The influence of Microstructural Features on Fatigue Crack Propagation in Ti-6Al-4V

M.J.J. Smedes

Master Thesis

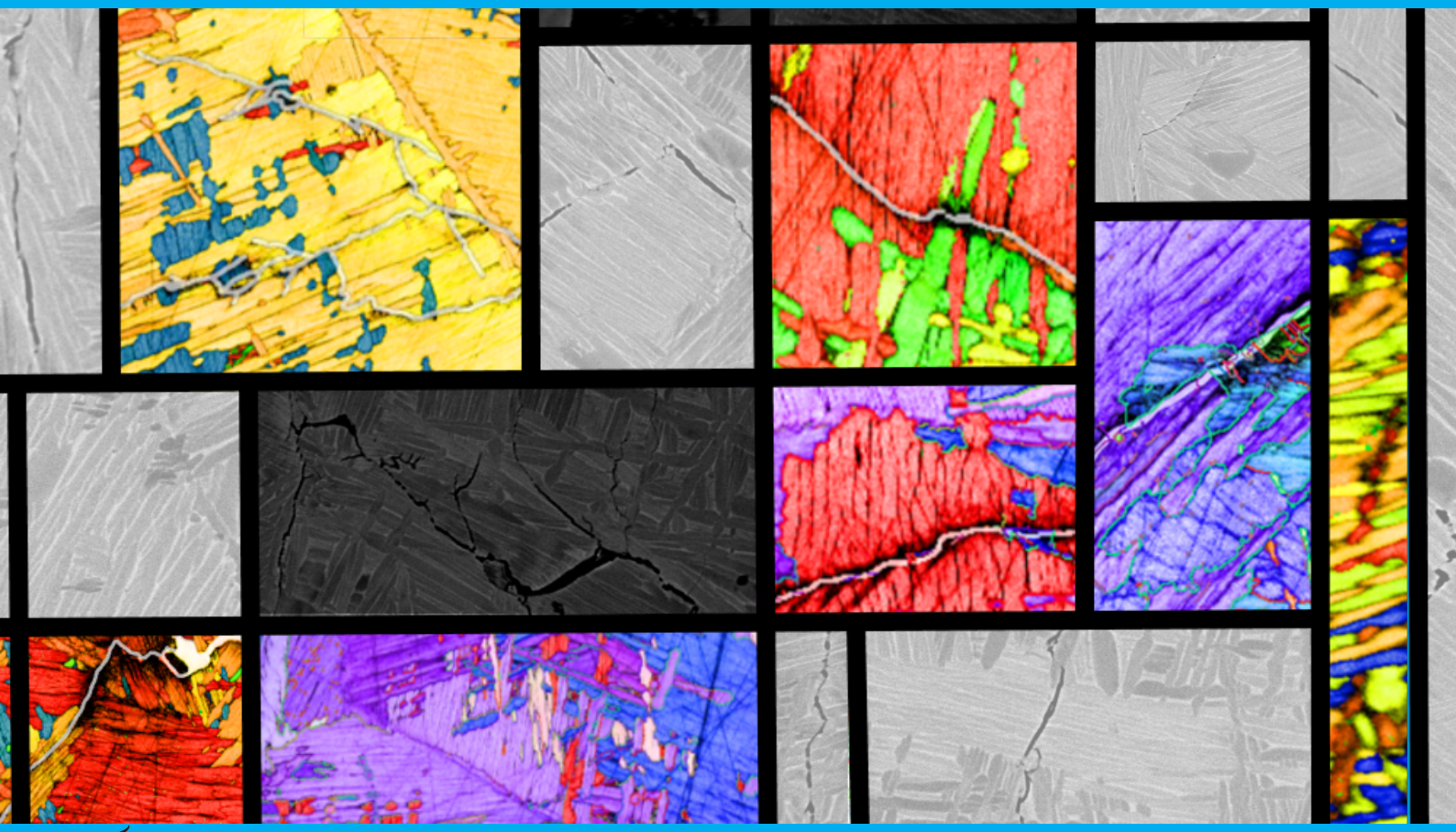

TU Delft

The influence of Microstructural Features on Fatigue Crack Propagation in Ti-6Al-4V

by

M.J.J. Smedes

to obtain the degree of Master of Science
at the Delft University of Technology,
to be defended publicly on Wednesday May 25, 2022 at 13:15 AM.

Student number:	4394739	
Project duration:	June 1, 2021 – May 25, 2022	
Thesis committee:	Prof. dr. ir. J. Sietsma,	TU Delft, supervisor
	Dr. ir. V. A. Popovich,	TU Delft, supervisor and committee chair
	Ir. J.N. Chamakura,	TU Delft, supervisor
	Prof. dr. ir. L. A. I. Kestens	TU Delft / U Gent

An electronic version of this thesis is available at http://repository.tudelft.nl/.
Cover image inspired by the work of Piet Mondriaan.

TU Delft

Preface

I would like to thank Jilt Sietsma, Vera Popovich and Jaji Chamakura for their supervision during my masters thesis project. Their input, feedback and expertise were invaluable for a successful completion of my thesis.

I would like to thank Ton Riemslag for his help during the testing phase, Hans Hofman for the help during heat treatment and Ruud Hendrikx for the XRD measurements. I would like to thank Kees Kwakernaak in particular for his help during the EBSD analysis, for which he has gone above and beyond for me.

The discussions with my peers and support of my friends and family have helped me throughout the process. Finally, I would like to dedicate this thesis to my father, Jaap Smedes, who I have lost in the last months during my thesis. He has been an amazing inspiration throughout my life and he is the reason I am where I am today.

M.J.J. Smedes
Delft, May 2022

Abstract

In our modern world, where computers, mobile phones and many other applications have become indispensable, there is a growing need for high precision machines in order to be able to produce these technologies. For these complex high precision applications it is important to understand the fatigue properties of the materials used to prevent premature failure, as these materials are subjected to large numbers of stress cycles. A material that is used for high precision applications is Ti-6Al-4V, as its material properties are highly adaptable and can be fine-tuned for a wide range of applications.

Material fatigue due to stress cycles knows two stages: crack initiation and crack propagation. This research focuses on the latter and looks into the influence of microstructural features on crack propagation in Ti-6Al-4V. The influence of the microstructural features is tested by applying a load shedding method to form cracks in Ti-6Al-4V samples. These cracks are analysed with Scanning Electron Microscopy (SEM) and Electron BackScatter Diffraction (EBSD) in order to relate the microstructural features to the crack path.

There are two main microstructural features found to have a large influence on the fatigue crack propagation in Ti-6Al-4V. The first of these is the Schmid factor, which relates the applied stress to the slip system available. As there are only a small amount of slip systems available in Ti-6Al-4V and limited crack path propagation opportunities, large crack deflections can be the result. The second microstructural feature found to have a large influence is the misorientation angle of the grain boundaries. When the misorientation angle is large enough, a shift from transgranular cracking to intergranular cracking is observed. Intergranular cracking can cause deviations of the crack path around the grains and the formation of secondary cracks.

The deviations in crack path as a result of a low Schmid factor and a high misorientation angle extend the fatigue life of the material. The Schmid factor was found to have a large influence on crack deflections observed, whereas the high misorientation angles were mostly found around sites where bifurcation occurred, especially at lower applied stress ranges.

This study proposes that the influence of the microstructural features on fatigue crack propagation in Ti-6Al-4V can be expressed as two probability functions describing crack deflection and bifurcation. The probability of a crack deflecting is relatively high for a lower Schmid factor, a high misorientation angle and a low deflection angle. The probability of bifurcation is relatively high when a near-threshold stress intensity range is applied and also for a high misorientation angle and a low deflection angle.

Contents

Nomenclature

$\Delta\sigma$	Stress range
ΔK	Stress intensity range
ΔK_{th}	Fatigue crack propagation threshold
$\Delta K_{th,eff}$	Intrinsic fatigue propagation threshold
$\Delta K_{th,LC}$	Fatigue crack propagation threshold for a long crack
$\Delta K_{th,op}$	Fatigue crack propagation threshold component induced by crack closure
$\frac{da}{dN}$	Fatigue crack growth per cycle
ϕ	Deflection angle
ψ	Misorientation angle
σ_e	Endurance limit
m_s	Schmid factor
a	Crack length
B	Sample thickness
C, m	Paris' constants
d_1	Crack length transition between a microstructurally short crack and a mechanically short crack
d_2	Crack length transition between a mechanically short crack and a long crack
K_{Ic}	Fracture toughness
R	Ratio of minimum over maximum applied stress
W	Sample width
CRSS	Critically resolved shear stress
EBSD	Electron backscatter diffraction
EDM	Electrical discharge machining
EDS	Energy-dispersive x-ray spectroscopy
EPFM	Elastic-plastic fracture mechanics
FEM	Finite element method
HAGB	High angle grain boundary ($> 15°$)
HCP	Hexagonal close-packed
IPF	Inverse pole figure
LAGB	Low angle grain boundary ($< 5°$)
LEFM	Linear elastic fracture mechanics
SEM	Scanning electron microscopy
XRD	X-ray diffraction

List of Figures

List of Tables

1

Introduction

In the first half of the 19th century, metals were first observed to fail at cyclic stresses below their yield stress. Back then, this phenomenon was explained by the metal becoming tired, or fatigued [1]. Nowadays this phenomenon is much better understood and the mechanics behind metal fatigue have been described in great detail. The fatigue life of a material can be categorized in two main stages: initiation and propagation. Where the initiation stage can be random at times, the propagation stage can be predicted and described by modern fracture mechanics [2].

When a high precision application like the advanced lithography machine by ASML is considered, the fatigue life must be well known to avoid premature failure due to unexpected crack propagation rates, especially when rapid movements at high g-forces are applied to a waver which need to be counteracted by use of a counterweight. This counterweight is supported by flexure mechanics which experience high stresses for an extended number of cycles. These forces are a result of an acceleration of the waver of up to 7 g for as many as 27500 times per hour [3]. It is therefore of crucial importance to understand the mechanics behind the fatigue failure of the material in order to predict and prevent this premature failure.

The material selected to research for this application in the current study is Ti-6Al-4V , which is commonly used for aerospace and high precision applications [4]. The material properties of Ti-6Al-4V are well described in literature and the microstructures are well understood. After proper heat treatment, the fatigue strength of Ti-6Al-4V is higher than that of AISI 420 steel alloy, currently used in high precision applications [5]. In the current research, the mechanics researched behind the fatigue strength of Ti-6Al-4V will be limited to the crack propagation stage. The crack propagation stage is mostly influenced by microstructural features where the crack initiation is mostly influenced by the surface finish [6]. Despite the mechanical properties of Ti-6Al-4V being well understood, the specific influence of the microstructural features in Ti-6Al-4V on the fatigue crack propagation is not as well described. For steel and aluminium alloys the influence of certain microstructural features are already closely related to the fatigue crack path [7, 8]. This shows that there is a clear need to describe the influence of these microstructural features on fatigue crack propagation. The goal of the current research is therefore to identify the influence of the microstructural features on the crack path. Given that these microstructural features can then be identified or controlled within a sample, more accurate predictions on fatigue life can be made.

Chapter 2 provides background knowledge, where some fundamentals of metal fatigue and the material Ti-6Al-4V are described. The microstructural features most important for fatigue crack propagation are also introduced. The methods used to test the Ti-6Al-4V for the fatigue properties and the characterization methods used to find the microstructural features present are described in chapter 3. Finally, the obtained results are discussed in chapter 4, where the microstructural features are linked to the crack path. Two probability relations are proposed for the crack path deviations as functions of the microstructural features present and the load cases applied. These probability relations can be used to describe the influence of the microstructural features on the fatigue crack propagation in Ti-6Al-4V .

1.1. Problem statement

From the initial problem provided by ASML, where unexpected fatigue failure rates have been observed, a research question and subsequently, sub-questions have resulted. A correlation was found between the microstructural features in Ti-6Al-4V and fatigue crack propagation in literature. This correlation has led to the hypothesis that by mapping the influence of the microstructural features in Ti-6Al-4V on fatigue crack propagation, a better prediction of the fatigue life of the material can be made. By answering the following question this better prediction can be achieved and as a result more reliable materials can be designed:

What is the influence of the microstructural features in Ti-6Al-4V on the fatigue crack propagation?

This research question is separated into sub-questions in order to obtain a systematic approach to answering the research question. The first sub-question relates the current state of the art to the current research. During a literature study the following question is answered:

Which microstructural features influence the fatigue crack propagation properties in Ti-6Al-4V?

Once the specific microstructural features which influence the fatigue crack propagation are known, the fatigue cracks need to be formed within samples. The method by which these cracks are made and analyzed needs to be designed, which leads to the following sub-question:

Which experimental methods can be used to determine the influence of the microstructural features on the fatigue crack propagation in Ti-6Al-4V?

When the fatigue cracks are eventually formed and characterized, the microstructural features found can be related to the crack path observed. This relation is made using the final sub-question:

How do the microstructural features affect the probable crack path during fatigue crack propagation in Ti-6Al-4V?

2

Background

Several mechanics are at play when considering fatigue crack propagation in Ti-6Al-4V. In order to explore these mechanics, some background knowledge of the material and fatigue in general is required. This includes a detailed description of Ti-6Al-4V and its alloying elements and microstructures in section 2.1. The mechanics behind fatigue and the parameters influencing it are described in sections 2.2 to 2.4. The features which might affect fatigue crack growth and their relevance to the current research are discussed in section 2.5.

2.1. Material description Ti-6Al-4V

For high precision and medical applications titanium and its alloys are often considered when an excellent combination of mechanical and physical properties are required. This is due to the ability to finely tune the mechanical properties of titanium alloys to certain specifications by means of heat treatment. These mechanical properties are combined with desirable physical properties such as a low density of 4.42 g/cm^3. The alloying elements in titanium alloys play an important microstructural role as they will influence the phases present and their morphology. These features will also have an influence on the fatigue life properties of the titanium alloy.

2.1.1. Alloying elements

Titanium can be alloyed with many different elements which can provide a range of benefits to the properties of the material. However, almost 50% of the titanium alloys are created by alloying titanium with aluminium and vanadium [4]. The most commonly used alloy containing these elements is Ti-6Al-4V, accounting for about 45% of the total sold titanium alloys, with the usual chemical composition shown in table 2.1.

Table 2.1: Nominal composition of grade 5 Ti-6Al-4V in wt% and impurity limits in wt% (max) [4].

Ti	Al	V	N (max)	C (max)	H (max)	Fe (max)	O (max)
Balance	6	4	0.05	0.10	0.0125	0.30	0.20

The aluminium in Ti-6Al-4V is present as an α stabilizer, which results in a higher melting temperature. The higher melting temperature allows for the material to be heated to higher temperatures during the heat treatment. When higher temperatures are reached, a higher percentage of α platelets can be obtained. These α platelets in turn lead to an increased hardness and strength when compared to a β structure [9]. At 6-7 wt% aluminium, the alloy has the highest thermostability and optimum welding properties, excellent for potential additive manufacturing applications. Moreover, adding aluminium has the effect of increasing the β transus temperature and enhancing the solubility of β stabilizing elements.

The β stabilizing element in the case of Ti-6Al-4V is vanadium. Vanadium is considered an isomorphous stabilizer since the crystal lattice of vanadium is BCC. Like the crystal lattice of β titanium, this allows for great solubility of vanadium in β titanium. When 4 wt% of vanadium is added to the alloy, the microstructure which is found changes from fully α in Ti-6Al to $\alpha + \beta$ in Ti-6Al-4V [10]. Moreover,

the creep resistance is decreased and the structure stability is increased [9]. The combination of the α and β stabilizers allows for a bimodal structure which can greatly improve the fatigue properties of the material when compared to commercially pure titanium. This bimodal structure is even considered to be the best morphology for fatigue life properties by Lu et al.[9], due to the resistance to crack initiation.

Finally, the impurities in Ti-6Al-4V can have an influence on certain material properties. The nitrogen, carbon and oxygen should be carefully controlled to improve ductility for cryogenic applications. Iron impurities are added to some alloys of titanium to improve the corrosion behaviour of the material [4].

2.1.2. Microstuctures

The microstructure of the Ti-6Al-4V alloy is generally a combination of the hard and brittle α phase and the more ductile and soft β phase. These phases can exist in several arrangements, from lamellar at one end of the spectrum to equiaxed at the other end [11]. The lamellar structure is shown in Figure 2.1a with a high surface area between the α lamellae and organized colonies, as opposed to the equiaxed structure as shown in Figure 2.1b, with a low surface area between the globular α grains. A combination of an equiaxed and lamellar structure, i.e. a bimodal structure, is shown in Figure 2.1c.

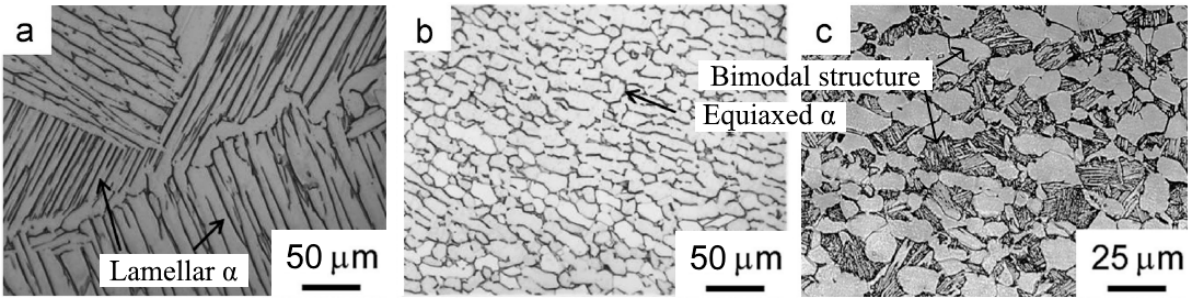

Figure 2.1: Micrographs of lamellar α, equiaxed α and bimodal $\alpha + \beta$ phases in Ti-6Al-4V alloy adapted from [12, 13].

The different phases and structures present in Ti-6Al-4V will have different effects on the crack propagation mechanisms in the material [11, 14]. The fatigue crack propagation resistance of a lamellar α phase is compared to an equiaxed α structure in order to study the effect of the phase and structure of the material. It was found that the resistance to crack propagation is superior in the lamellar α phase structure which is caused by a difference in crack propagation mechanics in both structures. This difference can be mostly attributed to bifurcation of the cracks due to the α colonies, shown as the groups of parallel lamellae in Figure 2.1a, present in the lamellar α structure. These α colonies are known to cause bifurcation, large crack deflection and secondary crack formation. This is caused by the limited slip systems available in the HCP α structure [15]. The crack growth resistance of the lamellar α phase is mostly attributed to the large crack deflection and bifurcation due to the limited crack paths available and the large size of the α colonies.

Meanwhile, the equiaxed structure shown in Figure 2.1b allows for a straight crack propagation path. A crack deflection is generally only as large as the diameter of the equiaxed α phase. The crack is able to propagate along the slip bands of the equiaxed α particles and the α/β interface. This results in an easy connection being made between the microcracks formed at the α/β interface [16].

Finally, a combination of the lamellar and equiaxed microstructures is shown in the bimodal structure in Figure 2.1c. This structure is similar to the lamellar microstructure in several fatigue life aspects. When the fatigue life properties and the resistance to fatigue crack growth were compared, the lamellar structure slightly outperformed the bimodal structure due to the larger overall grain size. When the stress ratio tended toward extremely high values this effect was eliminated but the bimodal structure would not outperform the lamellar structure [13]. Lu et al. [9] considered the bimodal structure to be the most fatigue resistant morphology but this includes the crack initiation stage. When only fatigue crack propagation is considered, the lamellar structure has a superior resistance.

2.2. General introduction to fatigue crack growth

Fatigue in its simplest form is defined as the failure of a specimen after a specified number of stress cycles [17]. The fatigue failure of a material can be separated into two processes: the crack initiation

and the crack propagation. However, all fatigue properties can be summarized with one main parameter, the fatigue strength, which depicts the stress amplitude under which the material will not fail for an infinite number of cycles. The fatigue strength is usually given as the endurance limit (σ_e), which is the stress amplitude under which a material will not fail for a very large number of cycles, e.g., 10^7 [18]. The fatigue behaviour of a material is most commonly plotted as the stress amplitude versus the number of cycles, also referred to as the Wöhler curve (S-N curve). Two examples of S-N curves are shown in Figure 2.2. The endurance limit is generally much lower than the yield strength of a material. For example, when equiaxed Ti-6Al-4V is considered, it has an endurance limit of approximately 500 MPa, shown in Figure 2.2a, whereas the yield strength is around 900 MPa [19]. Therefore, a cyclic load is able to cause failure in a material at lower stresses than a monotonic load is able to.

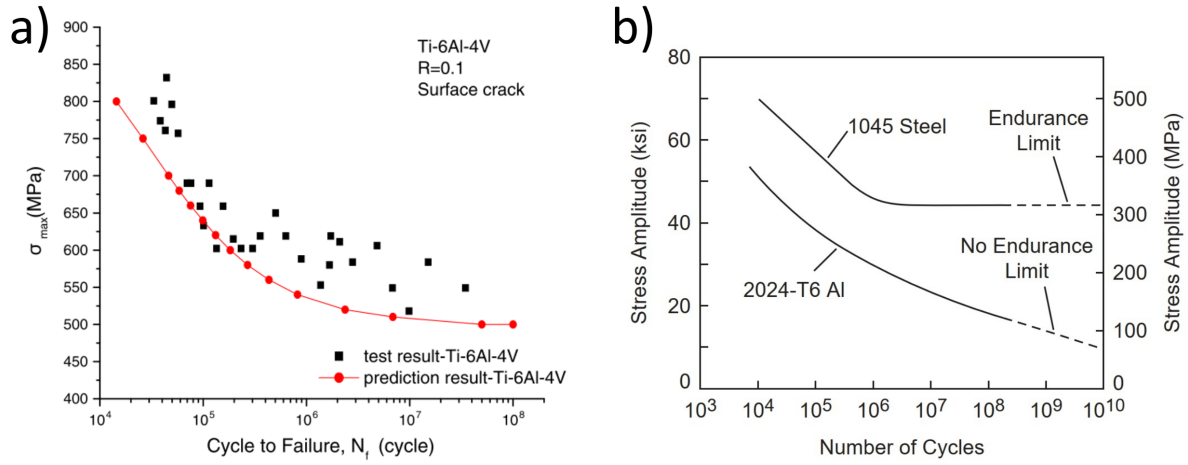

Figure 2.2: Fatigue behaviour of Ti-6Al-4V showing an endurance limit at 500 MPa (a) and a comparison of steel and aluminium S-N curves (b) [20, 21].

Not all materials have an endurance limit. Figure 2.2b for example, shows no endurance limit for aluminium. A small stress concentration like a crack tip can also increase the stress amplitude above the endurance limit. In order to design a safe-life construction for these cases, a deep understanding of the mechanics at work during fatigue failure is necessary.

The crack initiation and propagation stages are dependent on many factors and parameters. The crack initiation will briefly be addressed in section 2.2.1 as it can account for a large part of the fatigue life of a material. The main focus of the current research will be on the crack propagation which will be discussed thereafter.

2.2.1. Crack initiation

The first step in fatigue failure is the crack initiation process. This initial step can take up a significant part of the fatigue life-time [6].

Tu and Zhang [6] divided the sites at which crack initiation takes place into three main locations depending on the grain size, the surface treatment or the morphology:

- Persistent slip bands
- Grain boundaries
- Inclusions

A persistent slip band is a regular arrangement of dislocations over a long distance. The clustering of the dislocations is the result of their interaction and movement through the lattice. This movement is a result of the applied stress where the interactions of the dislocations cause them to cluster. When the stress is above a certain threshold, the cluster becomes a stable pattern, a persistent slip band, which spreads through the whole grain [22].

The stress concentrations at the grain boundaries due to the grain boundary-slip band interaction are commonly believed to be the main reason for crack initiation. Inclusions can become sites for

crack initiation when a large inclusion creates a high plastic strain region which promotes an early crack initiation.

The crack initiation process can be slowed down by implementing several surface treatment techniques like deep rolling and shot peening. The effect of deep rolling is to work harden the surface of the material which leads to an increase in the number of cycles required for crack initiation. Firstly, the work hardening will increase the hardness and yield strength due to the high dislocation density at the surface. Secondly, after the work hardening, the introduced dislocations will reorganize during a recovery process at an elevated temperature and form sub-grains, decreasing the overall grain size of the material. The high residual stress and the improved smoothness at the surface prevent the initiation at the surface and cause the initiation to happen at defects or inclusions within the material. When a surface is shot-peened, the treatment creates high residual compressive stresses in the surface which in turn increases the micro hardness. This increase in surface hardness moves the crack initiation site under the surface of the material and therefore extends the number of cycles required for crack initiation. This outcome is observed in several materials, including titanium alloys [6].

2.2.2. Crack propagation

The second stage in fatigue failure is crack propagation, which will be the main focus of the current research. During the crack propagation stage the initial crack will propagate using different mechanisms as the crack grows until failure of the specimen. A classification has been made between the different sizes of cracks as different mechanisms are at work:

- Microstructurally short cracks, described by microstructural fracture mechanics
- Mechanically Short cracks, described by elastic-plastic fracture mechanics (EPFM)
- Long cracks, described by linear elastic fracture mechanics (LEFM)

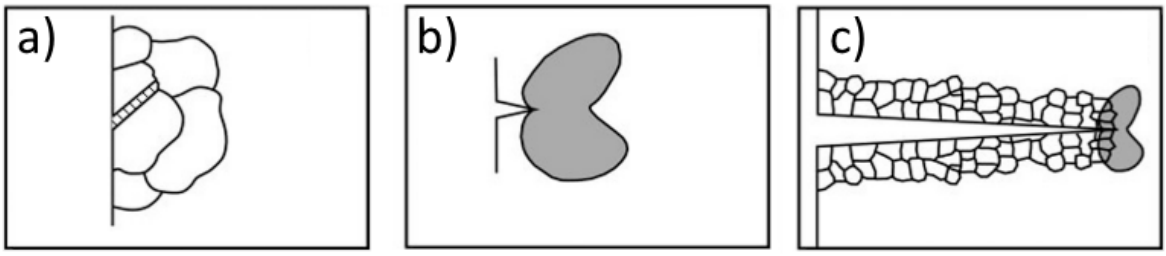

Figure 2.3: Different crack classifications visualized with the grey zone as the plastically affected zone, microstructurally short (a) typically under 50 µm, mechanically short (b) typically under 500 µm and long crack (c) typically over 500 µm adapted from [2].

The sizes of the three classifications of cracks seen in Figure 2.3 are separated by two designated parameters, d_1 and d_2. The parameter d_1 is the crack length for which the microstructurally short crack transitions into the mechanically short crack, d_2 is the length at which a crack transitions from a short crack to a long crack.

The microstructurally short crack is the initial crack from which further crack propagation is described. This crack is the minimum size for the initial crack size a_i which is further defined as follows.

- The largest initial material defect such as an inclusion, secondary phase, pore and other defects.
- Surface defects such as pits or scratches.
- The largest just arrested microstructurally short crack.
- The largest otherwise detectable defect.

The initial crack size will be the largest of the groups described above. This crack size a_i has to be the same size or larger than d_1 since otherwise the crack will be arrested at an early stage at stresses below the endurance limit. The parameter d_1 can then be described as the largest of cracks which are still arrested when a stress below the endurance limit (σ_e) is applied.

Once a crack has reached a length d_1, elastic-plastic fracture mechanics come into play. This introduces the fatigue crack propagation threshold ΔK_{th} which is composed of effective threshold $\Delta K_{th,eff}$ and the crack tip opening threshold $\Delta K_{th,op}$ where $\Delta K_{th,eff}$ is a material property below which no crack propagation occurs and $\Delta K_{th,op}$ is a crack length dependent parameter which reaches a maximum when a short crack transforms into a long crack. The parameter $\Delta K_{th,op}$ is dependent on different empirically fitted parameters such as the crack closure effect, the yield stress and the crack extension of the material [2].

Figure 2.4 shows the complicated elastic-plastic fracture mechanics of the mechanically short crack regime. In Figure 2.4, the correlation between the fatigue crack propagation threshold and the crack length is plotted. When a stress is applied above the solid line, the crack will propagate. When the stress results in a stress concentration below the solid line, indicated as the cyclic R-Curve, the crack will arrest.

When a mechanically short crack, for example, experiences a stress $\sigma_{a,1}$ the crack will propagate, causing the stress intensity to increase with it. However, due to the effect of crack tip opening, the required stress intensity for crack propagation ($\Delta K_{th,op}$) also increases. When the stress $\sigma_{a,1}$ is applied, the required stress intensity for propagation has increased faster than the applied stress intensity has and therefore crack arrest is observed. If the stress on the specimen exceeds $\sigma_{a,2}$, such as is the case for $\sigma_{a,3}$ in Figure 2.4, the stress intensity will increase faster due to the crack growth than $\Delta K_{th,op}$ due to the crack tip opening and thus the crack will propagate past the length d_2 and transition into a long crack.

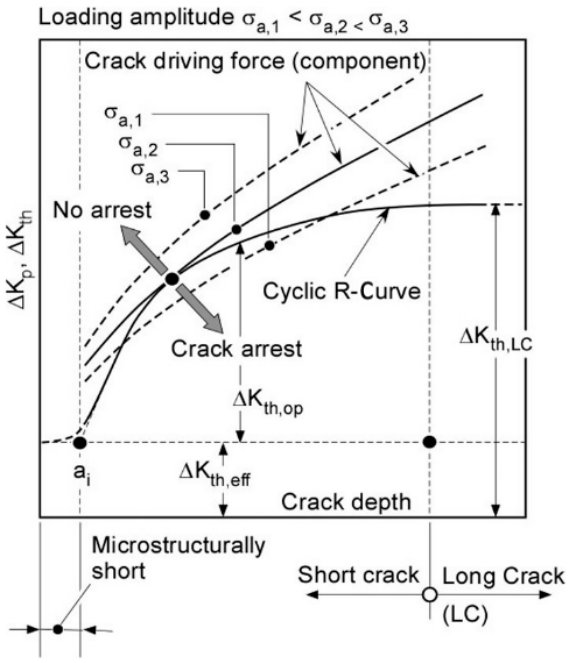

Figure 2.4: Cyclic R-curve displaying the different stresses for which crack arrest either does or does not occur [2].

Once the crack length has reached the long crack size, the crack propagation can be divided into three regions according to Paris' law, as seen in Figure 2.5. This starts with the short crack transition into the long crack in region 1. Region 2 is the crack propagation phase where Paris' law is supposed to hold and region 3 is the phase of fast propagation which leads to failure [23].

Figure 2.5 shows the behaviour of the long cracks where linear elastic fracture mechanics (LEFM) apply. LEFM is a theory which assumes linearity in the lifetime estimation, which is indicated in stage 2 of Figure 2.5. This linearity allows for simple analyses of fracture mechanics using theoretical, numerical and experimental data. Some short cracks for which elastic-plastic fracture mechanics (EPFM) apply, are plotted as dashed-lines. EPFM is used to analyze more plastic affected zones and requires more resources than the LEFM and will therefore be mostly defined using empirical data [24]. The behaviour of the crack propagation in stage 2 is given by Paris' law [25]. This law describes the relation

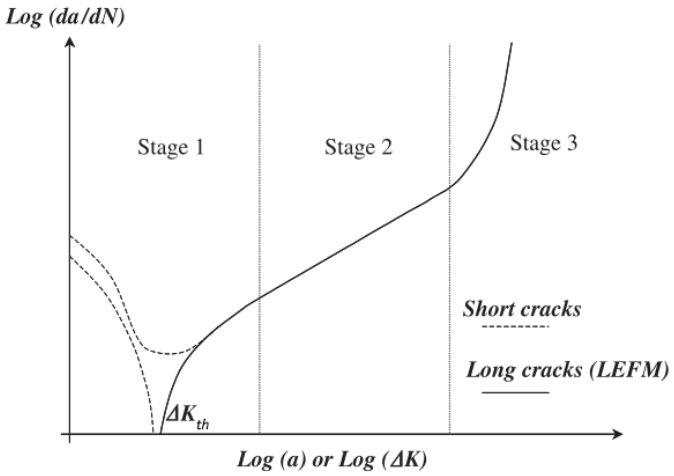

Figure 2.5: A visualization of the different Paris regions where Paris' law holds for stage 2 [23].

between the crack propagation rate and the stress intensity range ΔK where LEFM applies:

$$\frac{da}{dN} = C\Delta K^m, \qquad \Delta K_{th,LC} < \Delta K < K_{Ic} \tag{2.1}$$

Where Paris' constants C and m describe the crack propagation rate per load cycle $\frac{da}{dN}$. The fatigue parameter applied is ΔK which is the stress intensity range. The lower limit of the stress intensity range is the fatigue crack propagation in the long crack regime, $K_{th,LC}$, and the upper limit is the fracture toughness, K_{Ic}. Once ΔK reaches the fracture toughness, the crack propagation rate will increase dramatically and failure will rapidly occur. This law, however, has been proven to be more of an assumption rather than a universal law. This is because Paris et al. suggested, without experimental verification, that the observed effect of applied stress ratio on the crack propagation rates is a direct result of crack closure which is a phenomenon to be addressed later, in section 2.4 [25]. Later it was found that it overestimated the effects of crack closure as it is only significant in plane stress situations and that is further reduced by environmental factors and stress intensities [26].

2.3. Fatigue Testing Parameters

When researching fatigue and crack propagation in particular, experimental set-ups are still the preferred method in describing the materials response to the load cycles applied. Several testing parameters can be altered which have an influence on the mechanisms at work during crack propagation.

2.3.1. Stress Intensity Range

The most important testing parameter in crack propagation is the stress intensity range ΔK, which is described by the range of stresses applied to the crack as a function of the crack length and geometrical factors. The stress intensity range is commonly described by [2]:

$$\Delta K = Y(a)\sqrt{\pi a}\Delta\sigma \tag{2.2}$$

Here $Y(a)$ is a geometrical factor as a function of crack length a and $\Delta\sigma$ is the applied stress range. From this equation it becomes clear that ΔK changes for a change in crack length even at a constant applied stress range.

2.3.2. Frequency

The frequency of the load cycles is a parameter which has the ability to alter the resulting fatigue propagation parameters but is not included in most calculations. This is most likely due to the effects of frequency being mostly dependent on environmental conditions when normal testing frequency ranges are considered (1Hz-100Hz) [2]. When testing at a frequency range of 20Hz-20kHz, a discrepancy

was found between when testing in a gaseous environment consisting of air and in a vacuum. When similar tests were executed either in air or in a vacuum, only the environment containing air responded to varying frequencies whereas the crack propagation in the vacuum did not change. This difference is attributed to the effects of hydrogen embrittlement [27].

2.3.3. R-ratio

Another important parameter is the R-ratio or load ratio. The R-ratio represents the ratio between the minimum and the maximum stress ($\sigma_{min}/\sigma_{max}$) applied to the specimen. This ratio has an influence on the fatigue growth rate due to its effects on the crack closure concept [28, 29]. This effect is simply explained by the notice that at an R-ratio close to one will keep a crack open as σ_{min} and σ_{max} both pull the surfaces of the crack apart. When σ_{min} is decreased, the crack will close due to a lack of stress applied or the crack can even be pushed into itself. The compressive stresses then cause closure at the crack tip.

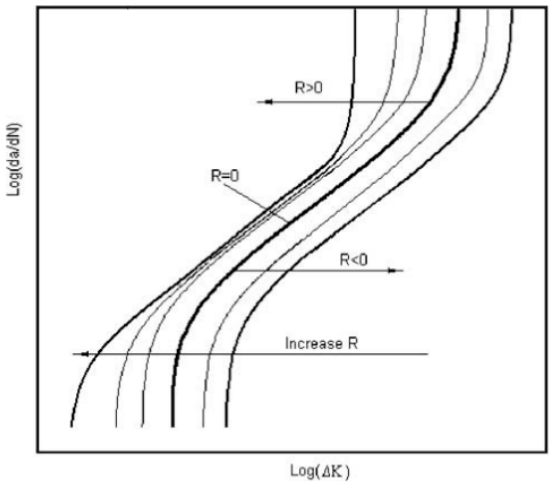

Figure 2.6: A visualization of the influence of the R-ratio on the fatigue crack growth by shifting Paris' diagram [30].

Figure 2.6 shows that there is a clear correlation between the R-ratio and the crack growth rate for a given ΔK. The crack growth rate increases for a given ΔK when the R-ratio is increased. The importance of the crack closure effect due to the R-ratio however, seems to have been overestimated in the past. For a negative R-ratio, only the positive part of the applied stress intensity factor (ΔK^+) range contributes to the crack growth [30]. Therefore Equation 2.1 (Paris' equation) should become:

$$\frac{da}{dN} = C(\Delta K^*)^m \tag{2.3}$$

With,

$$\Delta K^* = (K_{max})^{\alpha}(\Delta K^+)^{1-\alpha} \tag{2.4}$$

Where α is an empirically fitted constant and K_{max} is the maximum stress intensity applied. This new model was created to correlate fatigue crack growth data for a range of $-1 \leq R < 1$. However the correlation between experimental data and this model is still better for positive R-ratios of $0 \leq R < 1$, than for negative R-ratios of $-1 \leq R < 0$. This is likely due to the negative part of ΔK not influencing the crack closure for a negative R-ratio. Even for higher R-ratios of $R > 0.7$, eqs. (2.3) and (2.4) are not sufficient to predict growth rate data of Ti-6Al-4V.

2.4. Crack closure mechanisms

Crack closure occurs when the opposing surfaces of a crack come into contact with each other before the minimum load of the load cycle is reached. This can be achieved using several mechanisms, all indicated as crack closure. These include plasticity, roughness and oxide-induced effects. The plasticity-induced crack closure is a result of the stress state in the sample. Roughness-induced crack

closure is heavily dependent on the grain size in the material [31], where the oxide-induced crack closure is an environmental effect, dependent on the oxidation rate of the material [2]. A schematic depiction of the three crack closure mechanisms is shown in Figure 2.7.

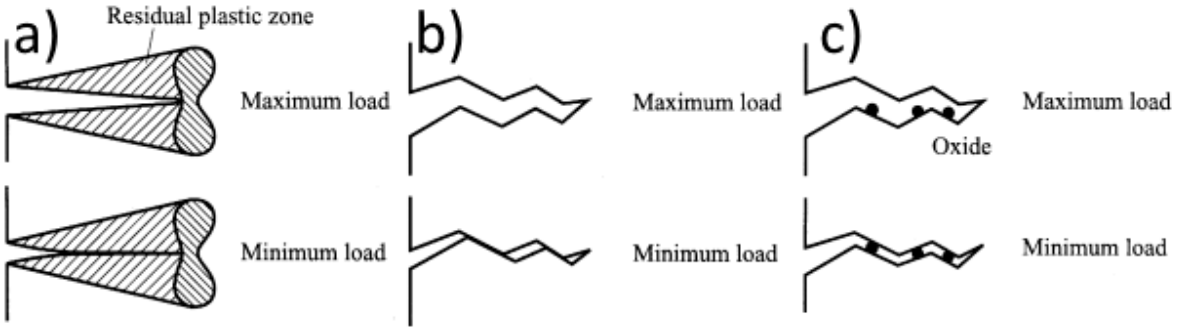

Figure 2.7: Three different crack closure mechanisms including the plasticity-induced (a), the roughness-induced (b) and the oxide-induced (c) effects [32].

The plasticity-induced crack closure is a result of the plastic deformation along the crack which is particularly high at the crack tip. When the crack tip then advances, plastic deformation normal to the crack length is left behind along the rest of the crack. This deformation is not fully reversed in the minimum load condition, which can be seen in Figure 2.7a, leading to the material compressing into itself, resulting in a compressive residual stresses [33].

The idea of roughness-induced crack closure is that a higher grain size will increase the deflection length of the crack which will in turn increase the surface roughness of a crack surface. This roughness will then promote crack closure due to a misfit of the opposing crack surfaces. This idea has since been experimented upon by Gray et al. [31] using AISI 1080 steel, from which they concluded there is a significant increase of ΔK_{th} due to an increase of the grain size. This effect is most apparent at a lower R-ratio such as 0.1, seen in Figure 2.8. An increase of the R-ratio will allow the crack to remain open throughout the load cycle and thus reduces the effect of roughness-induced crack closure.

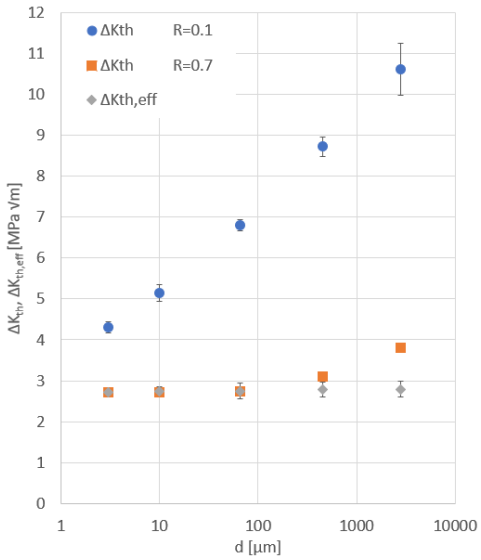

Figure 2.8: Effect of grain size on the different thresholds ΔK_{th} and $\Delta K_{th,eff}$ for different R-ratios in ARMCO iron, adapted from [34].

Oxide-induced crack closure is mostly influenced by environmental factors. When a crack propagates through a material, new surfaces are generated, oxidation layers can form on these surfaces when a gaseous atmosphere consisting of air is present. Due to these oxides generally having a larger volume than their metallic base material, the formation of oxides on the crack surface results in additional volume of material. Much like the plasticity and the roughness, this mechanism could cause the

crack to close slightly. Normally this layer will only be a few nanometres thick after such a short period of time and therefore will not induce a crack closure effect. This layer thickness however, can be greatly increased due to the build-up of these oxide layers caused by the continuous breaking and reforming during the load cycles. This effect is most pronounced at low R-ratios, at near-threshold loads and for low frequencies so there is more time for oxidation layer build-up [35].

The effect of the crack closure however, has been disputed over the years. One argument given against crack closure is that during tests comparing an open, partially closed and fully closed crack, the effects of crack closure were small and could not account for the observed behaviour in fatigue [36]. When taking a re-examination of the effect of crack closure on fatigue crack propagation, Jiang et al. [37] concluded that there is in fact an effect of crack closure but the crack closure effects may have been overestimated in traditional approaches.

An example of the influence of crack closure mechanisms at R-ratios of 0.02 and 0.25 is given in Figure 2.9. The fatigue crack propagation rate is directly plotted over the stress intensity factor. When the stress intensity induced by crack closure, $\Delta K_{th,op}$, is subtracted from the applied stress intensity range ΔK, only the effective stress intensity range $\Delta K_{th,eff}$ is left. The fatigue crack propagation rates overlap when only $\Delta K_{th,eff}$ is considered for different R-ratios as seen in Figure 2.9c. The difference in crack propagation rates is thus caused by the stress intensity induced by crack closure. A small portion of the crack closure effect is attributed to plasticity-induced mechanisms, but after a fractographic analysis, most of the crack closure at these low R-ratios is due to roughness-induced crack closure [38].

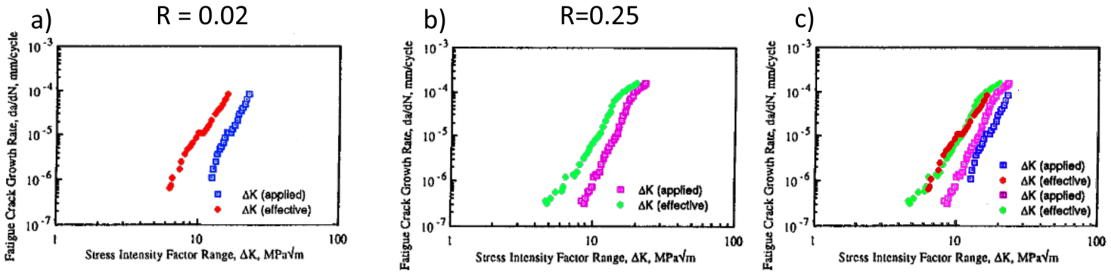

Figure 2.9: Relation between stress intensity and the crack propagation rate with and without crack closure mechanisms for an R-ratio of 0.02 (a), 0.25 (b) and an overlay of these figures in (c) in Ti-6Al-4V, adapted from [38].

2.5. Microstructural features

As has been described in subsection 2.1.2, a lamellar α phase has superior crack growth resistance when compared to other microstructures in Ti-6Al-4V. Some microstructural features of the lamellar α phase and their influence on the fatigue crack growth are therefore discussed in this section. The effect of the morphology and grain boundaries on the crack path is explained in subsection 2.5.1. The Schmid factor is introduced in subsection 2.5.2, a factor which relates the slip system to the load direction. The Schmid factor is highly dependent on the available slip systems while there are a limited number of slip systems in HCP. The Schmid factor could therefore prove to be an important property in fatigue crack growth.

2.5.1. Grain morphology

The influence of grain morphology can be further divided into the grain size and shape and the grain boundaries. On one side, the effect of grain size is the roughness-induced crack closure. As has been discussed in section 2.4, a larger grain size creates a rough crack surface which might induce a form of crack closure known as roughness-induced crack closure. On the other side, a large grain size leads to long grain boundaries which might be able to facilitate crack propagation more easily.

The grain boundaries are divided into three types of boundaries present in a lamellar α, shown in Figure 2.10.

- Prior β grain boundaries
- α colony boundaries

- α platelets boundaries

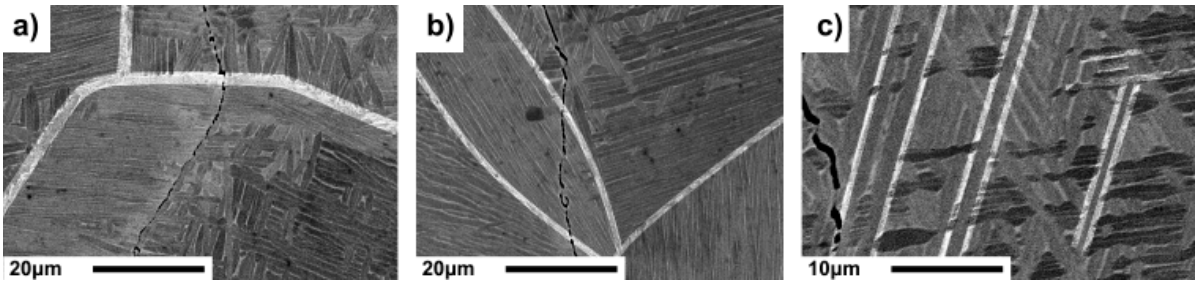

Figure 2.10: Three different types of boundaries found in β annealed Ti-6Al-4V , prior β grain (a), α colony (b) and α platelet (c).

In fine microstructures, the crack tip is deflected by grain boundaries such as the ones listed above. The deflection is a result of the neighbouring grains having distinct crystallographic orientations and thus allows for an easier path along the boundary, which is called intergranular cracking [39]. A lamellar α microstructure in Ti-6Al-4V is able to facilitate crack growth through the grain however, this is called transgranular cracking. When both intergranular cracking and transgranular cracking are possible, the misorientation angle will be able to influence the fracture mode. When a high angle grain boundary is encountered, intergranular cracking is the most plausible fracture mode [40]. Figure 2.11 shows this combination of intergranular and transgranular cracking as the crack bifurcated through packets of α colonies. When the crack was orientated favourably with the grains however, intergranular cracking was observed along the β grain and α colony boundaries.

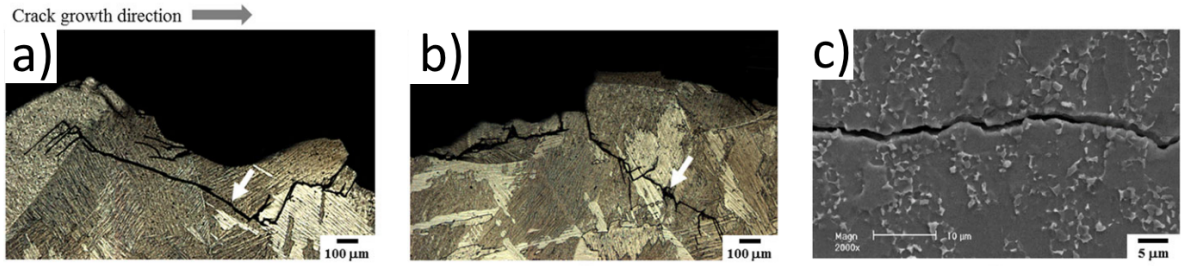

Figure 2.11: Micrographs showing crack deflection and bifurcation in β-annealed Ti-6Al4V using an optical microscope (a, b) and a straight crack path in mill-annealed Ti-6Al-4V examined by using an SEM (c) [14].

2.5.2. Schmid factor

When a crack propagates through the material, the grain boundaries present might not always facilitate an easy crack path. A transgranular crack growth can in some cases facilitate an easier crack path due to the slip systems being favourably orientated with the load direction. This relation between the slip systems and the load direction is described by the Schmid factor [41].

Ti-6Al-4V annealed above the β transus temperature and air-cooled is almost exclusively composed of α platelets which have an HCP structure [14]. The HCP structure only has a few viable slip systems available with both basal and prismatic being the main slip systems, seen in Figure 2.12.

The Schmid factor (m_s) is used to translate the applied stress (σ) to the resolved shear stress (τ) as shown in Equation 2.5. The Schmid factor is calculated as a function of the three unit vectors for the load direction (**l**), slip direction (**s**) and the slip plane normal (**n**), according to Zheng et al. [42].

$$\tau = m_s \sigma \tag{2.5}$$

$$m_s = (\mathbf{l} \cdot \mathbf{s})(\mathbf{l} \cdot \mathbf{n}) \tag{2.6}$$

Solving for the three different slip systems, Figure 2.13 shows the peaks of the Schmid factor of each slip plane, where a higher Schmid factor indicates less resistance to dislocation glide. A lower

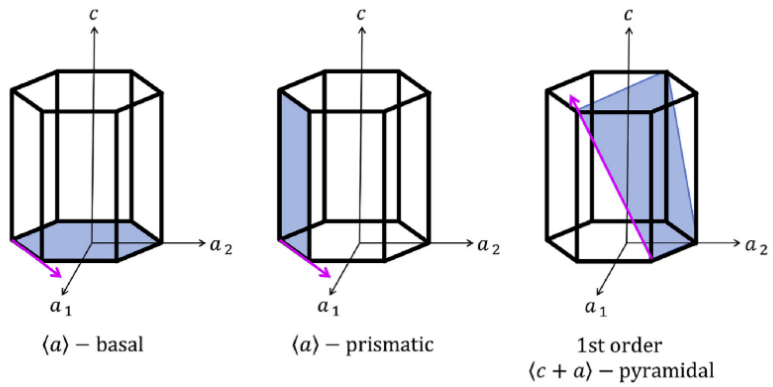

Figure 2.12: Three major slip systems in HCP [42]

resistance to dislocation glide leads to a lower resolved shear stress required for fatigue crack propagation.

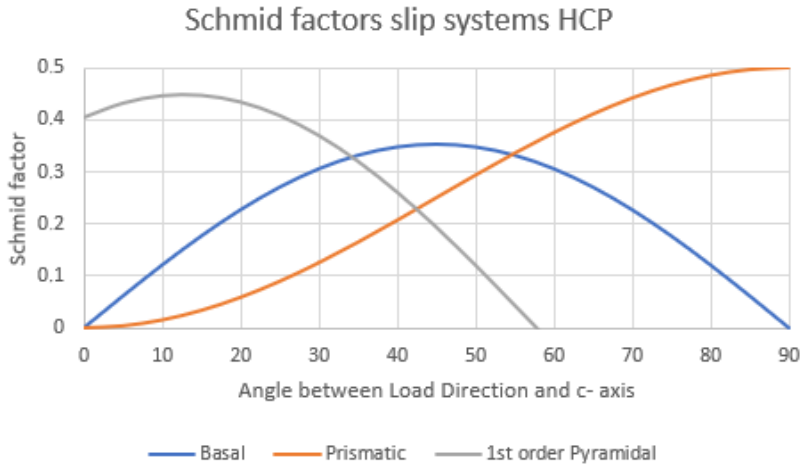

Figure 2.13: Results of Equation 2.6 applied on the three slip systems shown in Figure 2.12.

The graph shown in Figure 2.13 does not yet show the actual Schmid factors for the slip systems. This is due to the different slip systems having a different critically resolved shear stress (CRSS). This CRSS is the critical shear stress for which dislocation glide is possible. The Schmid factors will therefore be normalized, this is done by using [41]:

$$m'_s = m_s * (\tau_{min}/\tau_{system}) \tag{2.7}$$

Here m'_s is the normalized Schmid factor as a function of the Schmid factor m_s and the ratio of the CRSS of the easiest activated slip system τ_{min} and the the CRSS of a given slip system τ_{system}. For both the basal and prismatic plane this ratio is 1:1 as these are both the easiest slip planes. For the 1^{st} order pyramidal system is ratio is 1:2.63 which results in a significantly lowered normalized Schmid factor. This will result in Figure 2.14.

The plot shown in Figure 2.14 can now be used to describe the slip system used by the crack if the crystal orientation with respect to the load direction is known. By comparing the angle between the load direction and the c-axis to Figure 2.14, the slip system with the highest Schmid factor at that angle will be active during crack propagation.

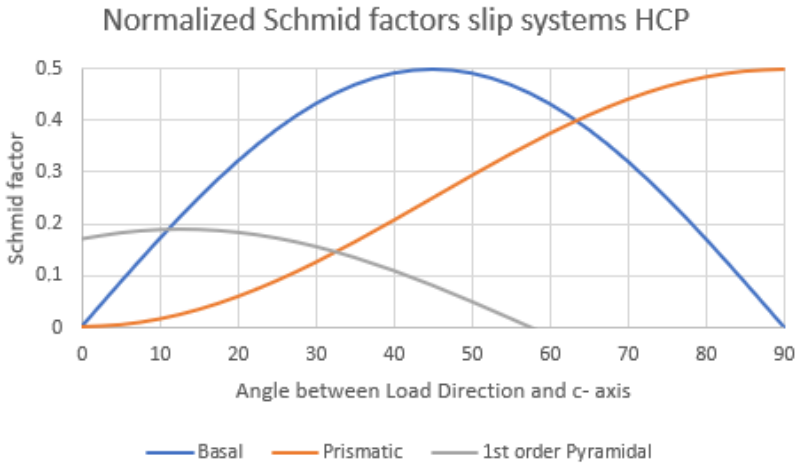

Figure 2.14: Schmid plot shown in Figure 2.13 normalized using a CRSS ratio for basal, prismatic and 1st order pyramidal of 1:1:2.63.

2.6. Concluding remarks

When high precision and medical applications are considered, excellent properties of the material and a good understanding of the failure mechanics are required. Ti-6Al-4V is a material with a great strength to weight ratio and corrosive properties. The unpredictability of fatigue crack growth can form an issue when high cycle lifetimes are required. The microstructure with the highest fatigue crack growth resistance is lamellar α and therefore the influence of certain microstructural features on fatigue crack growth in lamellar α Ti-6Al-4V will be explored.

The stress intensity range ΔK is a factor with a large influence on the fatigue crack growth rate. The crack growth will respond differently to different values for ΔK and by creating a Paris diagram, the stage of crack growth can be determined for each ΔK. By defining the stages of crack growth, the microstructural features affecting crack growth can be related to these stages.

The effect of the R-ratio on the fatigue crack growth rate has long been attributed to the crack closure effects. These effects are divided into plasticity, roughness and oxide-induced crack closure. The influence of crack closure has long been overestimated however as it could not account for the observed fatigue behaviour. By testing at a high and a low R-ratio, the effect of crack closure can be singled out and different effects of microstructural features can be highlighted.

The most influential microstructural features for fatigue crack growth in lamellar α Ti-6Al-4V are the high angle grain boundaries and the Schmid factors [39, 40, 41]. The high angle grain boundaries will deflect the crack path and induce intergranular fracture modes. The Schmid factor is able to relate the load direction to the crystallographic orientation. This Schmid factor reveals where transgranular crack growth is possible and in which slip system this might occur. By relating crack growth at the different stress intensity ranges and R-ratios tested, the influence of the microstructural features on the crack path can be described in more detail.

3

Methods and Experimental

In order to understand the impact of microstructural features in Ti-6Al-4V on the fatigue crack propagation, understanding of the microstructural features present and the fatigue properties of the material are essential. The process of understanding the microstructural features present in the material consists of a material treatment, preparation and characterisation process. The material treatment should result in homogeneous microstructural features and material properties throughout all experiments. Once this has been achieved, the experiments have to be designed using different design and modelling processes, such that all desired properties can be derived from the results for every load type tested. After these models result into an accurate depiction of the stresses present in the samples, actual experiments can be applied in order to determine the desired fatigue parameters. Once the specimens are tested, the microstructural features influencing the crack path can be analysed using a combination of different characterization techniques.

3.1. Material preparation

A proper analysis of fatigue crack growth in Ti-6Al-4V can only be achieved by acquiring a homogeneous material with the designed material properties. The samples will therefore all be treated using the same heat treatment, cooling period and clean-up process. A few aspects that can differ in the final material despite careful preparations are the oxidation layer and warping of the samples.

First of all, every sample is cut using electrical discharge machining (EDM) out of a single base plate of Ti-6Al-4V according to the design displayed in Appendix A. The material will then be heat treated for optimal fatigue crack growth properties according to [14]. By annealing at 70 °C above the β-transus temperature the microstructure will be homogenized by forming a fully β microstructure [43]. By heating to these temperatures however, the material will experience a significant increase in oxidation rate [44]. Since these oxidation layers cannot easily be controlled, they will be eliminated from the samples by treating in an inert environment. This is achieved by filling an annealing envelope with argon gas and subsequently adding the Ti-6Al-4V samples, after which the annealing envelopes are sealed and heat treated as a whole.

Another factor which might cause a variation in the samples is warping due to internal stresses from the EDM process being released during the heat treatment. This warping might cause the designed stress concentration in the sample being shifted due to bending forces. This will be counteracted by first bending the samples straight if needed. The internal stresses introduced in this process cannot be disregarded and will need to be taken into account during the analyzing process by using FEM models to calculate bending induced stress.

The first step in the design of the material is a heat treatment, this treatment will be applied to all samples and will be consistent over all experiments conducted. Once this treatment is applied, some samples will be prepared for microstructural characterisation.

3.1.1. Heat treatment

Nothing is known about the manufacturing method nor about the heat treatment of the base material provided by Titanium-Services [45]. The resulting microstructure of the manufacturing method and the

heat treatment applied on Ti-6Al-4V has the possibility to influence the results of a subsequent heat treatment [46]. The untreated material will therefore need to be characterised alongside the treated material in order to identify any microstructural features present due to the manufacturing method and prior heat treatment.

The design of the heat treatment which will be applied on the material used for fatigue testing is chosen from literature [14]. Due to the nature of the experiments, only one type of treatment will be tested. Therefore it is necessary to apply a known heat treatment which is used for a long fatigue life, especially for low fatigue crack propagation rates. One heat treatment which has been well described in literature is "β annealing". β annealing maximises the fracture toughness of a material at the cost of a significant decrease in fatigue initiation resistance [47]. However β annealed Ti-6Al-4V is described as having a good resistance to fatigue crack propagation by achieving a microstructure of lamellar α phase [48]. The current research is focused around fatigue crack propagation through Ti-6Al-4V and therefore β annealing will provide the desired properties. By following a specific heat treatment, a comparison can be drawn between the fatigue properties and microstructure of the material [14]. The heat treatment conditions used are described in figure Figure 3.1.

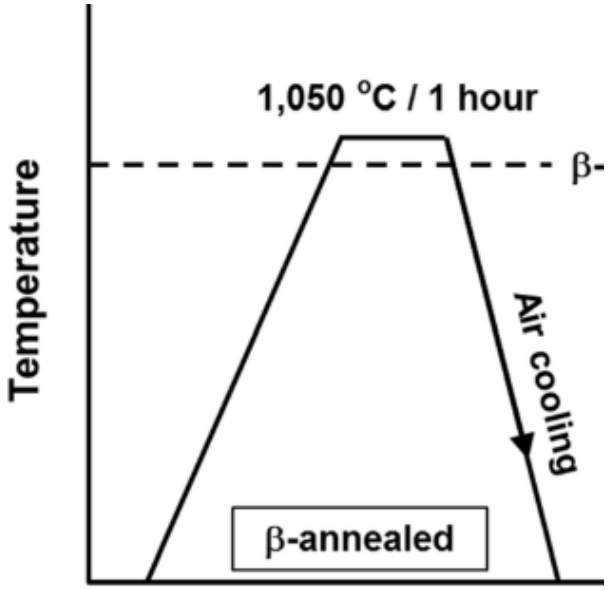

Figure 3.1: β annealing treatment applied to all Ti-6Al-4V samples with a thickness of 2 mm as designed by Jeong et al. [14].

The main goal of this heat treatment is to approach the lamellar α structure described by Jeong et al. [14]. This will allow for direct comparison of the fatigue properties measured by the different testing methods. This direct comparison can only be made when all samples are identical to each other. This is achieved by preventing oxidation by sealing the samples in annealing envelopes as described above. Before inserting the samples into these annealing envelopes however, they are thoroughly cleaned using 2-isopropanol. This is done to prevent any leftover residue on the samples from evaporating and settling down on the sample during the heat treatment. These annealing envelopes are then placed inside the heat treatment oven on top of a thermocouple in order to monitor the temperature of the sample during the treatment.

After the sample has been held at a temperature of 1050°C for 1 hour, the sample was removed from the oven and placed at room temperature to cool over the course of 2 hours outside the oven. During this cooling period the samples are held in the argon environment to prevent oxidation during the cooling process. The samples are removed from the annealing envelopes after they have cooled down to room temperature.

3.1.2. Microstructure preparation

Once the Ti-6Al-4V samples have been heat treated according to the method described in subsection 3.1.1 a series of preparation steps have to be applied before material characterisation can be

performed. This is done by hot-mounting a small segment of a Ti-6Al-4V sample in a conductive resin in a Struers CitoPress. By mounting the sample in a conductive resin the sample will still be compatible with SEM analysis during the characterisation process. After the sample is mounted, the sample is sanded and polished to remove any scratches which might be visible during optical microscopy. The sanding steps executed using SiC sandpaper on Struers LaboPol-25 are displayed in Table 3.1.

Table 3.1: Sanding steps for Ti-6Al-4V sample preparation.

Grit	Rotation speed [rpm]	Time [s]
P80	250	60
P180	250	60
P320	250	60
P800	250	60
P1200	250	60
P2000	250	120
P4000	250	300

The final step of sanding with P4000 grit sandpaper is added due to the inability to cleanly polish Ti-6Al-4V samples using 1 µm - 3 µm diamond polish. Diamond polishing introduces scratches and smearing on Ti-6Al-4V samples.

The subsequent polishing step is therefore solely made up of polishing using colloidal silica (OP-S) applied to a rotating MD-Chem cloth by Struers at a rotation speed of 300 rpm. The samples prepared for optical microscopy are polished for 15 minutes after which no scratches are observed using a 50x magnification optical microscope. Samples prepared for SEM/EBSD however, are polished for 2 hours using the OP-S and rotating MD-Chem cloth. During the polishing process it was found necessary to continuously wet the cloth with the OP-S solution and regularly flush the sample with 2-isopropanol. When this is not done, the OP-S starts to etch the material making EBSD analysis less accurate.

Once the embedded Ti-6Al-4V samples destined for optical microscopy have been polished until no scratches remain visible, the final step of material preparation is applied. The material is etched in order to define the grains in the microstructure and make optical characterisation possible. Etching is done using Kroll's reagent as recommended by Reddy et al. [49]. The composition used for Kroll's reagent is 100 ml H_2O, 1 ml HF and 2 ml HNO_3. Kroll's reagent is applied to the specimen by continuously wetting the surface with the reagent using a swab over the course of 40 seconds. The sample is then immediately flushed with 2-isopropanol and inspected. Due to the etchant deteriorating over time, samples etched at a later date might require additional swabbing steps of only 10 seconds at a time to avoid overetching. Once the grains are clearly visible under an optical microscope the etching process is finished.

3.1.3. Microstructure and crack analysis

Due to the scale of the microstructure, crack path and microstructural features, several techniques are used to identify all relevant data. The microstructure measurements are applied using different methods for the different types of grains. The prior β grain size and the α colony size are measured using a line method, applied on micrographs obtained by optical microscopy. In the line method, a line of known length is drawn onto the micrograph and the number of grain boundary intersections is counted. By dividing the line length over the number of intersections, an average grain size is obtained. For the α lamellae thickness, an ellipse method is applied to a micrograph obtained using a SEM. In the ellipse method, ellipses are manually drawn around several randomly chosen lamellae. The thin radii of these ellipses are averaged in order to obtain the average lamellae thickness.

During and after the experimental many data sets are retrieved using several methods, these data sets must then be processed using different software in order to retrieve the desired data. This starts with an analysis of the crack growth during the experimental. The crack growth data will then be processed and fitted to a Paris diagram. The final cracks and microstructural features around them also need to be scanned using several characterization methods in order to obtain information about the microstructural features present.

During the load shedding described in Table B.1 and Table B.2 (Appendix B), the crack growth is observed by optical microscopy. In between load steps, the sample is removed from the test set-up

and the crack growth is recorded using an optical microscope and a micrograph is captured such as shown in Figure 3.2.

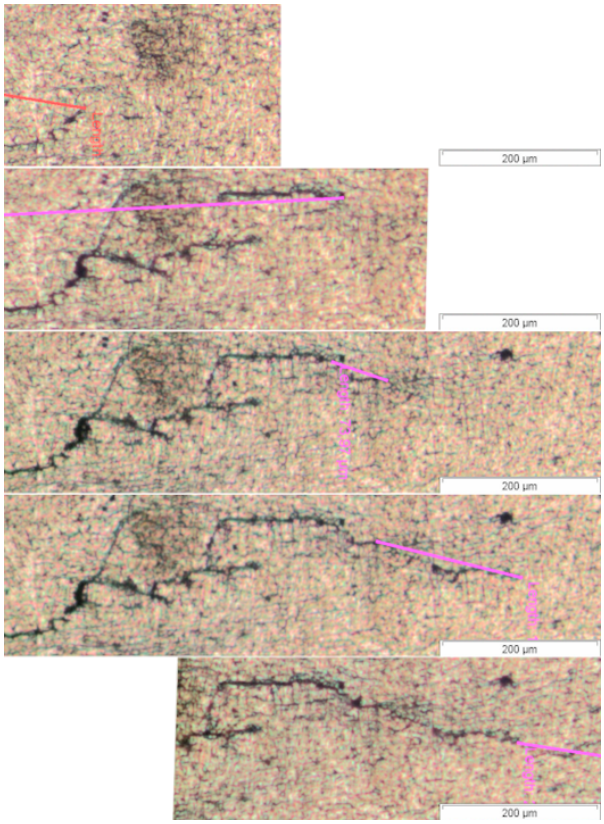

Figure 3.2: Five crack propagation steps on the same sample showing the crack propagation and measuring method.

By superimposing these micrographs for each individual growth step, a map of the crack propagation steps can be created. This allows for a final inspection of the crack growth after the experiment is complete to confirm the results obtained from the experiments. From Figure 3.2 it becomes clear there is an inaccuracy in the measurements of the crack propagation using this method. Due to the resolution of the optical microscope used, the minimum crack growth observed is 5 µm.

Once the samples are fully tested, one sample from each of the $R = 0.1$ and $R = 0.7$ sets is further examined using SEM and EBSD methods. Unfortunately, due to the long preparation and scanning times of EBSD, not every sample can be analyzed this way. The SEM used is a JSM-IT100 and the EBSD analyses are conducted in a JEOL JSM-7900F and a Helios G4 CX. These characterization methods require a smaller sample size of around 20 mm by 20 mm and therefore require the samples to be deconstructed. After an extensive polishing period of 2 hours using OP-S on MD-CHEM cloth, the samples can be analysed further. The resulting sample is shown in Figure 3.3.

The SEM images are made using a retractable Robinson-type backscatter detector (BED-C) at an energy of 10 kV. For crack path analysis, a zoom of 1800x was used where for lamellae width measurements this zoom was increased to 4000x. The instrument used for XRD measurements is a Bruker D8 Advance diffractometer with $CuK\alpha$ radiation (45 kV, 40 mA), using a step scan mode with the step of 0.040° (2θ) at 2 seconds per step.

The SEM analysis is combined with an EDS analysis to obtain a detailed overview of the elements present. Furthermore, the entire crack is mapped in great detail in order to perform an optical examination of the grain morphology around the crack. The optical examination is then combined with grain size measurements performed using an EBSD analysis to confirm the results. The EBSD analysis will also uncover the various crystallographic properties of the grains. These properties are related to the crystallographic orientation of the grains and can have a large influence on the crack path. The most influential crystallographic properties are the Schmid factor and the misorientation angles at the grain boundaries since these determine the stresses needed to propagate the crack intergranularly or

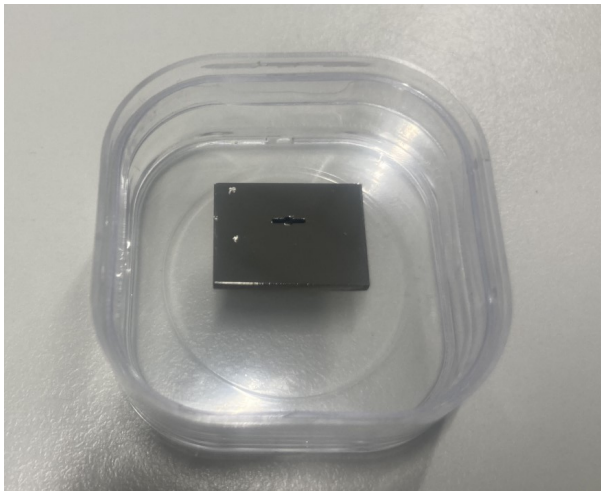

Figure 3.3: A 20 mm by 20 mm sample as prepared for EBSD analysis with two marks present for orientation identification.

transgranularly [41].

For the EBSD analysis a step size has to be determined, this step size determines the resolution of the data acquired. The step size is ideally as small as possible in order to uncover the most data. A smaller step size also leads to a higher amount of points scanned, which increases the scanning time. Therefore a step size must be determined which shows all desired data within a reasonable scan time. The smallest features which should be visible are the α lamellae with an average thickness of 2 µm. When these lamellae are displayed as 10 data points thick, all lamellae within the material are distinguishable. Therefore the step size which will be used during EBSD analysis is 0.2 µm. At this step size however, a full scan of the crack would result in significant scanning times when the JEOL SEM is used. This is due to the JEOL SEM achieving an identification rate of 80% at a scan time per point of 90 ms. Therefore a different SEM (Helios) is used for to create an overview of the crack at a scanning time of 20 ms per point. The resulting identification rate of the Helios scan is only 25% which makes the data unusable for proper identification of the microstructural features. The Helios scan is therefore used to define regions of interest which can then be further analysed using a JEOL scan.

3.2. Fatigue testing design

Once the material is properly treated, the dog bone shaped samples with dimensions shown in Appendix A, produced by EDM are prepared for testing. This testing requires a reliable test set-up and matrix, which must be designed according to the requirements set. In order for representative and repeatable results to be generated, this set-up must be sturdy and non-restrictive. The test matrix is designed specifically for the specimen size used in the present.

3.2.1. Fatigue test sample preparation

Before any testing is conducted, the dog bone shaped samples must be prepared in order to retrieve representative data. During the heat treatment process two additional processes occurred. First, the annealing envelopes were not able to fully prohibit an oxide layer from forming, this formed layer was therefore sanded away manually using P800 and P2000 grit sandpaper respectively. The samples were then etched around the stress concentration, using the same method as described in subsection 3.1.2. This step is done to improve visibility of the crack during testing. Second, the samples did warp during the heat treatment. This warping is reversed using a 4-point bending set-up as seen in Figure 3.4. The reversal of the warping using bending can induce cracks around the designed stress concentration but in optical analysis no cracks were observed.

3.2.2. Fatigue test set-up Design

The design process of the fatigue crack propagation experiments of the current research are a result of the dimensions of the provided raw material and the limitations of the clamping system of the MTS500 machine used for the fatigue testing. Due to the material having a thickness of 2 mm, a three/four point

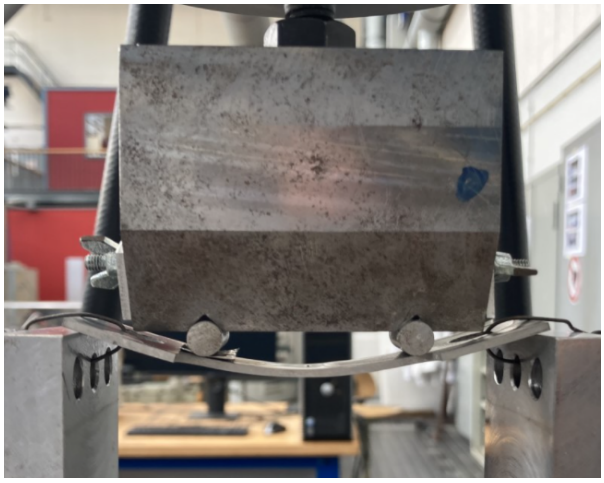

Figure 3.4: 4 point bending used to reverse the warping after heat treatment.

bending test is no longer applicable. The decision was therefore made to design for a tensile specimen. By inducing a crack in the middle of the specimen, the total amount of cracks grown and observed is doubled as a result of the cracks growing in two directions. This finally results in the decision to design the specimens as middle tension specimens according to E647 ASTM standard [50]. Clamps which allow for automatic alignment of the specimen to force direction applied by the testing apparatus were custom designed. These clamps were designed as four separate parts, joined by four pins allowing for an automatic alignment as shown in Figure 3.5. These clamps are fully modelled using FEM software and under the maximum applied force. The FEM models resulted in no significant stresses being reached in the clamps, therefore the assumption is made that these clamps will be able to endure all fatigue tests planned.

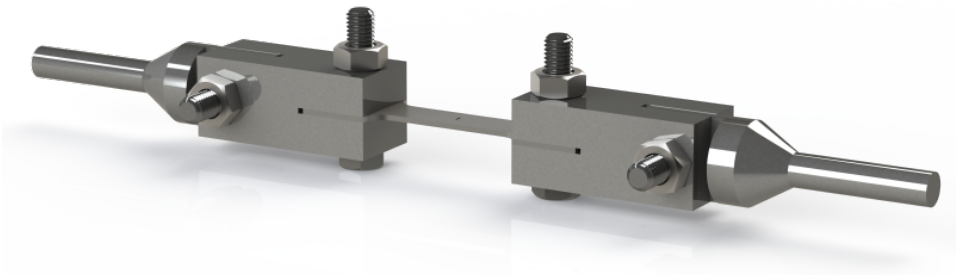

Figure 3.5: Render of clamps with MT specimen included with dimensions shown in Appendix A.

As for the specimen design, in order to ensure valid results the recommendations according to the E647 ASTM standard for middle tension specimens is followed [50]. In order to ensure crack growth at the desired location at the stress concentration, a dog bone shape was adopted. According to a finite element analysis using Solidworks 2021 the yield stress will never be exceeded in the specimen other than at the designed stress concentration, as shown in Figure 3.6.

The clamps shown in Figure 3.5 are combined with the experimental sample using two M10 bolts. This entire system is then clamped in the MTS500 universal testing machine as seen in Figure 3.7. The MTS500 universal testing machine has easily releasable clamps for fast removal of the sample for

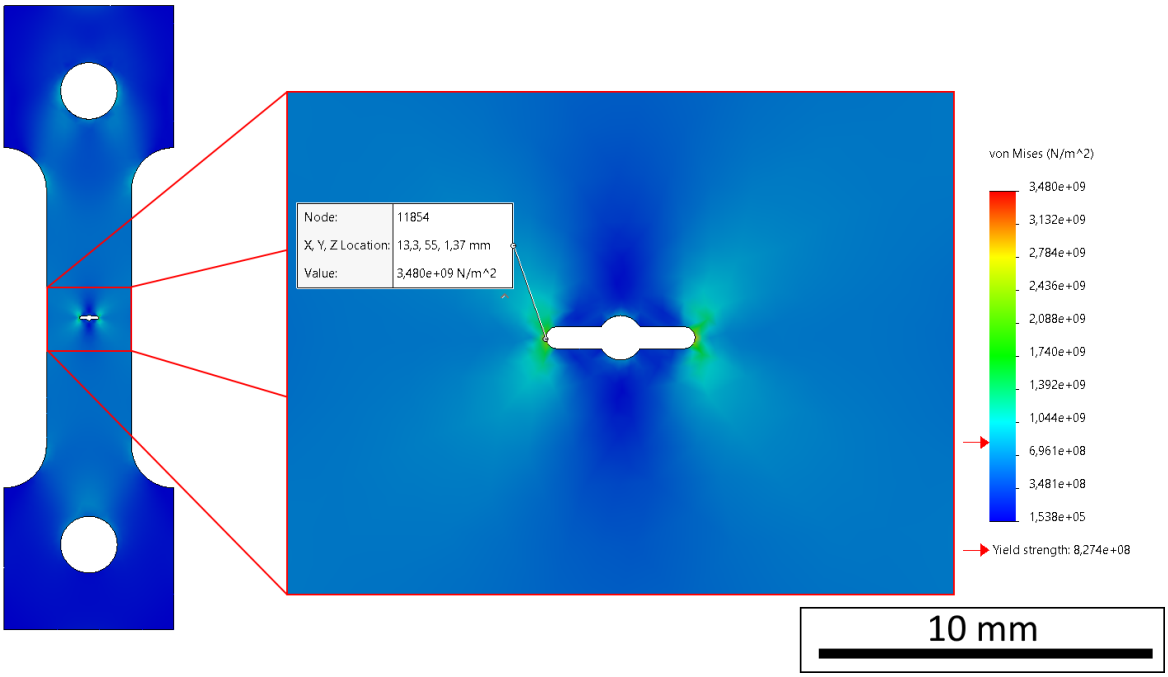

Figure 3.6: Von Mises stresses at a maximum load of 17.3 kN during testing.

optical examination during the experimentals.

3.2.3. Fatigue test matrix design

The method by which the load is applied to the material during fatigue testing has a large influence on the crack growth mechanics. The three testing parameters explained in section 2.3 can have an influence on the fatigue crack propagation during the experiments. The MTS500 universal testing machine requires the following three parameters as input: the frequency, number of cycles and the range of force applied by means of a mean force and a force amplitude.

The frequency of the load variation is a parameter which can have a large influence on fatigue properties of certain materials. This is mostly related to oxide-induced crack closure effects in materials which quickly generate an oxide layer in the testing atmosphere. This effect is negligible in Ti-6Al-4V however, as a result of the low oxidation rates of Ti-6Al-4V in a standard atmosphere at room temperature. The load cycle frequency of the experiments will therefore be determined by a combination of safety and speed. A frequency of 10 Hz creates the safest environment with repeatable results and manageable test times.

In order to determine mean force and force amplitude applied for each step of the experimental, the desired stress intensity range has to be outlined. The stress intensity range ΔK applied to the sample can have an influence on the crack path observed. Therefore ΔK is varied over the experiment in order to observe the effects of ΔK on the crack path. Since this material is specifically designed for the current research, the Paris diagrams are constructed for both R-ratios tested. The creation of these Paris diagrams helps identify the near-threshold stress intensity range ΔK_{th}. These tests are normally conducted using a load-shedding method described by [50]. This method allows for an accurate determination of ΔK_{th} values as the load is gradually lowered until the crack growth rate has dropped below $10^{-10}\mathrm{m}/\mathrm{cycle}$, at which point the crack will be considered as having stopped propagating. This method should result in a crack consisting of a range of propagation sections, all resulting from different stress intensity ranges. These cracks will thus provide an overview of the influences of the different stress intensities on the crack path.

In order to construct the Paris diagrams, an estimation for the crack growth rates for different stress intensity ranges is made using the Paris diagrams constructed by Jeong et al. [14]. These stress intensity ranges first have to be translated to a stress range however. This is done using the following formula [50]:

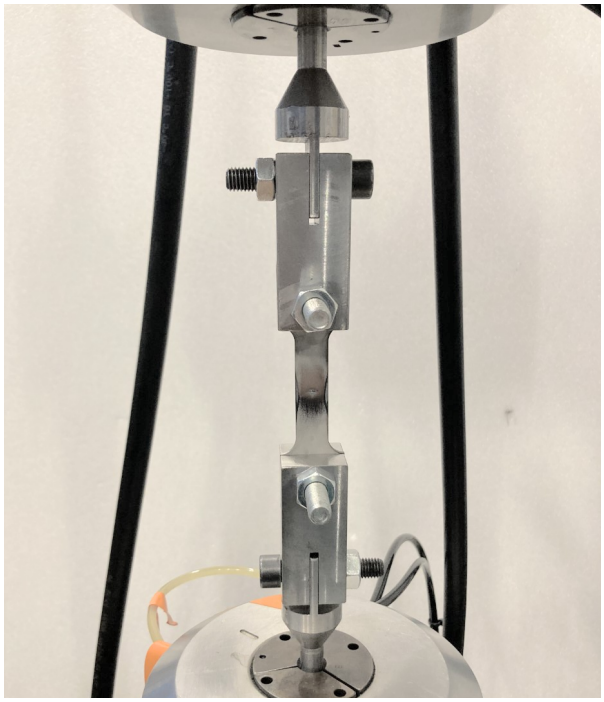

Figure 3.7: Test set-up as used in MTS500 universal testing machine.

$$\Delta K = \frac{\Delta\sigma}{B}\sqrt{\frac{\pi\alpha}{W}\sec(\pi\alpha)} \tag{3.1}$$

Where ΔK is the stress intensity range and $\Delta\sigma$ is the stress range. The values B and W are the thickness and the width of the sample. Finally, α is $2a/W$ which is a ratio of the total crack length a and the width W. Solving Equation 3.1 for $\Delta\sigma$ gives the stress range which needs to be applied. The stress range can then be transformed to the force range by multiplying the stress by the area on which it acts. Since the input parameter of the MTS500 universal testing machine requires the force amplitude, the force range is divided by two:

$$F_{amplitude} = \frac{\Delta\sigma * (W - 2a) * B}{2} \tag{3.2}$$

The area in Equation 3.2 is the width W of the specimen minus the total crack length $2a$, times the thickness B. Finally, the minimum, maximum and mean force can be obtained from the force range by solving for the different R-ratios applied, according to:

$$\begin{aligned} F_{min} &= \frac{2 * F_{amplitude}}{\frac{1}{R} - 1} \\ F_{max} &= \frac{2 * F_{amplitude}}{1 - R} \\ F_{mean} &= \frac{F_{min} + F_{max}}{2} \end{aligned} \tag{3.3}$$

The R-ratio has a large influence on the Paris diagram and therefore two different sets of tests will be conducted, one set with an R-ratio of 0.1 and one set with an R-ratio of 0.7. This will provide one set of samples with little to no roughness-induced crack closure and one with this effect. This will be critical to confirm the validity of the conclusions drawn from the current research.

The number of cycles required for a crack propagation of 200 µm is estimated from the results obtained by Jeong et al. [14] for the crack propagation rates of Ti-6Al-4V shown in Figure 3.8. At each applied stress intensity range this number of cycles is determined which results in a test matrix which

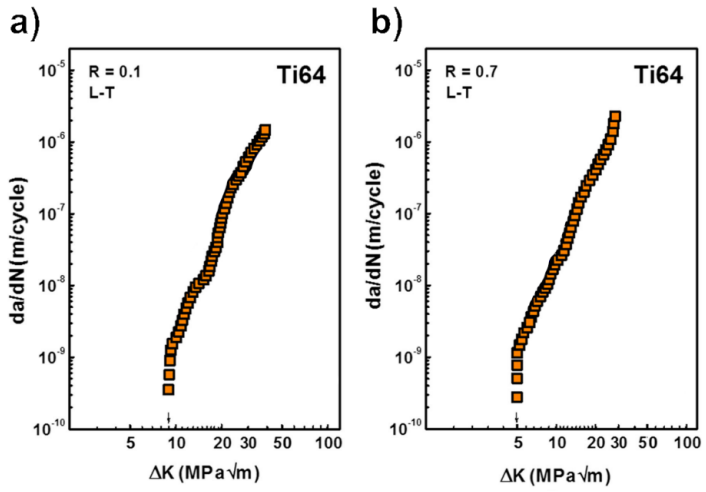

Figure 3.8: Test results from load shedding method by Jeong et al. used for estimating the crack growth rates in the current research [14].

can be used during the load shedding, these test matrices are shown in Appendix B. The order of the steps is critical since the total crack length achieved in each step is used for the calculations of the stress intensity range of the next step. Due to the stochastic character of crack propagation rates, the expected number of cycles is not always the number of cycles used in the test. When the crack propagation rate deviates from the expected value, the test duration will be adjusted accordingly. This process is clearly seen in the resulting test matrix shown in Appendix B.

Before the propagation stage is reached however, a crack must be initiated. This is done using the same mean force and amplitude across all samples, including both $R = 0.1$ and $R = 0.7$. The decision was made to initiate the crack at an R-ratio of $R = 0.1$ with an initial stress intensity range of 15 MPa$\sqrt{\text{m}}$. At this ΔK the crack propagation rate is low and therefore the crack length is easy to monitor. The minimum length of this initial crack is defined by ASTM standard E647 [50]. When two lines are drawn from the tip of the crack to two coincidence points on the slot, indicated by the green lines in Figure 3.9, the angle must be lower than 30 degrees, this ensures no effect of the machined notch on ΔK. The minimum required crack length to fulfill this requirement is 716 µm. The initiation step will thus be considered complete when all cracks have reached this initial length.

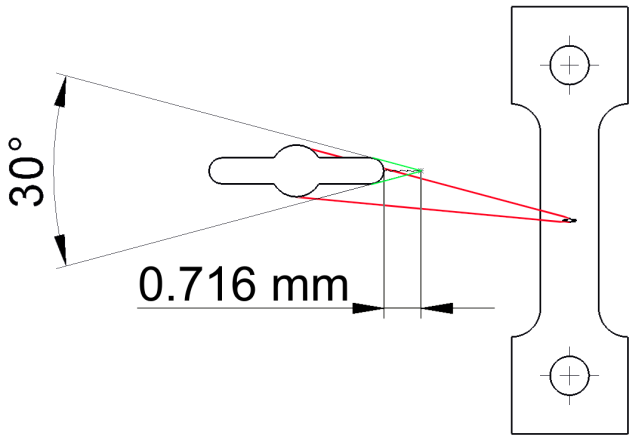

Figure 3.9: Schematic drawing of stress concentration slot in dog bone shaped samples showing the initial crack length required.

4

Results and Discussion

The Ti-6Al-4V samples have been prepared and tested using the methods described in chapter 3. The heat treatment applied has resulted in the desired microstructure. The characteristics and properties of this microstructure are shown and discussed in section 4.1. These samples were tested using the previously described load shedding method, which resulted in fatigue cracks of which the propagation rates are processed and analyzed in section 4.2. The crack paths are analysed using two different EBSD techniques which results in imagery of the microstructural features around the fatigue cracks, of which the results are shown in section 4.3. Finally, the effects of the microstructural features on the fatigue crack path are characterized. The effect of the microstructural features is expressed as a probability for the crack to bifurcate or deflect. These probabilities are a function of both the microstructural features and the load case applied which are described in section 4.4.

4.1. Effect of heat treatment on the microstructure

The resulting microstructure and its mechanical properties are a combination of the chemical composition, the processing of the material and the heat treatment of the Ti-6Al-4V samples. In order to discuss the expected microstructures, knowledge of the chemical composition of the material is required. The alloying elements in Ti-6Al-4V have a large influence in the formation of the α and β phase as has been described in subsection 2.1.1. The alloying elements in the base material are not known to an accurate enough degree since no information on the composition is given by the supplier. An Energy-dispersive X-ray spectroscopy (EDS) scan has therefore been performed on the material. This EDS scan has been done over an area of 128 µm by 104 µm. The depth of this scan is determined using the Kanaya-Okayama model [51]:

$$R = \frac{27.6 * A * E_0^{5/3}}{Z^{8/9} * \rho} \tag{4.1}$$

Here, the penetration depth R (nm) is calculated using the atomic mass A (u), the incident energy E_0 (keV), the atomic number Z and the density ρ $(g * cm^{-3})$. Using the atomic properties of titanium, the penetration depth is calculated to be 0.9 µm at an incident energy of 10 keV. The total volume measured using EDS is then $1.2 * 10^4 \mu m^3$. The net counts of the elements found in this volume are shown in Table 4.1.

Table 4.1: Net counts and weight percentages with a standard deviation found in base material used in the current research using EDS.

Element	Ti	Al	V
Net count	2730619	197077	115291
Wt%	89.70 ± 0.07	6.48 ± 0.02	3.79 ± 0.03

The chemical composition lies within the limits of what is considered a grade 5 titanium alloy [4]. With the chemical composition confirmed, the effect of the heat treatment on the microstructure can be analyzed.

The morphology of the grains has a large influence on the fatigue properties of the material. As described in subsection 2.1.2, a lamellar α microstructure will provide the most resistance to fatigue crack propagation. This lamellar α microstructure is achieved by the heat treatment described in subsection 3.1.1. Before this heat treatment can be applied, it is important to identify the grain morphology of the base material. The morphology of the base material can still affect the microstructure after heat treatment as the boundaries of the β grains in the base material can influence the α-formation, after a heat treatment above the β transus temperature is applied [52]. The microstructure of the base material was observed using optical microscopy and found to be fully equiaxed. A micrograph showing the equiaxed microstructure of the base Ti-6Al-4V is shown in Figure 4.1. The black regions indicate transformed β where the light regions indicate primary α [53].

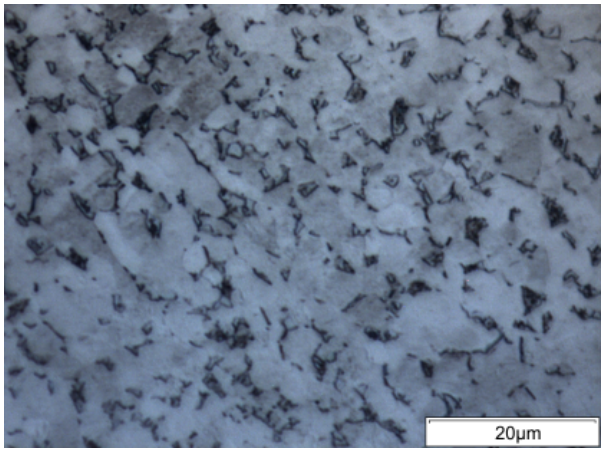

Figure 4.1: Micrograph showing microstructure of the base Ti-6Al-4V material provided by Titanium Services [45].

The first analysed property of heat treated microstructure is the phase distribution. The heat treatment used in the current research, designed by Jeong et al., is designed to produce a lamellar fully α microstructure [14]. The expected phases are therefore α with little to no β present. The phase distribution of the heat treated sample is measured using both an X-ray diffraction (XRD) and an Electron backscatter diffraction (EBSD) method. First, during the XRD analysis a clear majority of α phase is seen in Figure 4.2. There are however, some unidentified peaks at a 2θ of 39° and 56°, indicated by blue peaks in Figure 4.2. The lattice parameter of the β-Ti has been slightly altered to fit these blue peak positions. No assumption can be made from the XRD results about the phase distribution apart from the presence of α-Ti.

In order to further investigate phase distribution after the heat treatment, a phase map was created using EBSD analysis. This phase map, shown in Figure 4.3, shows the phases present in two different colours. The α phase is shown in red and the β phase is shown in blue. Some β phase is observed in the figure.

From the data used to create Figure 4.3, a table is made in order to show the α and β phase fractions. These results are shown in Table 4.2.

Table 4.2: Phase distribution results of EBSD analysis of heat treated Ti-6Al-4V sample.

Phase	Composition [%]
Ti-Hex (α)	99.95
Ti-Cubic (β)	0.05

The amount of β phase found lies within the same range of error found by Nolze and Winkelmann where 0.07% of phase was erroneously assigned [54]. From Table 4.2 it can therefore reasonably be assumed there will be no influence of β phase on the fatigue crack growth and the material will therefore be treated as fully α.

After the heat treatment described in subsection 3.1.1 is applied to the material, the morphology has changed significantly. Figure 4.4 shows a cross-section of a heat treated dog bone sample after etching, using the method described in subsection 3.1.2.

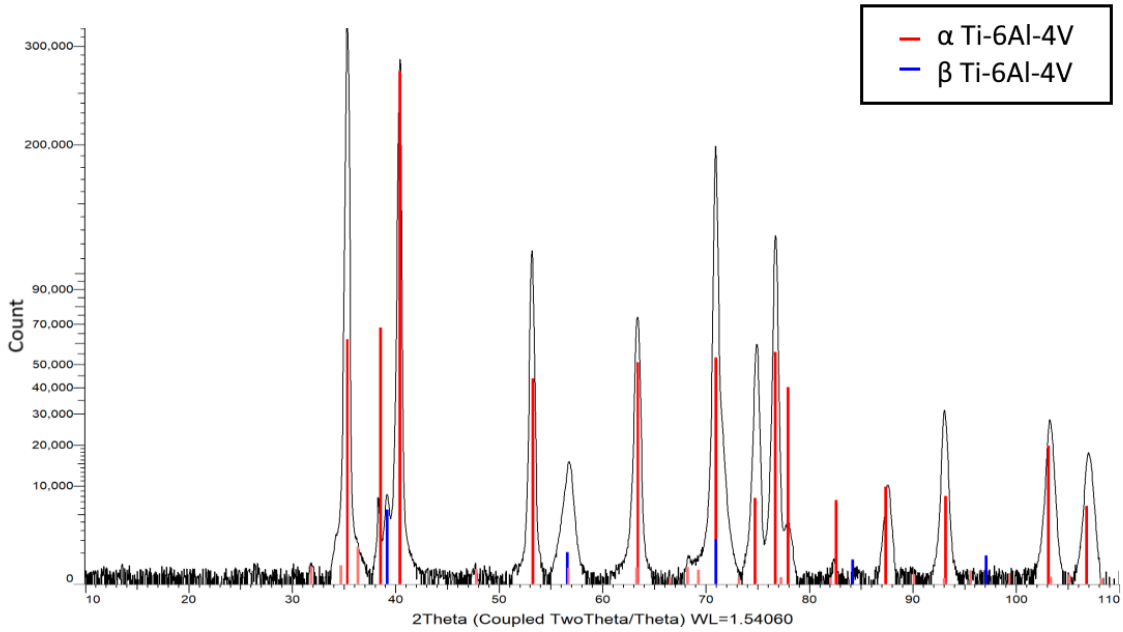

Figure 4.2: XRD results of heat treated Ti-6Al-4V where the β lines have been slightly altered to fit the peak positions.

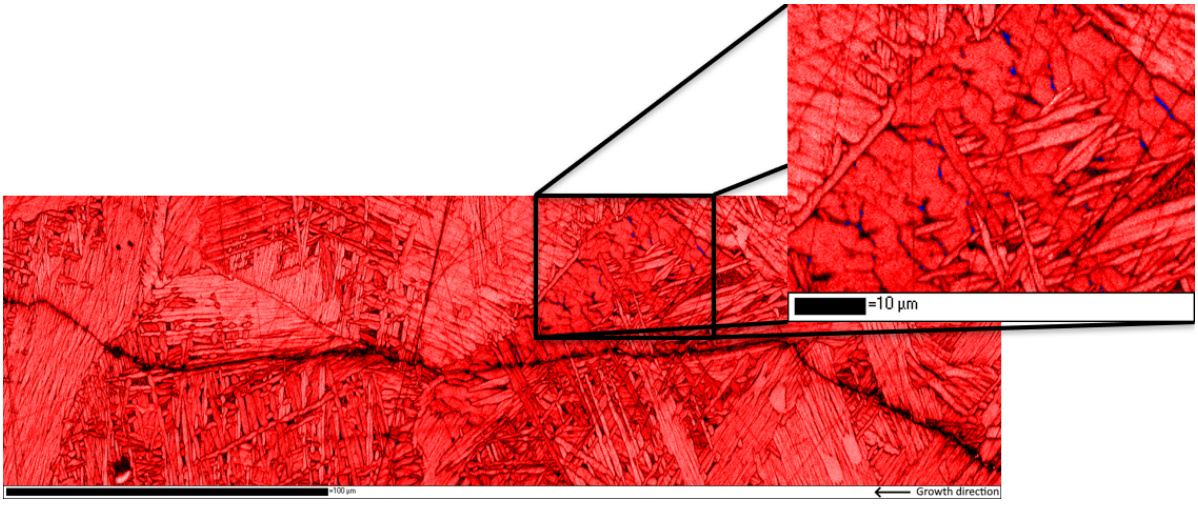

Figure 4.3: EBSD results at a step size of 0.2 µm overlaying the identified phases over the band contrast where red depicts the α and blue depicts the β phase.

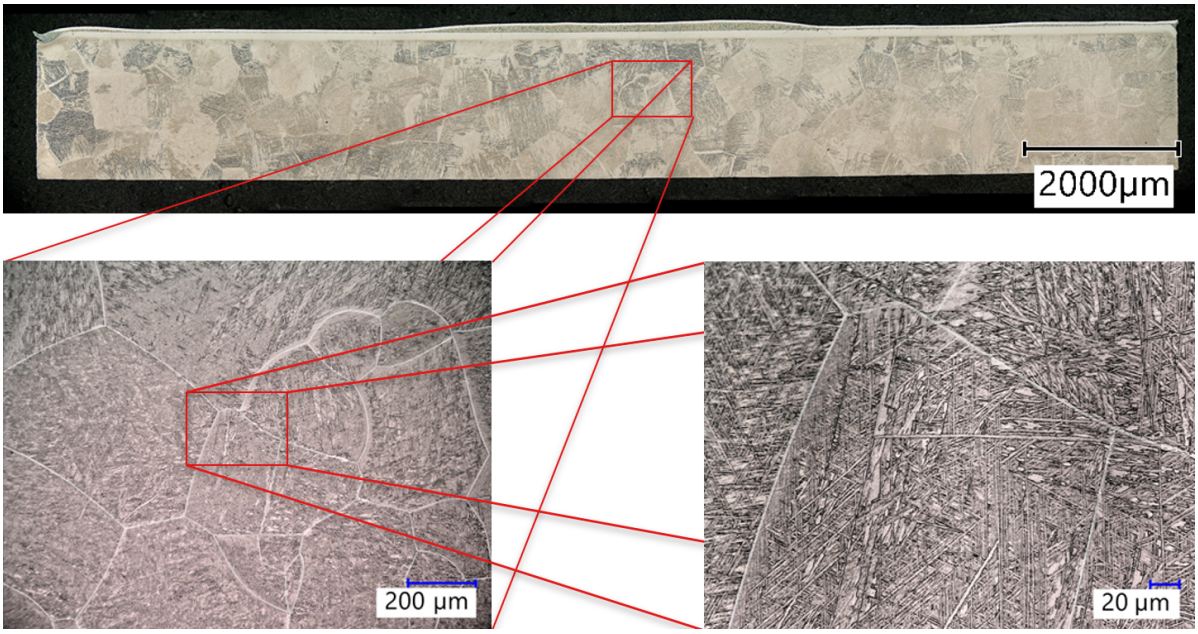

Figure 4.4: Series of increasingly zoomed in optical micrographs of the cross-section of a heat treated dog bone sample, note that the prior β grain boundaries are highlighted in white.

The first in the series of micrographs shown in Figure 4.4 shows an overview of large prior β grains in the cross-section. The second micrograph shows a clear overview of the shape and size of these prior β grains. Finally, the micrograph at the smallest scale shows the lamellar α grains located within the prior β grains. Due to the thickness of the α lamellae being so small, scanning electron microscopy (SEM) is required to observe the thickness. A SEM image is shown in Figure 4.5 where the α lamellae thickness is more clearly visible.

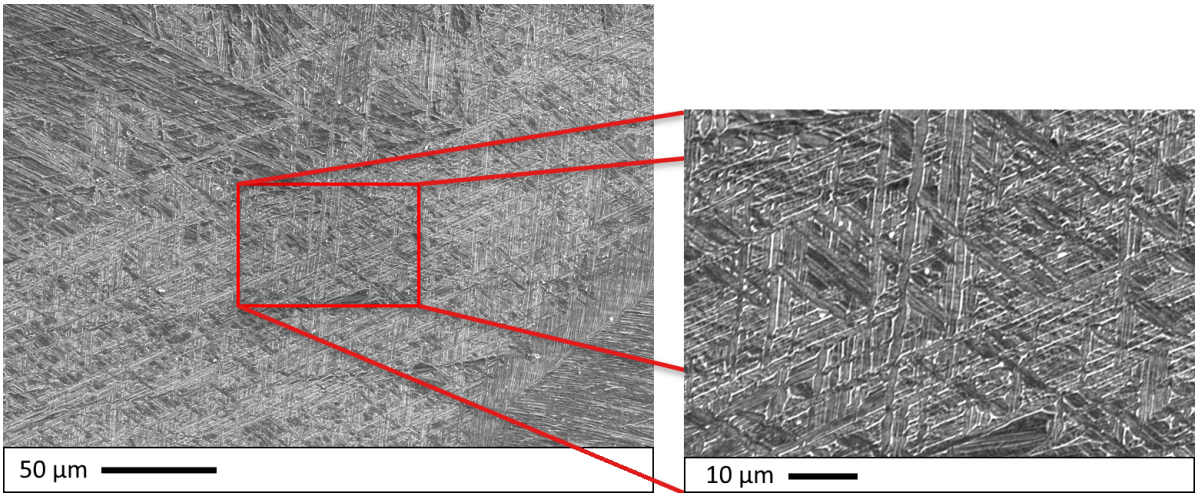

Figure 4.5: SEM image of the heat treated Ti-6Al-4V showing the α lamellae in the microstructure.

The grain sizes shown in Table 4.3 within the microstructure have a large influence on the fatigue crack propagation in the material as a larger grain size increases the roughness-induced crack closure [31]. The size of the grains also determines the density of grain boundaries present, which has a large influence in determining the fracture mode during fatigue crack growth [39]. The grain sizes are therefore determined using the method described in subsection 3.1.3. The three measured parameters are the prior β grain size, the α colony size and the α lamellae thickness. The three types of boundaries mentioned are highlighted in Figure 4.6.

The resulting grain sizes from the measurements are shown in Table 4.3. Both the prior β grain size

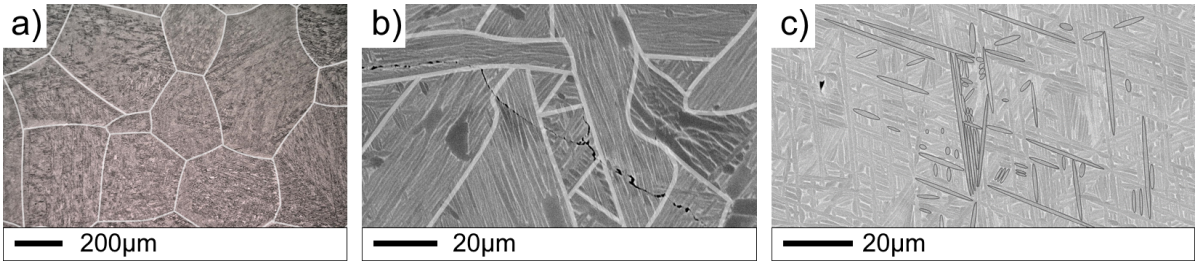

Figure 4.6: Micrographs showing the prior β grain boundaries in white (a), the α colony boundaries in white- (b) and the α using an ellipse approach (c).

and the α lamellae thickness are similarly sized in the current microstructure when compared to the β annealed Ti-6Al-4V analyzed by Jeong et al. [14]. The α colony size, however, was found to be smaller by a factor 2 in the current microstructure when compared to the colony size found by Jeong et al., where an average α colony size of 84 µm was found. This difference is attributed to the determination method of the colony size as SEM imaging of the β annealed Ti-6Al-4V analyzed by Jeong et al. [14] reveals colonies of the same size.

Table 4.3: The average grain size measured for the heat treated Ti-6Al-4V with standard deviation

β grain size $[\mu m]$	α colony size $[\mu m]$	α lamellae thickness $[\mu m]$
380 ± 40	34 ± 8	1.2 ± 0.1

Finally, the difference in microstructure before and after the heat treatment should be reflected in a difference in hardness. An increase in hardness is expected due to the formation of a fully α microstructure, which is in general harder and more brittle when compared to the ductile β microstructure [11]. Hardness measurements in the form of a Vickers' hardness test are performed on the as received equiaxed material and on the β annealed lamellar α material. The results of these tests are shown in Figure 4.7.

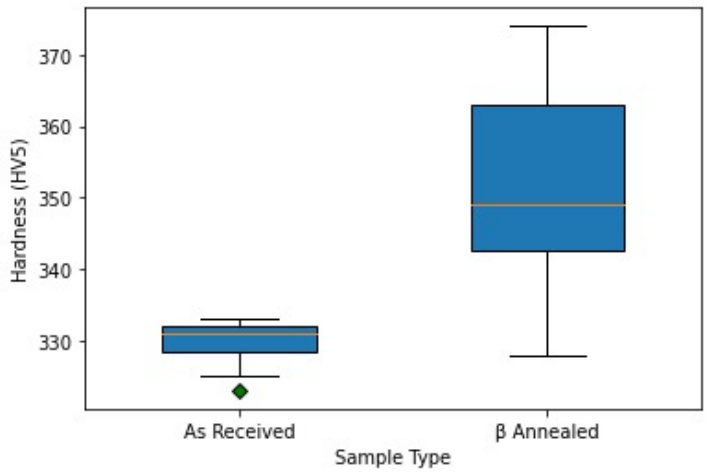

Figure 4.7: Vickers' hardness test results comparing the hardness of the as received sample to the beta annealed sample.

A clear increase in hardness is shown post heat treatment with the average hardness increasing from 332 HV to 349 HV. The larger spread of the β annealed hardness is attributed to the larger grain size when compared to the as received material. At a larger grain size, the hardness test can sometimes completely avoid grain boundaries or encompass a large number of grain boundaries, creating a deviation in the hardness results. The spread found in the β annealed hardness is however, small enough to indicate a homogeneous microstructure throughout the sample.

4.2. Crack propagation

The load shedding method described in subsection 3.2.3 has been applied to four samples at an R-ratio of 0.1 and to four samples at an R-ratio of 0.7. During these tests, from 4 to 10 crack propagation steps were recorded using optical microscopy. These micrographs were used to determine the stress intensity range and crack growth at every step. This was done by overlaying the intermediate micrographs on top of an image of the final crack. The resulting crack is then highlighted and the stress intensity range at every step is indicated. Figure 4.8 shows the crack path at several stress intensity ranges with an R-ratio of 0.1. There is no clear relation visible between the applied stress intensity range and the crack path. If there is any influence of the stress intensity range on the crack path, it could become more visible when the scale is drastically decreased or different visualization techniques like EBSD are applied.

Figure 4.8: Overview of the crack path and the accompanying stress intensity range of crack 1 out of 4 on sample 1, tested at an R-ratio of 0.1

Figure 4.8 does not provide any information on the rate at which the crack has propagated. The crack propagation rates have been recorded in the form of distance per cycle, indicating the crack growth in meters per cycle. These values can then be plotted against ΔK to create a Paris diagram which is shown in Figure 4.9. The green step in Figure 4.8, for example, shows a smaller propagation rate for a similar ΔK in Figure 4.9 when compared to the yellow step. This indicates that there is an influence of some microstructural features that creates this deviation in crack propagation rates. This influence of microstructural features would also explain the large spread in the data.

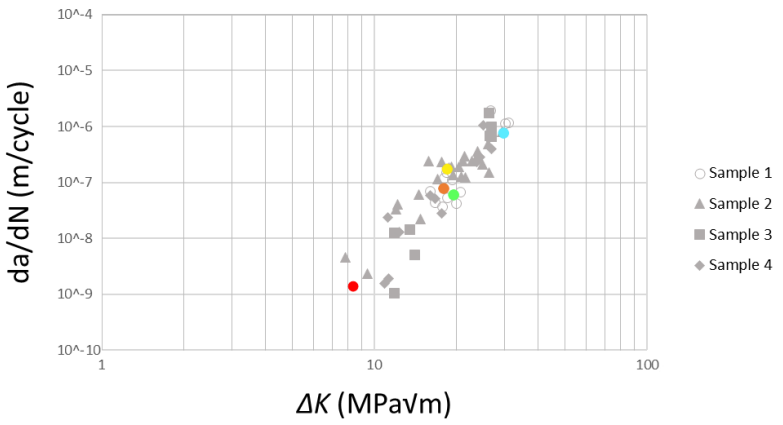

Figure 4.9: Paris diagram showing the crack propagation rates for the stress intensities tested at an R-ratio of 0.1. The crack propagation steps of Figure 4.8 are highlighted in the graph using the same color scheme.

At a double logarithmic scale, the results of the load shedding method for an R-ratio of 0.1 can be fitted using an exponential function with an R^2 value of 0.60:

$$\frac{da}{dN} = 4 * 10^{-14} \Delta K^{5.0} \tag{4.2}$$

The resulting Paris constants for an R-ratio of 0.1 from Equation 4.2 are determined to be $C = 4 * 10^{-14}$ $^{m}/_{(cycle*MPa\sqrt{m})}$ and $m = 5.0$.

Figure 4.10 shows a similar figure to Figure 4.8 but at an R-ratio of 0.7. Due to the lower overall crack growth of each visible step, more steps could be applied at different stress intensity ranges. During the green propagation step, indicated with a ΔK of 9.6 MPa$\sqrt{\text{m}}$, the propagation was so little, there was a debate whether the crack was propagating at all. The stress intensity has therefore been temporarily increased as can be seen by the sudden jump in ΔK to 15.8 MPa$\sqrt{\text{m}}$ in the yellow region.

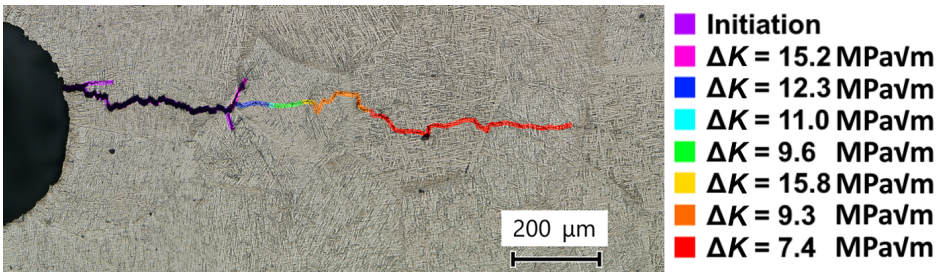

Figure 4.10: Overview of the crack path and the accompanying stress intensity range of crack 4 out of 4 on sample 5, tested at an R-ratio of 0.7.

Figure 4.10, much like Figure 4.8, does not show a clear indication to an influence of the applied stress intensity range to the crack path. The effect of the different R-ratios is also not clearly visible on the scale shown. The only apparent difference between the R=0.1 and R=0.7 cracks is the width of the initial crack. This difference is attributed to the higher peak force applied when the R-ratio of 0.7 is tested. The peak force of 17.3 kN translates to a stress on the cross-section of the sample of 880 MPa, which is the only stress applied during the experimental surpassing the yield strength of β annealed Ti-6Al-4V at 867 MPa [14]. This leads to an elongation of the sample and a significant widening of the crack.

The values for the crack growth rates at an R-ratio of 0.7 are plotted over the applied stress intensity range in order to construct another Paris diagram in Figure 4.11. An even larger spread in results is found in Figure 4.11 when compared to Figure 4.9. The change in spread is attributed to the smaller propagation rates. The smaller propagation rates result in lower crack growth per step and therefore small discrepancies between the steps are more visible.

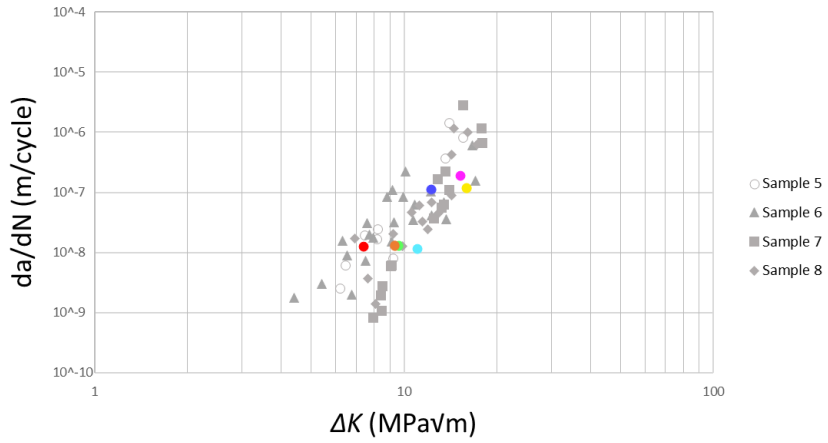

Figure 4.11: Paris diagram showing the crack propagation rates for the stress intensities tested at an R-ratio of 0.7. The crack propagation steps of Figure 4.10 are highlighted in the graph using the same color scheme.

The results from the load shedding method shown in Figure 4.11 are fitted to an exponential equation with an R^2 value of 0.39:

$$\frac{da}{dN} = 2 * 10^{-14} \Delta K^{6.2} \tag{4.3}$$

The resulting Paris constants of the material tested at an R-ratio 0.7 differ from those tested at an R-ratio of 0.1. The Paris constants have been determined to be $C = 2 * 10^{-14}$ $^{\text{m}}/_{(\text{cycle}*\text{MPa}\sqrt{\text{m}})}$ and

$m = 6.2$ for an R-ratio of 0.7. The results for an R-ratio of 0.1 and 0.7 are shown in Table 4.4.

Table 4.4: Comparison of the Paris constants found in the current for an R-ratio of 0.1 and 0.7 in Ti-6Al-4V.

R-ratio	0.1	0.7
C $[^{m}/_{(cycle*MPa\sqrt{m})}]$	$4 * 10^{-14}$	$2 * 10^{-14}$
m	5.0	6.2

Despite the influence of the different R-ratios not being clearly visible in Figure 4.8 and Figure 4.10, a clear difference in crack propagation rates between the R-ratios of 0.1 and 0.7 has been observed in the Paris diagrams. The fits of both Paris diagrams are combined into Figure 4.12.

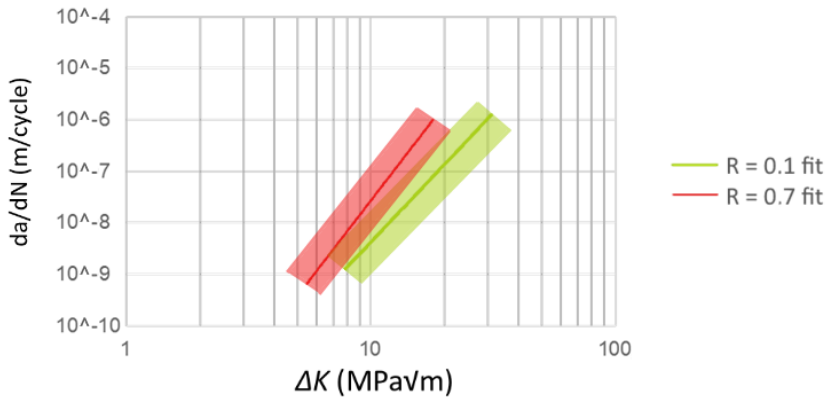

Figure 4.12: A comparison between the fits of the Paris diagrams of an R-ratio of 0.1 and 0.7 with a 95% confidence fit highlighted in the respective colors.

A shift of the crack propagation rates as a result of a change in R-ratio is clearly visible in Figure 4.12. As has been discussed in subsection 2.3.3, a shift to lower ΔK values in the Paris diagram is expected when the R-ratio is increased. Besides this shift, the slope of the fit also seems affected by the change in R-ratio. This change of slope has not been described by the effects discussed in subsection 2.3.3. This change of slope is most likely a result of a combination of the spread in the measured data and an underestimation of the fit in the near ΔK_{th} regime.

The shift to lower ΔK values in the Paris diagram for an increase in R-ratio is mostly attributed to crack closure effects. In β annealed Ti-6Al-4V this effect will mostly originate from the roughness-induced crack closure [38]. This roughness-induced crack closure should be detectable optically in the form of crack blunting. Figure 4.13 shows two micrographs where two cracks have propagated through an α colony along the direction of the α lamellae. These comparable cracks show one distinct difference in that the width of the crack is significantly larger in the crack where an R-ratio of 0.1 was applied.

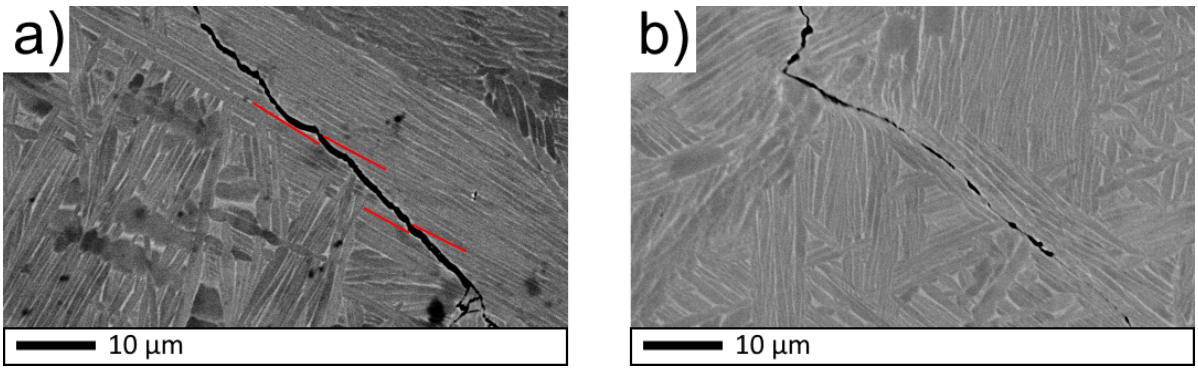

Figure 4.13: Crack propagation through an α colony along the direction of α lamellae in Ti-6Al-4V at an R-ratio of 0.1 (a) and an R-ratio of 0.7 (b).

The increase in crack width, due to the effect of roughness-induced crack closure, allows for a larger shift of the material on either side of the crack. This shift is most clearly seen by the discontinuation of the α lamellae boundaries in Figure 4.13a, highlighted in red. The misfit created by this shift will induce a larger effect of roughness-induced crack closure which will enhance the effect further.

It has been previously stated that the effects of crack closure have been overestimated in the past and could not fully account for the shift in crack growth rates observed. This would indicate that some other feature or parameter would be influenced by the change in R-ratios in order to fully account for the difference in observed crack growth rates. Apart from the effects of roughness-induced crack closure however, there is no clear indication of different crack growth behaviour between the two tested R-ratios. In the next sections the effect of the microstructural features and the load case on the crack path are further explored in an attempt to further explain the observed effects.

4.3. Microstructural features affecting crack path

Besides the effects of roughness-induced crack closure, there are several microstructural features which affect the fatigue crack propagation rate through the material. In the current section, the influence of these microstructural features on the crack propagation rate are related to the crack path. Each grain had a unique crystallographic orientation within the material which lead to distinct fatigue properties in each individual grain. The microstructural features which are examined in the current research are limited to the following three:

- Schmid factor
- Low angle grain boundaries (LAGB)
- High angle grain boundaries (HAGB)

A special distinction is made between LAGB and HAGB. The boundaries between α lamellae in are typically found to be at a low angles ($< 5^{\circ}$). The angles between prior β grains boundaries or α colony boundaries however, were found to be mostly high ($> 15^{\circ}$). By making this distinction, the effects of α lamellae thickness and α colony size can be separated.

In the current section, two methods by which the crack path is altered due to microstructural features are discussed. These two methods are deflection and bifurcation. Deflection is used as a term to describe a clear deviation of the crack from a straight crack path by means of intergranular cracking. Bifurcation is used to describe the formation of clearly observable secondary cracks, this requires a minimum secondary crack length of 5 µm due to the limitations of the used equipment.

4.3.1. Activated slip system in crack path due to Schmid factor

Besides the effect of the Schmid factor on altering the crack path, the Schmid factor also determines the active slip system during crack propagation. As has been described in subsection 2.5.2, the Schmid factor determines the active slip system used to propagate the crack during transgranular cracking. The shifting of slip systems allows for a crack, which would normally be deflected in a basal slip system due to a low Schmid factor, to shift to a prismatic slip system if a high Schmid factor is available. Therefore, a large deflection due to the Schmid factor should only be expected when the crystal orientation is such that for all slip systems a low Schimd factor results.

From Figure 2.14 it is apparent that there could be three different slip systems active, depending on the angle between the c-axis and the loading direction. Despite the range of angles of 0° to 10° showing that 1st order pyramidal slip is favourable, this was never found to be the active slip system when the crack path was analysed. The crack will only propagate when the resolved shear stress exceeds the critical shear stress value. The critically resolved shear stress of the pyramidal system is 2.5 times higher than that of the basal and prismatic systems and as a result, the resolved shear stress will never exceed the critical shear stress, so no pyramidal slip will occur [42].

The two cracks analysed using EBSD techniques in the current research are one sample tested using an R-ratio of 0.1 and one sample tested at an R-ratio of 0.7. The entirety of these cracks is first analysed using a Helios SEM. Due to the large scan area and small step size the scan time per point is low. This resulted in large detailed EBSD maps of both cracks at the cost of a high level of noise. Figure 4.14 and Figure 4.15 show the full cracks analysed using the Helios SEM. The colours in the image represent the highest Schmid factor detected, this includes both the basal and prismatic

slip systems. The same color scheme is used to identify the Schmid factor for the rest of the current research, a scale bar for these Schmid factors is shown in figs. 4.14 to 4.16.

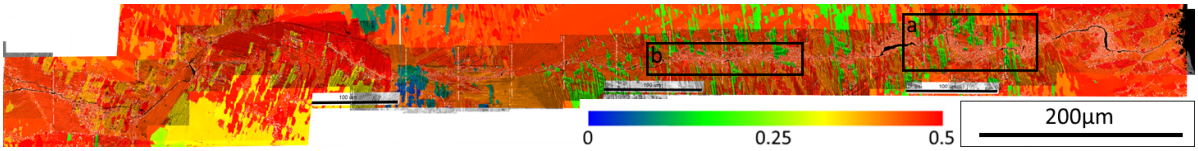

Figure 4.14: Helios image of the crack in the sample tested at an R-ratio of 0.1, the EBSD results are overlayed with SEM imagery to highlight grain boundaries further.

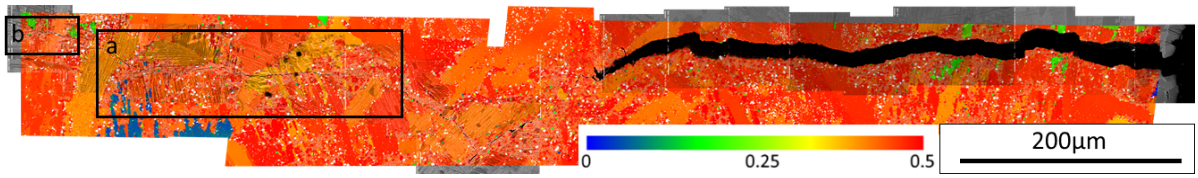

Figure 4.15: Helios image of the crack in the sample tested at an R-ratio of 0.7, the EBSD results are overlayed with SEM imagery to highlight grain boundaries further.

Figure 4.16: Coloured Schmid factor scale used for all Schmid factor maps by both Helios and Jeol EBSD.

Figure 4.14 and Figure 4.15 are used to identify areas of interest for further examination. The two areas chosen per sample are selected due to their high correlation between microstructural features. Areas a in both Figure 4.14 and Figure 4.15 indicate areas with relatively high ΔK values of 24 MPa$\sqrt{\text{m}}$ and 15 MPa$\sqrt{\text{m}}$ for the tested R-ratios of 0.1 and 0.7 respectively. Areas b indicate areas where a ΔK near the threshold was applied for both R-ratios.

The first area which is further examined is a of the sample tested at R=0.1, which was tested at a relatively high ΔK of 24 MPa$\sqrt{\text{m}}$. An EBSD scan using the Jeol SEM was performed in order to get a detailed image together with information about the crystallographic orientation of the grain. An image of the Schmid factors is shown for both the basal and the prismatic slip systems in Figure 4.17 and Figure 4.18.

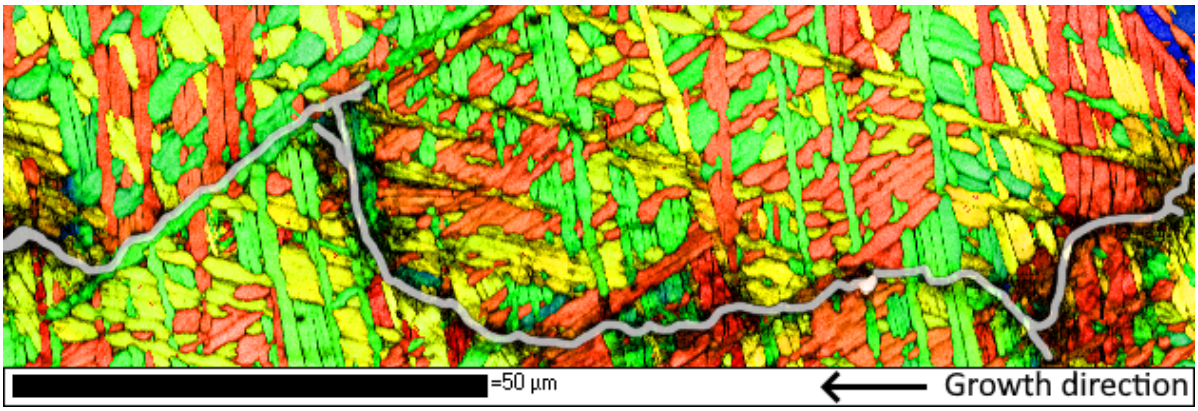

Figure 4.17: Schmid factors of the basal slip system, for the crack in the sample tested at R=0.1 at area a, indicated for all individual grains with the colours representing the magnitude of the Schmid factor according to Figure 4.16.

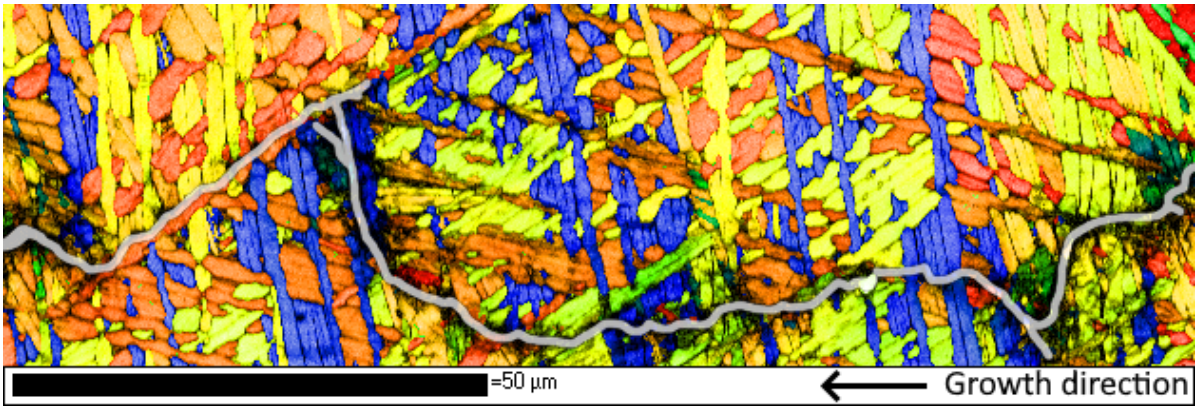

Figure 4.18: Schmid factors of the prismatic slip system, for the crack in the sample tested at R=0.1 at area a, indicated for all individual grains with the colours representing the magnitude of the Schmid factor according to Figure 4.16.

By comparing Figure 4.17 and Figure 4.18 the optimal slip system for the crack propagation is determined. The optimal slip system is determined by examining the crack path in the system where the Schmid factor is highest. When the crack then propagates into a region where the other slip system provides an easier crack path in the form of a higher Schmid factor, the crack is assumed to change slip system. This method allows for identification of the locations and frequencies of expected changes in slip system. This method is applied to Figure 4.17 and Figure 4.18 in order to create an EBSD image of the crack path through the optimal slip system available, shown in Figure 4.19.

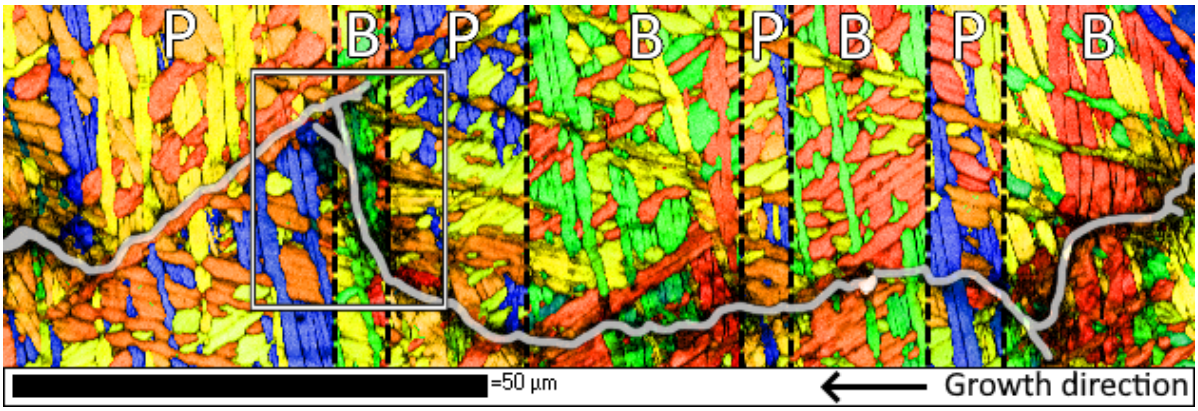

Figure 4.19: Combined Schmid factor image of the basal and prismatic slip systems for the crack in the sample tested at R=0.1 at area a where the areas where basal slip is expected are indicated with B and the areas where prismatic slip is expected are indicated with P.

From Figure 4.19 is becomes clear that the movement of the crack through the material is influenced by the low Schmid factor areas encountered. The crack moves straight through areas indicated with red or orange colors, where the Schmid factor is high. At the areas where green or blue grains are encountered, a significant deflection of the crack can be observed, indicated by the square in Figure 4.19, this deflection is attributed to the low Schmid factors of these green and blue areas. Furthermore, the slip system changes on average every 16 µm, this is a result of the high concentration of low Schmid factor areas present in both the basal and the prismatic slip systems. These low Schmid factor areas cause a change in slip system when this leads to a higher Schmid factor.

Another part of the crack in the sample tested at R=0.1 which was further examined is area b as indicated in Figure 4.14. This area has been tested at a near-threshold ΔK of 11 MPa$\sqrt{\text{m}}$. When the combined Schmid factor image of this area is inspected, similar results are found in area b (Figure 4.20) when compared to area a (Figure 4.19). The black areas visible indicate unidentified points in the EBSD analysis.

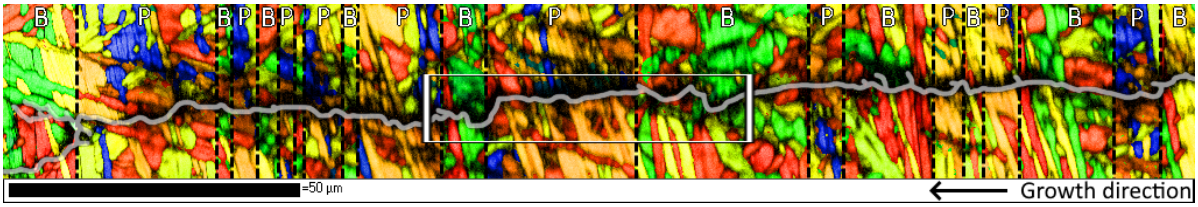

Figure 4.20: Combined Schmid factor image of the basal and prismatic slip systems for the crack in the sample tested at R=0.1 at area b where the areas where basal slip is expected are indicated with B and the areas where prismatic slip is expected are indicated with P.

The movement of the crack shown in Figure 4.20 shows tortuosity around low Schmid factor areas indicated with green and blue colours, as highlighted by the square. The deflections found in Figure 4.20 are not as drastic as those found in Figure 4.19 as a path through high Schmid factors was always available without a large deflection. The amount of changes in slip system indicated is higher in Figure 4.20 than that of Figure 4.19 at a rate of one transition at on average every 10 µm. This is on one hand attributed to an even higher concentration of low Schmid areas. On the other hand, this might be an overestimation as the crack is able to propagate through a low Schmid factor region without changing slip system. This is due to a crack being able to propagate through an unlikely grain if this accommodates an easy fracture path [41]. This effect might cause the current method used to predict a change in slip system to overestimate the amount of changes.

The same method to predict the active slip system was also applied to the areas indicated in the crack tested an R-ratio of 0.7 shown in Figure 4.15. Firstly, the slip systems of area a are shown in Figure 4.21 which was tested at a relatively high ΔK of 13 MPa$\sqrt{\text{m}}$.

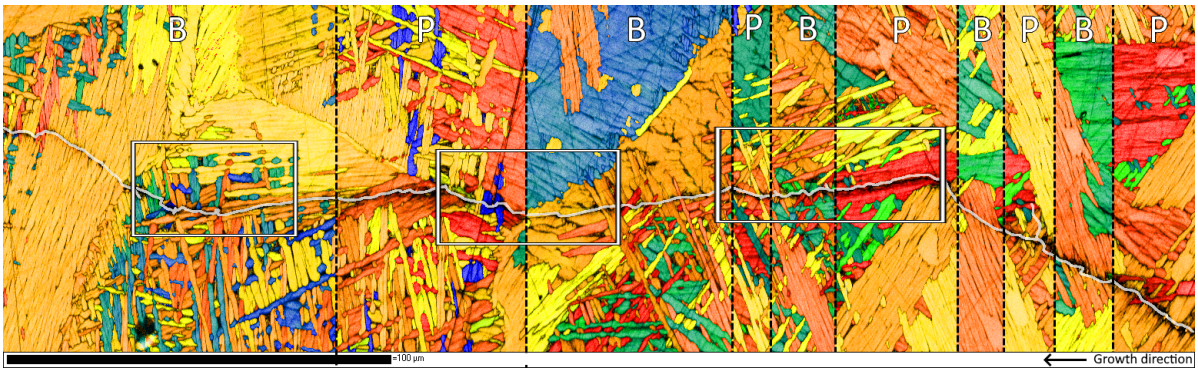

Figure 4.21: Combined Schmid factor image of the basal and prismatic slip systems for the crack in the sample tested at R=0.7 at area a where the areas where basal slip is expected are indicated with B and the areas where prismatic slip is expected are indicated with P.

Figure 4.21 shows a clear image of area a of Figure 4.15 where the movement of the crack is again clearly influenced by the Schmid factor. This influence is most apparent when the movement through the high Schmid areas is mostly straight but whenever a low Schmid area is encountered, small deflections appear in order to avoid the low Schmid area, visible in the three areas highlighted with squares in Figure 4.21. The amount of changes in slip system present is a lower at about one change every 33 µm. This low amount of changes in slip system is attributed to the large α colonies present in this part of the material. The α colonies have a largely homogeneous Schmid factor throughout the colony and therefore no change in slip system is expected.

The final area examined for the active slip system is area b of the sample tested at R=0.7 shown in Figure 4.15, this area is tested at a near-threshold ΔK of 9 MPa$\sqrt{\text{m}}$ (Figure 4.22).

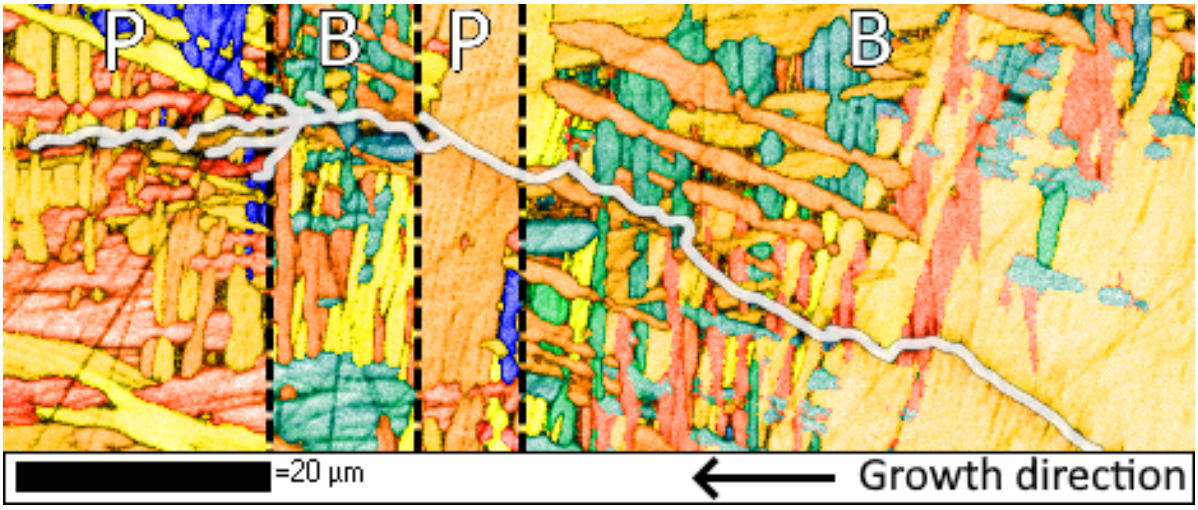

Figure 4.22: Combined Schmid factor image of the basal and prismatic slip systems for the crack in the sample tested at R=0.7 at area b where the areas where basal slip is expected are indicated with B and the areas where prismatic slip is expected are indicated with P.

Figure 4.22 shows well how a high Schmid area indicated by red or orange allows for a straight crack path, in contrast to the areas where more low Schmid areas are present and a more irregular crack path is followed. A low amount of changes in slip system, at a transition on average every 25 µm, is still observed in Figure 4.22 as this is a direct continuation of the area shown in Figure 4.21. Fewer changes in slip system are expected due the large homogeneous α colonies.

4.3.2. Misorientation angles along crack path

Besides the effects of the Schmid factor on the crack path, there are other microstructural features which can influence the crack path. At areas where no direct advantage in the lowest energy crack path can be obtained from the Schmid factor, the grain boundaries play an important role in facilitating crack propagation [6]. The microstructural features discussed in the current section besides the Schmid factor are therefore misorientation angles of the different grain boundaries. The grain boundaries between α lamellae within α colonies typically have misorientation angles of $< 5°$ whereas the misorientation angle between these α colonies is typically $> 15°$. The medium to high angle grain boundaries ($> 5°$) are highlighted in Figure 4.23 with the legend of the colours of the angles of the grain boundaries shown. The cracks shown in subsection 4.3.2 are the same as those shown in subsection 4.3.1.

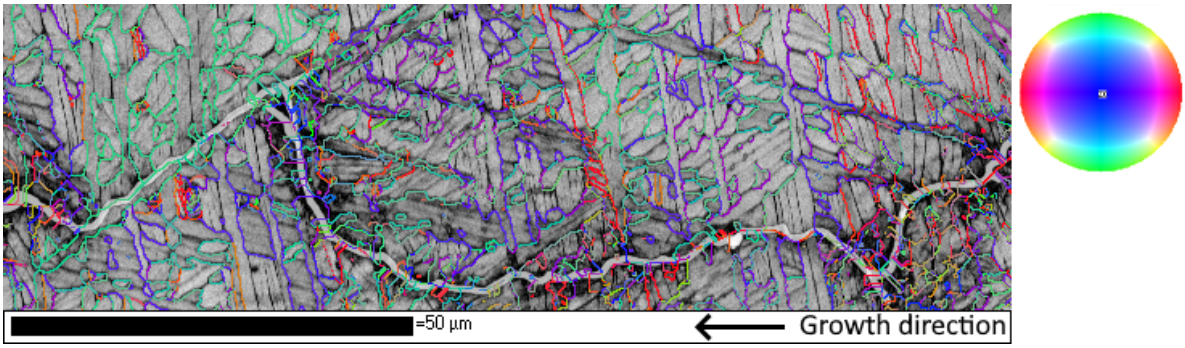

Figure 4.23: Misorientation angles between grains where the angles $> 5°$ are highlighted.

Figure 4.23 is an overlay of the HAGB found by the Jeol SEM projected onto the band contrast image. This allows for the HAGB to be clearly identified while the LAGB in the form of the boundaries between the α lamellae are also visible. One issue with the identification of the HAGB is that the crack itself is also considered a HAGB at times. This issue is solved by overlaying the IPF map onto Figure 4.23 as seen in Figure 4.24.

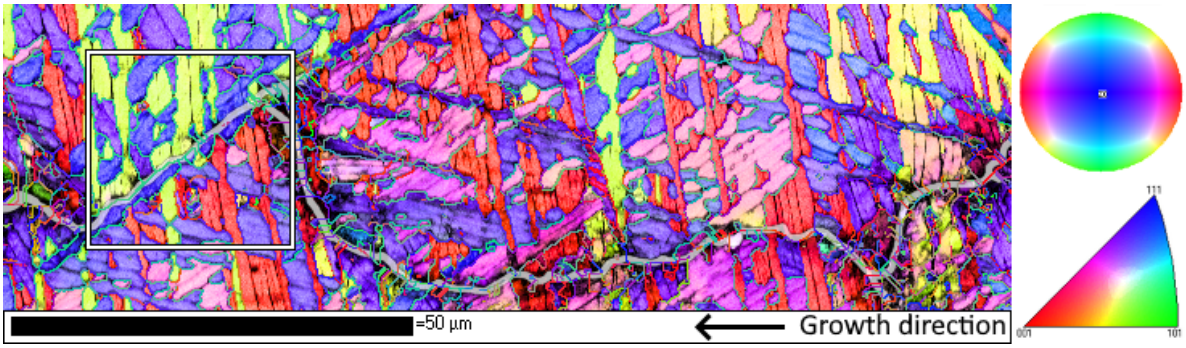

Figure 4.24: Map of the HAGB and band contrast results from the Jeol EBSD results overlayed onto the IPF data for a visual check on the results presented of area *a* in the sample tested at R=0.1.

Figure 4.24 shows how the crack tested at an R-ratio of 0.1 and a high ΔK of 24 MPa$\sqrt{\text{m}}$ tends to move along the LAGB of the α lamellae when the boundaries of the lamellae are in a similar direction as the crack. When the crack encounters these LAGB at a higher incident angle, the crack seems to propagate through without any visible deflection. When a HAGB is encountered, the crack tends to move along the boundary and intergranular cracking is preferred, a clear example is highlighted by the square in Figure 4.24. The effect of HAGB on crack deflection is not significant and deflection is only detected at a low incident angle of the crack on these boundaries. The effect of HAGB on deflections seems therefore significantly lower than the effect of the Schmid factor.

When area *b* of the sample tested at R=0.1 crack, tested at a near-threshold ΔK of 11 MPa$\sqrt{\text{m}}$, is considered, some different mechanics seem to play a role. The band contrast, HAGB and IPF are again combined into one figure which results in Figure 4.25.

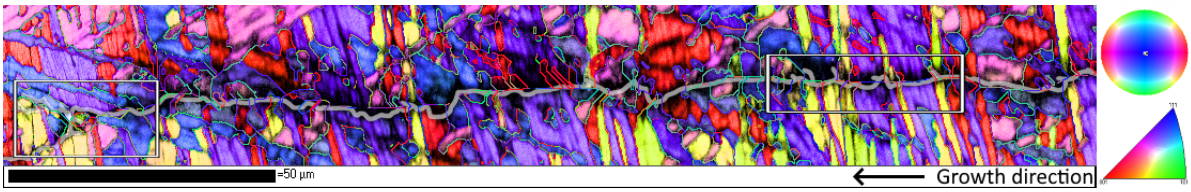

Figure 4.25: Map of the HAGB and band contrast results from the Jeol EBSD results overlayed onto the IPF data for a visual check on the results presented of area *b* in the sample tested at R=0.1.

At close inspection of Figure 4.25, more crack bifurcation is visible when compared to Figure 4.24. This happens at the areas where HAGB are present, highlighted by the squares in Figure 4.25, indicating that in Ti-6Al-4V there might be a correlation between HAGB and bifurcation. Furthermore, the material seems not affected by the LAGB found between the α lamellae as the lamellae are not orientated favourable with the crack growth direction.

Area *a* from the sample tested at R=0.7, shown in Figure 4.26, which was tested at a high ΔK of 13 MPa$\sqrt{\text{m}}$, shows a clear picture of the effects of the LAGB on the crack path.

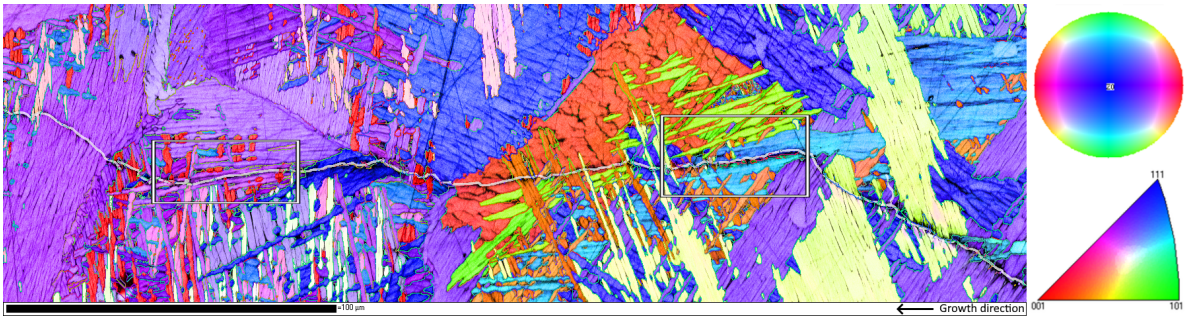

Figure 4.26: Map of the HAGB and band contrast results from the Jeol EBSD results overlayed onto the IPF data for a visual check on the results presented of area *a* in the sample tested at R=0.7.

The crack propagation through the large α colonies visible in Figure 4.26 shows good correlation between the orientation of the α lamellae and the crack growth direction, as highlighted by the squares. When the angle of incidence is low enough, the LAGB of the α lamellae are able to facilitate intergranular crack propagation. The effect of the HAGB in Figure 4.26 is not clearly identified as no bifurcation or large deflections are found.

Finally, area b from the sample tested at R=0.7, tested at a near-threshold ΔK of 9 MPa$\sqrt{\text{m}}$, shows the crack tip with some different mechanics when compared to a higher ΔK area. This crack tip is shown in Figure 4.27.

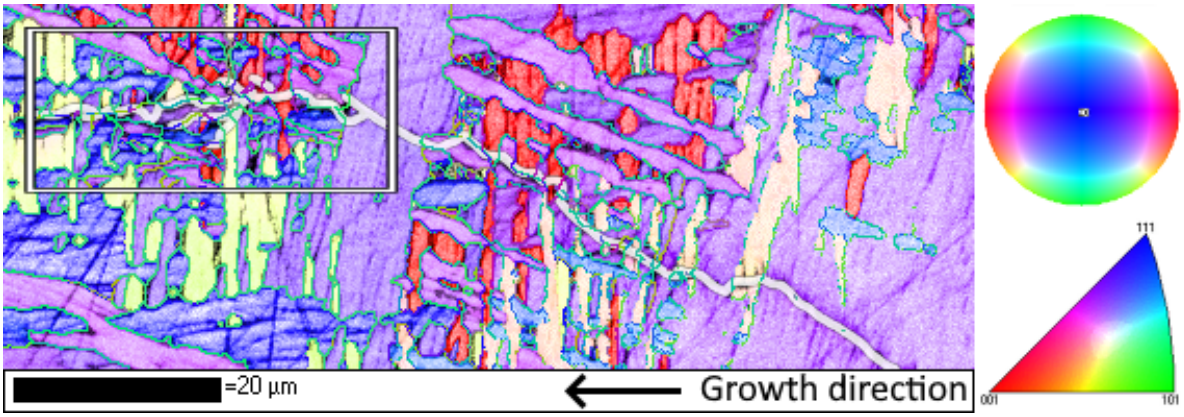

Figure 4.27: Map of the HAGB and band contrast results from the Jeol EBSD results overlayed onto the IPF data for a visual check on the results presented of area b in the sample tested at R=0.7.

The crack shown in Figure 4.27 contains more bifurcation than the areas previously discussed, as indicated by the square. The bifurcation is mostly present at HAGB with the added notion that there are multiple transgranular crack paths possible at a low incident angle with the growth direction. There is therefore an indication that a combination of these factors is more likely able to facilitate crack bifurcation.

4.4. Effect of microstructural features on crack path probability

As discussed in section 4.3, the Schmid factors and the misorientation angles along the crack path can greatly influence the crack path. The effect of these properties was divided into deflection and bifurcation. It has become clear that different microstructural features affect the crack path differently for different load cases. In this section, the effects of the Schmid factors and the misorientation angles at different load cases on the crack path are discussed, after which the probability of a crack path deviation in the form of either deflection or bifurcation is related to the microstructural features present and the load case applied. This will result in an overview of the influence of the microstructural features on fatigue crack propagation in Ti-6Al-4V.

4.4.1. Effect of Schmid factor on crack path

The figures in subsection 4.3.1 show the changes in active slip system along the crack path and the effects of a low Schmid factor on crack deflection. This section will relate the effects of the Schmid factor to the load case applied by comparing what range of Schmid factors causes deflections. An overview of four different load cases is presented in Figure 4.28, showing the crack paths in comparable microstructures at similar Schmid factors.

From Figure 4.28 similar deflection patterns are visible across all load cases presented. The cracks seem to prefer propagation along the red regions ($m_s = 0.45 - 0.50$), where orange regions ($m_s = 0.35 - 0.45$) provide a crack path where no deflection is observed. Starting at the yellow regions ($m_s = 0.35 - 0.30$), some deflection is observed, especially when a high Schmid factor region is nearby. The green ($m_s = 0.30 - 0.15$) and the blue ($m_s = 0.15 - 0$) regions show a large influence on deflection where large deviations from the expected crack path are observed. Some propagation through the green and blue areas is observed but only when this facilitates an easy crack path by linking two grains where slip is more likely [41].

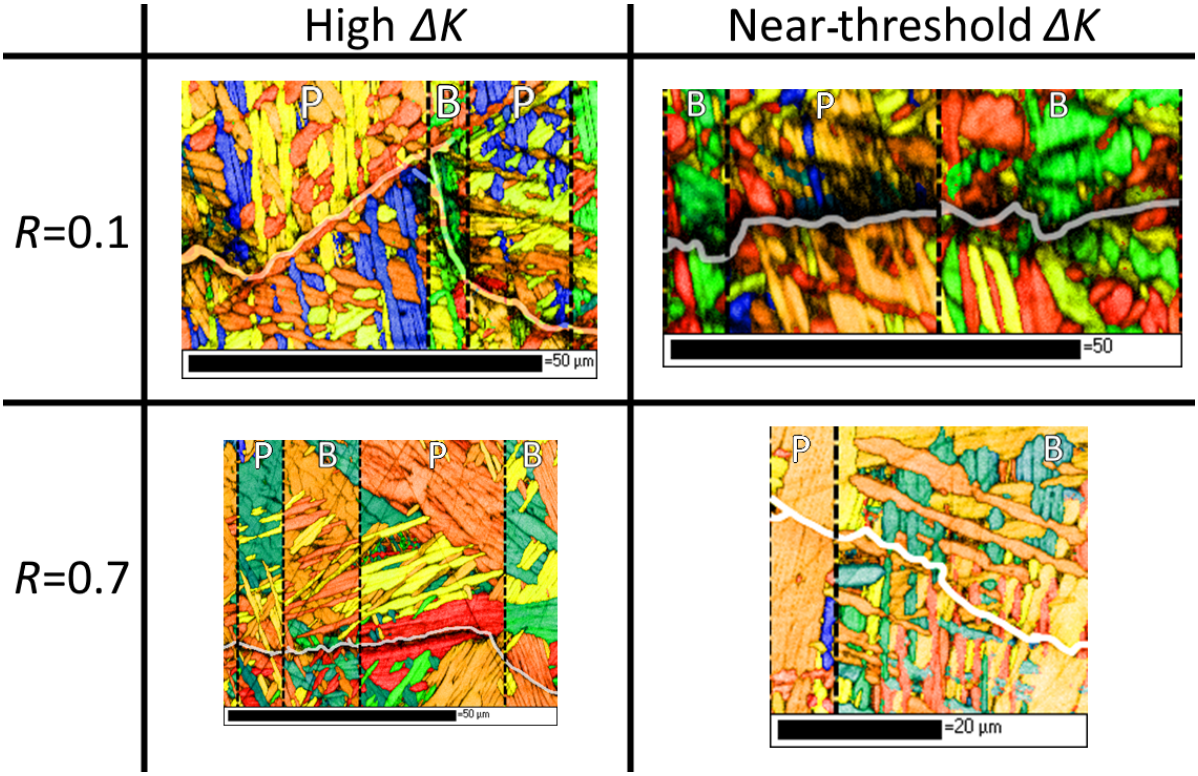

Figure 4.28: Selected sections of the combined Schmid factor figs. 4.19 to 4.22, showing the influence of Schmid factors on the crack path at different load cases where high ΔK values are 24 MPa$\sqrt{m}$ and 15 MPa$\sqrt{m}$ for the tested R-ratios of 0.1 and 0.7 respectively.

The crack is not only deflected when a low Schmid factor area is encountered. When a crack is forced to propagate through a low Schmid factor area, different behaviour is observed. When a crack propagates through a colony with a high Schmid factor, the crack follows a straight path. When the crack propagates through a low Schmid factor area, the crack struggles to find an easy path and shows erratic movement. This is visible in a section of the analysed crack of the sample tested at R=0.1 shown in Figure 4.29.

The crack path through the low Schmid area ($m_s = 0.04$) shown on the right side of Figure 4.29a, shows small deflections despite encountering no HAGB or favourably orientated LAGB as shown in Figure 4.29b. When the crack enters the high Schmid factor area on the left side of Figure 4.29a, the crack path is only deflected when other low Schmid regions are encountered, indicated by green regions. The difference in crack path is therefore attributed to the difference in Schmid factor through which the crack propagates.

There is no observable difference in the influence of the Schmid factor on the crack path at the different load cases. The crack seems to be affected in a similar way by the Schmid factor, from a high ΔK all the way to the near-threshold ΔK. There is seemingly also no effect of different R-ratios on the influence the Schmid factors has on crack deflection, which is in accordance with literature [8]. Therefore, a decrease of the Schmid factor seemingly always leads to a decrease the crack propagation rate independent of the load case applied. A low Schmid factor microstructure for the available slip systems is therefore desired when a material is designed for low fatigue crack growth rates.

4.4.2. Effects of misorientation angles on crack path

The results of the influence of the misorientation angles on the crack path have been discussed in subsection 4.3.2. These results have shown a distinct influence of HAGB on crack bifurcation for different load cases. The different load cases shown in subsection 4.3.2 have been summarized in Figure 4.30.

Figure 4.30 shows two sections of two different cracks for a total of four sections, these particular sections were chosen for this comparison due to their similar amount of $60°$ grain boundaries along

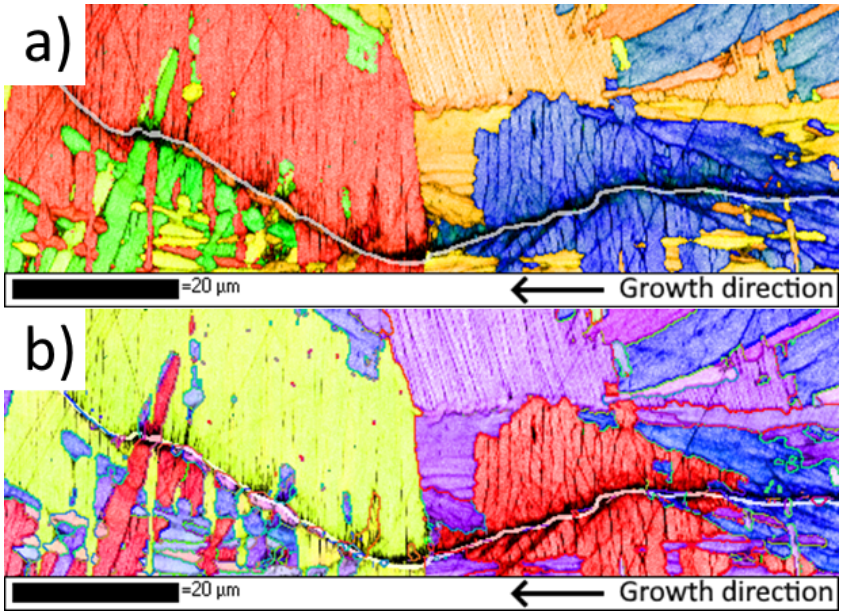

Figure 4.29: Crack path in a basal slip system (a) and through the HAGB + IPF (b) tested at an R-ratio of 0.1 at a near-threshold ΔK.

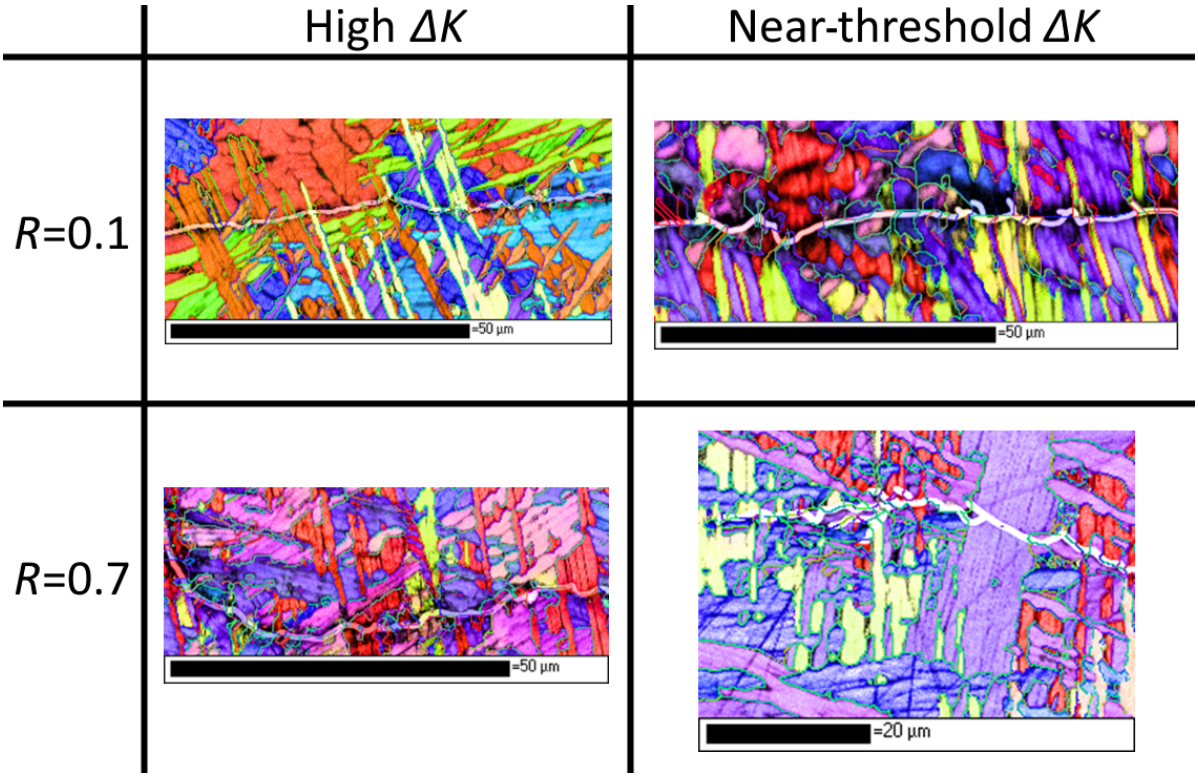

Figure 4.30: Selected sections of the combined HAGB + IPF figs. 4.24 to 4.27, showing the influence of the HAGB on the crack path at different load cases where high ΔK values are $24\,\mathrm{MPa}\sqrt{\mathrm{m}}$ and $15\,\mathrm{MPa}\sqrt{\mathrm{m}}$ for the tested R-ratios of 0.1 and 0.7 respectively.

the crack path. These HAGB were found to correlate closely to observed bifurcation, which is due to the HAGB promoting the transition from transgranular crack growth to intergranular crack growth [52]. Therefore, once a HAGB is encountered there are multiple crack paths available and bifurcation is more likely.

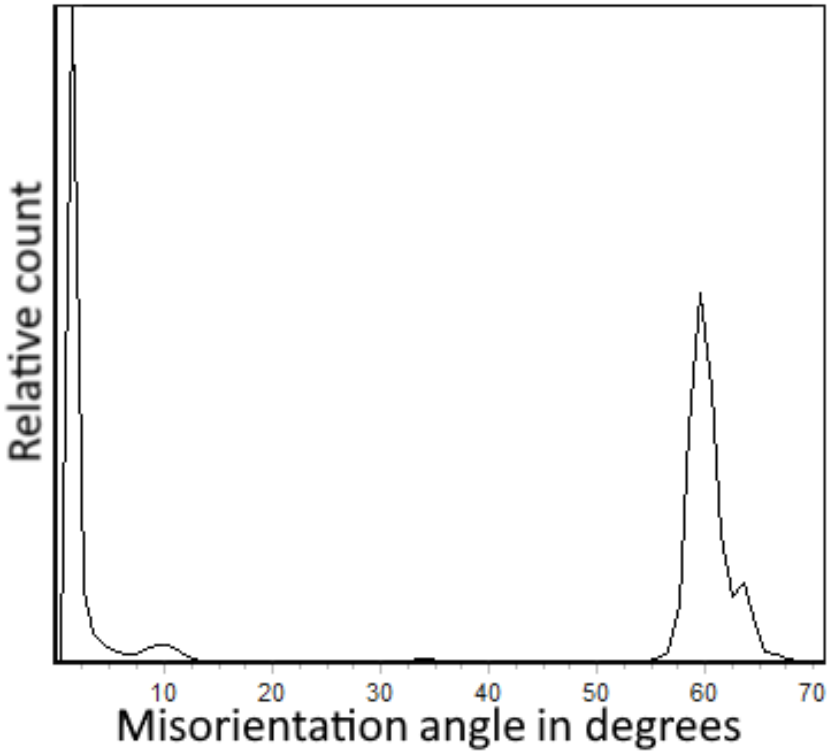

Figure 4.31: A histogram of the relative count of grain boundaries of different orientations found in the current research.

Figure 4.31 shows the relative count of different grain boundary angles found in the fatigue tested β annealed Ti-6Al-4V of the current research. Apart from the high concentration of LAGB between the α lamellae, a clear spike in HAGB is found at $60°$. The high concentration of $60°$ grain boundaries in Ti-6Al-4V was also found by Hu et al., where the high concentration is attributed to deformation twinning [55]. During SEM analysis of the cracks in the current research, no deformation twins were found however as the tested samples have not been etched after testing.

An increase of the effects of HAGB on bifurcation is observed in Figure 4.30 when ΔK is decreased towards the near-threshold ΔK. This indicates that when ΔK is lowered during testing, the crack propagation rate does not only decrease due to a decrease in the stress intensity range applied but the bifurcation in itself causes a decrease in the effective ΔK and therefore the crack propagation rate [56]. When a material is designed for near-threshold ΔK applications, an increase in HAGB is therefore desired for better fatigue crack growth resistance. This is in accordance with Kumar et al. where an increase in bifurcation was found in near-threshold crack propagation in Ti-6Al-4V [52].

The effect of LAGB between the α lamellae on the crack path is seemingly not affected by the load case. The effect is also limited to small deflections in the crack path and does not seem to cause bifurcation. Bifurcation is mainly found when a transition from transgranular to intergranular cracking is observed. Since the LAGB are found within the α colonies, they do not attribute to this transition.

4.4.3. Probability of change in crack path due to microstructural features

The Schmid factor and the misorientation angles present in the microstructure have distinct effects on the crack path followed. The effects on the crack path due to the microstructural features are divided into deflection and bifurcation. Due to there being no certainty of crack deflection or bifurcation when a certain microstructural threshold is reached, two probability functions are proposed. These probability

functions would describe the probability of a crack deflecting and the probability of crack bifurcation as a function of microstructural features and load cases applied.

The probability function for crack deflection at a certain point in the propagation stage can be described as a function of microstructural features and load cases applied. The first microstructural feature which shows a clear influence on crack deflection is the Schmid factor, as has been described in subsection 4.4.1. Due to the Schmid factor being a scalar, the relation between the Schmid factor and the probability of deflection is considered linear. This linear relation is further supported by the results for the Schmid factor of slip systems obtained by Zeng et al. and Ma et al. [57, 8].

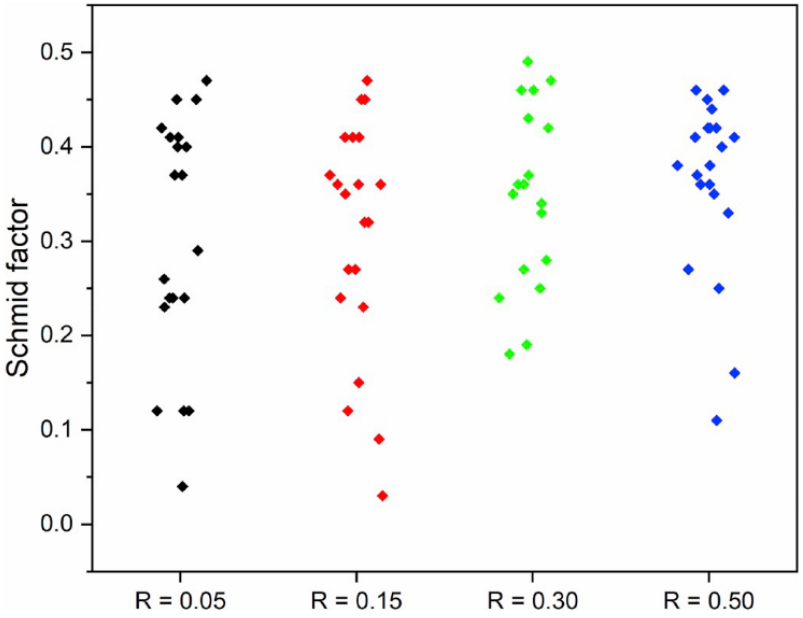

Figure 4.32: Schmid factors of grains which have been propagated through during fatigue crack growth at different R-ratios in a 5083 aluminum alloy [8].

Figure 4.32 shows the amount of grains of certain Schmid factors which have been propagated through during the fatigue crack growth in a 5083 aluminum alloy [8]. This indicates a relation where an increase in Schmid factors allows for a higher probability of propagation. Since the probability of a crack propagating transgranularly is the inverse of the probability of crack deflection, a linear decrease in deflections is assumed for a linear increase in Schmid factor. Unfortunately the graph shown in Figure 4.32 could not be constructed using the data for Ti-6Al-4V received from the crack propagation tests in the current research. This is a result of the limitations in the amount and quality of the EBSD data.

The probability of crack deflection due to grain boundary misorientation is divided into two factors. First there is the incident angle of the crack with the grain boundary, this angle leads to a deflection angle of the crack. Then there is the misorientation angle of grain boundary which describes the difference in crystallographic orientation between two grains. Kobayashi et al. [7] found a decrease in the amount of cracks deflected when the deflection angle is increased. However, an increase in the amount of cracks deflected was found for an increase in the misorientation angle for austenitic stainless steel, which is shown in Figure 4.33 [7]. The only deflections observed at LAGB are at low deflection angles while the amount of deflections clearly increases with the misorientation angle. This is in accordance with the findings of the current research as deflections have been observed for LAGB at low deflection angles while HAGB have shown deflections even at higher deflection angles. A diagram such as Figure 4.33 could not be constructed for Ti-6Al-4V using the data from the current research due to the high distortion of the EBSD data along the crack path.

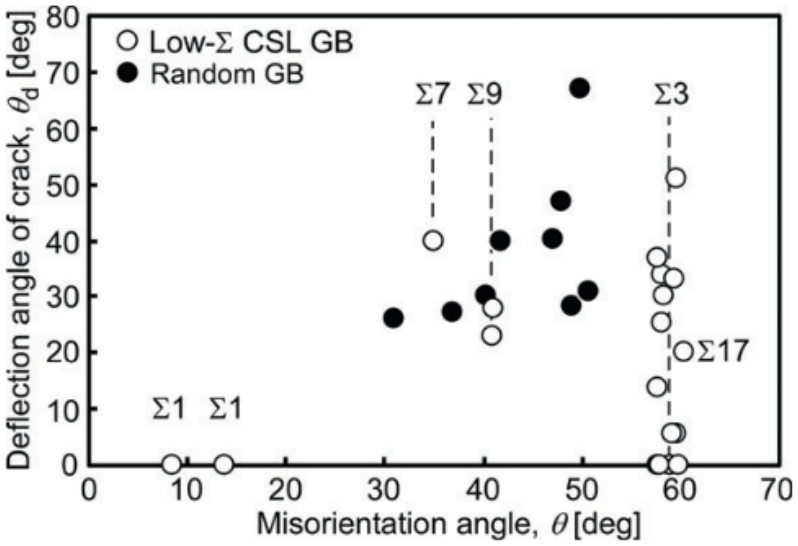

Figure 4.33: Amount of deflections found during fatigue crack growth as a function of deflection angle and misorientation angle in austenitic stainless steel [7].

There is no indication that the load case applied, in the form of ΔK and R-ratio, seems to influence the probability of crack deflection. Figure 4.28 shows four microstructurally similar cracks with only the load case varied. The behaviour of the deflection is comparable among all four cracks, indicating no influence of the load case. This indication disagrees with Kumar et al., where a decrease of ΔK is linked to an increase in tortuosity [52]. Figure 4.32 shows a slight difference in the Schmid factors which have been propagated through for different R-ratios but the qualitative analysis of the data of the current research suggests that this is the result of a probabilistic spread.

The probability of deflection is therefore proposed in the current study to be a function of the Schmid factor m_s, the deflection angle ϕ and the misorientation angle ψ. The resulting probability function is:

$$P(deflection) = f(m_s{}^{-1}, cos(\phi), \psi) \tag{4.4}$$

The probability of deflection shows an inverse relationship with the Schmid factor since an increase in Schmid factor decreases the probability of crack deflection. The deflection angle has a relation to the probability in the form of $cos(\phi)$, this is due to the probability of deflection being significantly higher at low angles and moving to zero at $90°$. The misorientation angle simply has a positive relationship to the probability of crack deflection as an increase in grain boundary angle leads to an increase in crack deflections.

When the probability for bifurcation is considered, Yoder et al. found a relation between bifurcation and the orientation of the α lamellae in the material [58]. This relation is also visible in Figure 4.30, where bifurcation seems to be in accordance with the direction of the α lamellae boundaries. The main influence on crack bifurcation as observed in the current research seems to be the presence of HAGB. These are consistently found to intersect the crack path at locations where crack bifurcation was observed. This effect is also found in literature where the amount of HAGB are found to be directly linked to the amount of crack bifurcation [57].

A correlation between Schmid factor and crack bifurcation is not clear from the current results. Despite some indications of a low Schmid factor aiding in crack bifurcations being shown in Figure 4.22, these bifurcations are mostly linked to the HAGB present. The effect of Schmid factor is therefore limited to deflections, this is also found by Ma et al. [8].

The probability function of bifurcation is proposed to be more complicated than that of deflection. This is due to the effect which ΔK has on bifurcation, as is shown in Figure 4.30. The indication here is that a decrease of ΔK towards ΔK_{th} leads to an increase in bifurcation. The statement made by Kumar et al., shown above, that a decrease in ΔK leads to an increase in tortuosity, seems to apply to bifurcation [52]. This is due to the fact that the tortuosity observed was linked to the transition from transgranular to intergranular cracking, which is the same transition from which bifurcation originates.

Choi et al. have also observed a clear relation between a decrease in ΔK and crack bifurcation on a microscopic level [59]. The probability of bifurcation is therefore linked to the ratio of ΔK to ΔK_{th} where bifurcation increases as ΔK approaches ΔK_{th}. There was no link found between bifurcation and R-ratio in the current research and in literature.

The probability function of bifurcation is proposed in the current study to be a function of ΔK applied, the deflection angle ϕ and the misorientation angle ψ. The influence of ΔK applied is implemented as a ratio of ΔK_{th} over ΔK as the amount of bifurcation increases as ΔK approaches ΔK_{th}. The effect of the deflection angle ϕ on the probability of bifurcation, similar to the effect on the probability of deflection, is proposed in the form of $cos(\phi)$. Finally, the misorientation angle ψ is directly proportional to the probability of bifurcation, much like the probability of deflection. The difference is that the misorientation angle plays a larger role in bifurcation when compared to deflection, where the Schmid factor is most influential. These relations lead to the following function for the probability of bifurcation.

$$P(bifurcation) = f(\frac{\Delta K_{th}}{\Delta K}, cos(\phi), \psi) \tag{4.5}$$

The influence of the microstructural features in Ti-6Al-4V on proposed probability functions of deflection and bifurcation seem to be in accordance to the literature discussed in section 2.5. The results acquired from the fatigue tests and all EBSD maps shown in Appendix C have been used as a qualitative confirmation of the results presented subsection 4.4.3. A quantitative analysis was unfortunately not possible due to the limitations of the amount of scans and the quality of the EBSD data.

The grain boundaries were related to both bifurcation and deflections while the Schmid factor has been seen to be the main influence on deflections observed. The stress intensity range applied has an influence on the amount of bifurcation observed. The change in crack propagation rate due to the different R-ratios applied could not be linked to any microstructural features in the current research. The only effect of R-ratio found was the previously described effect of roughness-induced crack closure, which on its own cannot account for the change in crack propagation rate found [37].

The results presented can be used to improve the predictability of the fatigue crack growth in Ti-6Al-4V. There are limitations to this however. The main challenge is to map the microstructural features of the material in a non-destructive manner, in 3D-space and at a large scale. When these microstructural features can be mapped in such a way however, the material can be machined in such an orientation that the probability of deflections and bifurcation is maximized, therefore decreasing the fatigue crack propagation rate. If the mapping of the microstructural features is not possible, a material with desirable microstructural features such as low Schmid factors for the designed load direction and high angle misorientation angles can be designed through heat treatments and processing. This can be achieved by, for example, controlling the direction of grain growth during heat treatment or by introducing 60° twinning by means of deformation.

5

Conclusions and Recommendations

5.1. Conclusions

Which microstructural features influence the fatigue crack propagation properties in Ti-6Al-4V ?

- There are two main microstructural features found to have a large influence on the fatigue crack propagation in Ti-6Al-4V. The first of these is the Schmid factor, which relates the stress applied to the slip system available. Due to the small amount of slip systems available in Ti-6Al-4V, a crack path through high Schmid areas is not always found and large deflections in the crack path can be the result. The second microstructural feature found to have a large influence on fatigue crack propagation in Ti-6Al-4V is the misorientation angle of the grain boundaries. When the misorientation angle is large enough, a shift from transgranular cracking to intergranular cracking is observed. Intergranular cracking can cause deviations of the crack path around the grains and the formation of secondary cracks.

- The load case applied during fatigue testing can also influence the fatigue crack propagation properties of Ti-6Al-4V. The R-ratio applied determines the amount of crack closure observed. A high R-ratio tends to keep the crack open during testing where at a lower R-ratio the crack closes in on itself. The effect of crack closure in Ti-6Al-4V is mainly attributed to roughness-induced crack closure which is further aggravated when the grain size of the material is increased. Finally ΔK applied can influence the fatigue crack propagation properties of Ti-6Al-4V by increasing the tortuousness of the crack when ΔK applied approaches ΔK_{th}.

Which experimental methods can be used to determine the influence of the microstructural features on the fatigue crack propagation in Ti-6Al-4V ?

- A load shedding method can be used to construct the Paris' diagrams of the material tested. The Paris' diagram can then be used to quantify the effect of crack closure when different R-ratios are tested. ΔK_{th} can also be determined using the load shedding method, which allows for comparison between high ΔK and near-threshold ΔK crack propagation. Finally, regions of slow crack propagation can easily be identified and further analysed for microstructural features which may have influenced the crack propagation rate.

- EBSD techniques can be combined with SEM imaging to closely relate the microstructural features to the crack path. The EBSD results show the crystallographic orientations of the grains analysed but do not show the crack path in detail. The SEM imagery, on the other hand, shows a detailed crack path but no information on the crystallographic orientations of the grains. By overlaying the results of EBSD and SEM data more details can be observed and analysed.

How do the microstructural features affect the probable crack path during fatigue crack propagation in Ti-6Al-4V ?

- By quantitative analysis it was found that the Schmid factor has a direct relation to the amount and severity of deflections observed in the crack path. When a crack, which is propagating, would encounter a Schmid factor below 0.35, deflections away from the low Schmid area are first observed. When lower Schmid factors are encountered, more deflections are observed and transgranular propagation becomes less likely. The crack is able to shift slip systems if this shift results in a high enough Schmid factor to allow for transgranular cracking.

- The misorientation angle of the grain boundaries encountered during the crack propagation stage can induce both deflections and bifurcations in the crack path. A large number of misorientation angles at 60° are found, these are most likely a result of deformation twinning. These HAGB are mostly found between α colonies and prior β grains and coincide with locations where deflections and bifurcations originate. The increase in deflections and bifurcation at HAGB are a result of the shift from transgranular cracking to intergranular cracking.

- At locations where the incidence angle of the propagating crack with an encountered grain boundary is low, deflections are observed even at low misorientation angles between the α lamellae. These deflections at low deflection angles are observed to aid in both deflections and bifurcation of the crack.

What is the influence of the microstructural features in Ti-6Al-4V on the fatigue crack propagation?

- The influence of microstructural features on fatigue crack propagation in Ti-6Al-4V is found to be mostly in the form of deviations in the crack path due to the Schmid factor and misorientation angles encountered. These deviations in crack path extend the fatigue life of the material. ΔK applied during the fatigue life influences the effect of the microstructural features on the crack path whereas the R-ratio does not.

- One type of deviation in the crack path is the deflection. The current study proposes the probability for a crack to deviate at a certain point in the crack propagation stage is to be a function of the Schmid factor, the deflection angle and the misorientation angle. A low Schmid factor will increase the chance of deflections, a low deflection angle is also preferred for deflections. A high misorientation angle increases the chance of a shift from transgranular to intergranular cracking and therefore increases the chance of deflections.

- The other type of deviation in the crack path described is the bifurcation. The current study proposes the probability of a crack bifurcating during fatigue crack propagation to be a function of ΔK, the deflection angle and the misorientation angle. A clear increase in bifurcations is observed when ΔK tends towards ΔK_{th}. A low deflection angle and a high misorientation angle both allow for an easy secondary crack path resulting in an increased chance of bifurcation.

5.2. Recommendations

In order to further extend the knowledge of influence of the microstructural features on fatigue crack propagation in Ti-6Al-4V, some recommendations are made to aid in further research.

- During the design phase of the samples, some issues were encountered when the heat treatment was applied. The samples used in the current had warped due to the internal stresses induced by the EDM process. A stress relief step in the heat treatment is therefore recommended. Furthermore, the method of preventing an oxidation layer from forming on the samples by means of annealing envelopes was not effective enough to eliminate oxidation. The stainless steel envelopes also fused together with some Ti-6Al-4V samples, making these unusable. The use of a protective paint for oxidation prevention is therefore recommended.

- During the testing phase, the crack propagation rates were microscopically observed. This has led to useful micrographs for post-inspection but it also led to inaccurate propagation measurements. The use of electron potential drop to measure the crack length is therefore recommended.

- During the analysis of the microstructural features around the crack using EBSD, an emphasis was laid on fast analysis at large scales. This emphasis has not allowed for a quantitative analysis of the influence of the Schmid factor and misorientation angles on deflections and bifurcation such as shown in Figure 4.32 and Figure 4.33. This was not possible due to the crack itself being poorly identified, it is therefore recommended to lay an emphasis on a high success rate around the cracks during EBSD analysis.
- The results presented in the current research are limited to a 2D analysis of the microstructural features. When a non-destructive characterisation of the microstructural features in Ti-6Al-4V can be made in 3D or if the crystal orientations can be controlled in such a way that they can be described post treatment, the relations between the crack path and the microstructural features can be described in much more detail. This would also allow for much more reliable estimates in fatigue life of a sample.
- During the current research, a relation was found between the high misorientation angles between grains and bifurcation. These angles were found to mostly be around 60°, this explained by the presence of deformation twinning. This deformation twinning, however, has not been found in the material. If the presence of deformation twinning can be confirmed and related to the bifurcation, deformation twinning can be used to design more fatigue propagation resistant materials.

Bibliography

[1] Walter Schütz. "A history of fatigue". In: Engineering Fracture Mechanics 54.2 (1996), pp. 263–300. ISSN: 00137944. DOI: 10.1016/0013-7944(95)00178-6.

[2] Uwe Zerbst et al. "About the fatigue crack propagation threshold of metals as a design criterion - A review". In: Engineering Fracture Mechanics 153.November 2014 (2016), pp. 190–243. ISSN: 00137944. DOI: 10.1016/j.engfracmech.2015.12.002. URL: http://dx.doi.org/10.1016/j.engfracmech.2015.12.002.

[3] ASML. Mechanics & mechatronics - Lithography principles | ASML. URL: https://www.asml.com/en/technology/lithography-principles/mechanics-and-mechatronics.

[4] Matthew J. Donachie. "Introduction to Selection of Titanium Alloys". In: Titanium: A Technical Guide 180.2 (2000), pp. 5–11. DOI: 10.31399/asm.tb.ttg2.t61120005.

[5] Camebridge:Granta. GRANTA Edupack 2020. 2020.

[6] S.-T. Tu and X.-C. Zhang. "Fatigue Crack Initiation Mechanisms". In: Reference Module in Materials Science and Materials Engineering. Elsevier Inc., 2016. ISBN: 9780128035818. DOI: 10.1016/b978-0-12-803581-8.02852-6. URL: https://www.researchgate.net/publication/301263059.

[7] Shigeaki Kobayashi et al. "Grain boundary engineering for control of fatigue crack propagation in austenitic stainless steel". In: Procedia Engineering 10 (2011), pp. 112–117. ISSN: 18777058. DOI: 10.1016/j.proeng.2011.04.021. URL: http://dx.doi.org/10.1016/j.proeng.2011.04.021.

[8] Mingyang Ma et al. "Investigation of fatigue crack propagation behavior of 5083 aluminum alloy under various stress ratios: Role of grain boundary and Schmid factor". In: Materials Science and Engineering A 773.November 2019 (2020), p. 138871. ISSN: 09215093. DOI: 10.1016/j.msea.2019.138871. URL: https://doi.org/10.1016/j.msea.2019.138871.

[9] Jinwen Lu, Peng Ge, and Yongqing Zhao. "Recent development of effect mechanism of alloying elements in titanium alloy design". In: Xiyou Jinshu Cailiao Yu Gongcheng/Rare Metal Materials and Engineering 43.4 (2014), pp. 775–779. ISSN: 1002185X. DOI: 10.1016/s1875-5372(14)60082-5. URL: http://dx.doi.org/10.1016/S1875-5372(14)60082-5.

[10] M. J. Bermingham et al. "MIcrostucture of cast titanium alloys". In: Materials Forum 31.January 2007 (2007), pp. 84–89. ISSN: 08832900.

[11] Y. Fan et al. "Relationships among the Microstructure, Mechanical Properties, and Fatigue Behavior in Thin Ti6Al4V". In: Advances in Materials Science and Engineering 2016 (2016). ISSN: 16878442. DOI: 10.1155/2016/7278267.

[12] Chao Zheng et al. "Effect of microstructures on ballistic impact property of Ti-6Al-4V targets". In: Materials Science and Engineering A 608 (July 2014), pp. 53–62. ISSN: 09215093. DOI: 10.1016/j.msea.2014.04.032.

[13] R. K. Nalla et al. "Influence of Microstructure on High-Cycle Fatigue of Ti-6Al-4V: Bimodal vs. Lamellar Structures". In: Metallurgical and Materials Transactions A: Physical Metallurgy and Materials Science 33.13 (2002), pp. 899–918. ISSN: 10735623. DOI: 10.1007/s11661-002-1023-3.

[14] Daeho Jeong et al. "High cycle fatigue and fatigue crack propagation behaviors of β-annealed Ti-6Al-4V alloy". In: International Journal of Mechanical and Materials Engineering 12.1 (2017). ISSN: 18230334. DOI: 10.1186/s40712-016-0069-8.

[15] S. Suresh and R. O. Ritchie. "Geometric model for fatigue crack closure induced by fracture surface Roughness". In: METALL TRANS A V 13A.N 9 (1982), pp. 1627–1631. ISSN: 03602133. DOI: 10.1007/bf02644803. URL: https://link.springer.com/article/10.1007/BF02644803.

[16] Changsheng Tan, Qiaoyan Sun, and Guojun Zhang. "Role of microstructure in plastic deformation and crack propagation behaviour of an α/β titanium alloy". In: Vacuum 183 (Jan. 2021), p. 109848. ISSN: 0042207X. DOI: 10.1016/j.vacuum.2020.109848.

[17] Qianfan Xin. "Durability and reliability in diesel engine system design". In: Diesel Engine System Design (2013), pp. 113–202. DOI: 10.1533/9780857090836.1.113.

[18] J. Carvill. "Strengths of materials". In: Mechanical Engineer's Data Handbook. Elsevier, Jan. 1993, pp. 1–55. DOI: 10.1016/b978-0-08-051135-1.50006-6.

[19] D H Kohn and P Ducheyne. "Tensile and fatigue strength of hydrogen-treated Ti-6Al-4V alloy". In: Journal of Materials Science 26.2 (1991), pp. 328–334. ISSN: 00222461. DOI: 10.1007/BF00576523. URL: https://www.researchgate.net/publication/237258506.

[20] K. Wang et al. "Prediction of short fatigue crack growth of Ti-6Al-4V". In: Fatigue and Fracture of Engineering Materials and Structures 37.10 (2014), pp. 1075–1086. ISSN: 14602695. DOI: 10.1111/ffe.12177.

[21] Samatham Madhukar et al. "A Study on Improvement of Fatigue Life of materials by Surface Coatings". In: International Journal of Current Engineering and Technology 8.01 (Jan. 2018). DOI: 10.14741/ijcet.v8i01.10878.

[22] C. Schiller and D. Walgraef. "Numerical simulation of persistent slip band formation". In: Acta Metallurgica 36.3 (1988), pp. 563–574. ISSN: 00016160. DOI: 10.1016/0001-6160(88)90089-2.

[23] N. Pugno et al. "A generalized Paris' law for fatigue crack growth". In: Journal of the Mechanics and Physics of Solids 54.7 (July 2006), pp. 1333–1349. ISSN: 00225096. DOI: 10.1016/j.jmps.2006.01.007.

[24] Jean LeMaitre. Handbook of Materials Behavior Models, Three-Volume Set. Academic Press, 2001, p. 1200. ISBN: 9780080533636. URL: https://www.sciencedirect.com/book/9780124433410/handbook-of-materials-behavior-models.

[25] W. Anderson P. Paris M. Gomez et al. A Rational Analytic Theory of Fatigue. 1961.

[26] Robert 0. Ritchie. Influence of microstructure on near-threshold fatigue crack propagation in ultra-high strength steel. Tech. rep. November. Lawrence Berkeley National Laboratory, 1976, pp. 35–43.

[27] J Petit, G. Hénaff, and C. Sarrazin-Baudoux. "6.05 - Environmentally Assisted Fatigue in the Gaseous Atmosphere". In: Comprehensive Structural Integrity. Vol. 6. Pergamon, 2007, pp. 211–280. ISBN: 9780080437491. DOI: 10.1016/B0-08-043749-4/06130-9. URL: https://www.academia.edu/download/31934809/Environmentally_assisted_fatigue_in_the_gaseous_atmosphere-3.pdf.

[28] Sudip Dinda and Daniel Kujawski. "Correlation and prediction of fatigue crack growth for different R-ratios using Kmax and ΔK+ parameters". In: Engineering Fracture Mechanics 71.12 (Aug. 2004), pp. 1779–1790. ISSN: 00137944. DOI: 10.1016/j.engfracmech.2003.06.001.

[29] Elber W. "Fatigue crack closure under cyclic tension". In: Engineering Fracture Mechanics 2.1 (July 1970), pp. 37–44. ISSN: 00137944. DOI: 10.1016/0013-7944(70)90028-7.

[30] Xiaoping Huang and Torgeir Moan. "Improved modeling of the effect of R-ratio on crack growth rate". In: International Journal of Fatigue 29.4 (Apr. 2007), pp. 591–602. ISSN: 01421123. DOI: 10.1016/j.ijfatigue.2006.07.014.

[31] G T Gray, J C Williams, and A W Thompson. "Roughness-Induced Crack Closure: An Explanation for Microstructurally Sensitive Fatigue Crack Growth". In: Metallurgical Transactions A 14.2 (1983), pp. 421–433. ISSN: 03602133. DOI: 10.1007/BF02644220.

[32] K. Tanaka. "4.04 - Fatigue Crack Propagation". In: Comprehensive Structural Integrity. Vol. 4. Elsevier Ltd, Jan. 2007, pp. 95–127. ISBN: 9780080437491. DOI: 10.1016/B0-08-043749-4/04089-1.

[33] R. C. McClung, B. H. Thacker, and S. Roy. "Finite element visualization of fatigue crack closure in plane stress and plane strain". In: International Journal of Fracture 50.1 (1991), pp. 27–49. ISSN: 03769429. DOI: 10.1007/BF00035167.

[34] Reinhard Pippan. "Threshold and effective threshold of fatigue crack propagation in ARMCO iron I: The influence of grain size and cold working". In: Materials Science and Engineering A 138.1 (May 1991), pp. 1–13. ISSN: 09215093. DOI: 10.1016/0921-5093(91)90671-9.

[35] R. Pippan and A. Hohenwarter. "Fatigue crack closure: a review of the physical phenomena". In: Fatigue and Fracture of Engineering Materials and Structures 40.4 (2017), pp. 471–495. ISSN: 14602695. DOI: 10.1111/ffe.12578.

[36] A. K. Vasudeven, K. Sadananda, and N. Louat. A review of crack closure, fatigue crack threshold and related phenomena. Nov. 1994. DOI: 10.1016/0921-5093(94)90351-4.

[37] Yanyao Jiang, Miaolin Feng, and Fei Ding. "A reexamination of plasticity-induced crack closure in fatigue crack propagation". In: International Journal of Plasticity 21.9 (Sept. 2005), pp. 1720–1740. ISSN: 07496419. DOI: 10.1016/j.ijplas.2004.11.005.

[38] S. Dubey, A. B.O. Soboyejo, and W. O. Soboyejo. "Investigation of the effects of stress ratio and crack fatigue closure on the micromechanisms of fatigue crack growth in Ti-6Al-4V". In: Acta Materialia 45.7 (1997), pp. 2777–2787. ISSN: 13596454. DOI: 10.1016/S1359-6454(96)00380-1.

[39] G. Lütjering. "Influence of processing on microstructure and mechanical properties of $(\alpha + \beta)$ titanium alloys". In: Materials Science and Engineering A 243.1-2 (1998), pp. 32–45. ISSN: 09215093. DOI: 10.1016/s0921-5093(97)00778-8.

[40] M. Simonelli, Y. Y. Tse, and C. Tuck. "Effect of the build orientation on the mechanical properties and fracture modes of SLM Ti-6Al-4V". In: Materials Science and Engineering A 616 (2014), pp. 1–11. ISSN: 09215093. DOI: 10.1016/j.msea.2014.07.086. URL: http://dx.doi.org/10.1016/j.msea.2014.07.086.

[41] Ioannis Bantounas, David Dye, and Trevor C. Lindley. "The effect of grain orientation on fracture morphology during high-cycle fatigue of Ti-6Al-4V". In: Acta Materialia 57.12 (2009), pp. 3584–3595. ISSN: 13596454. DOI: 10.1016/j.actamat.2009.04.018. URL: http://dx.doi.org/10.1016/j.actamat.2009.04.018.

[42] Zebang Zheng, Daniel S. Balint, and Fionn P.E. Dunne. "Rate sensitivity in discrete dislocation plasticity in hexagonal close-packed crystals". In: Acta Materialia 107.April (2016), pp. 17–26. ISSN: 13596454. DOI: 10.1016/j.actamat.2016.01.035. URL: http://dx.doi.org/10.1016/j.actamat.2016.01.035.

[43] I. Weiss and S. L. Semiatin. "Thermomechanical processing of alpha titanium alloys". In: TMS Annual Meeting (1998), pp. 147–161.

[44] Hasan Guleryuz and Huseyin Cimenoglu. "Oxidation of Ti-6Al-4V alloy". In: Journal of Alloys and Compounds 472.1-2 (2009), pp. 241–246. ISSN: 09258388. DOI: 10.1016/j.jallcom.2008.04.024.

[45] TITANIUM SERVICES. Titanium Sheet Grade5 (TA6V) - Thickness : 2 mm. URL: https://www.titane-services.eu/epages/230155.sf/en_GB/?ObjectPath=/Shops/230155/Products/tole-titane-G5-2xLxl.

[46] Ruben Wauthle et al. "Effects of build orientation and heat treatment on the microstructure and mechanical properties of selective laser melted Ti6Al4V lattice structures". In: Additive Manufacturing 5 (2015), pp. 77–84. ISSN: 22148604. DOI: 10.1016/j.addma.2014.12.008. URL: http://dx.doi.org/10.1016/j.addma.2014.12.008.

[47] F.C. Campbell. Manufacturing technology for aerospace structural materials. Amsterdam: Elsevier, 2011, p. 152.

[48] Gerhard Welsch, Rodney Boyer, and E.W. Collings. Materials properties handbook: titanium alloys. Ohio: ASM International, 1993, p. 484.

[49] N. S. Reddy et al. "Prediction of flow stress in Ti-6Al-4V alloy with an equiaxed $\alpha + \beta$ microstructure by artificial neural networks". In: Materials Science and Engineering A 492.1-2 (2008), pp. 276–282. ISSN: 09215093. DOI: 10.1016/j.msea.2008.03.030.

[50] ASTM Standard E647. "ASTM Standard Test Method for Measurement of Fatigue Crack Growth Rates". In: ASTM Standard 14.2 (2017), pp. 202–216. ISSN: 16797825.

[51] K. Kanaya and S. Okayama. "Penetration and energy-loss theory of electrons in solid targets". In: Journal of Physics D: Applied Physics 5.1 (1972), pp. 43–58. ISSN: 00223727. DOI: 10.1088/0022-3727/5/1/308.

[52] Punit Kumar and Upadrasta Ramamurty. "Microstructural optimization through heat treatment for enhancing the fracture toughness and fatigue crack growth resistance of selective laser melted Ti6Al4V alloy". In: Acta Materialia 169 (2019), pp. 45–59. ISSN: 13596454. DOI: 10.1016/j.actamat.2019.03.003. URL: https://doi.org/10.1016/j.actamat.2019.03.003.

[53] Birhan Sefer et al. "Evaluation of the Bulk and Alpha-Case Layer Properties in Ti-6Al-4V at Micro- And Nano-Metric Length Scale". In: Proceedings of the 13th World Conference on Titanium May (2016), pp. 1619–1624. DOI: 10.1002/9781119296126.ch271.

[54] G. Nolze and A. Winkelmann. "About the reliability of EBSD measurements: Data enhancement". In: IOP Conference Series: Materials Science and Engineering 891.1 (2020). ISSN: 1757899X. DOI: 10.1088/1757-899X/891/1/012018.

[55] Yan Hu and Valerie Randle. "An electron backscatter diffraction analysis of misorientation distributions in titanium alloys". In: Scripta Materialia 56.12 (2007), pp. 1051–1054. ISSN: 13596462. DOI: 10.1016/j.scriptamat.2007.02.030.

[56] G. R. Yoder, L. A. Cooley, and T. W. Crooker. "Quantitative analysis of microstructural effects on fatigue crack growth in widmanstätten Ti-6A1-4V and Ti-8Al-1Mo-1V". In: Engineering Fracture Mechanics 11.4 (1979), pp. 805–816. ISSN: 00137944. DOI: 10.1016/0013-7944(79)90138-3.

[57] Xiangkang Zeng et al. "Quantitative characterization of short fatigue crack and grain boundary interaction behavior in zirconium". In: International Journal of Fatigue 161.October 2021 (2022), p. 106894. ISSN: 01421123. DOI: 10.1016/j.ijfatigue.2022.106894. URL: https://doi.org/10.1016/j.ijfatigue.2022.106894.

[58] G. R. Yoder, L. A. Cooley, and T. W. Crooker. "OBSERVATIONS ON MICROSTRUCTURALLY SENSITIVE FATIGUE CRACK GROWTH IN A WIDMANSTAETTEN Ti-6Al-4V ALLOY." In: Metall Trans A 8 A.11 (1977), pp. 1737–1743. ISSN: 0360-2133. DOI: 10.1007/bf02646877.

[59] Heesoo Choi et al. "Effect of Microstructure on High Cycle Fatigue and Fatigue Crack Propagation Behaviors of β-Annealed Ti6Al4V Alloy". In: Metals and Materials International 27.7 (2021), pp. 2239–2248. ISSN: 20054149. DOI: 10.1007/s12540-019-00598-4. URL: https://doi.org/10.1007/s12540-019-00598-4.

A

Test set-up dimensions

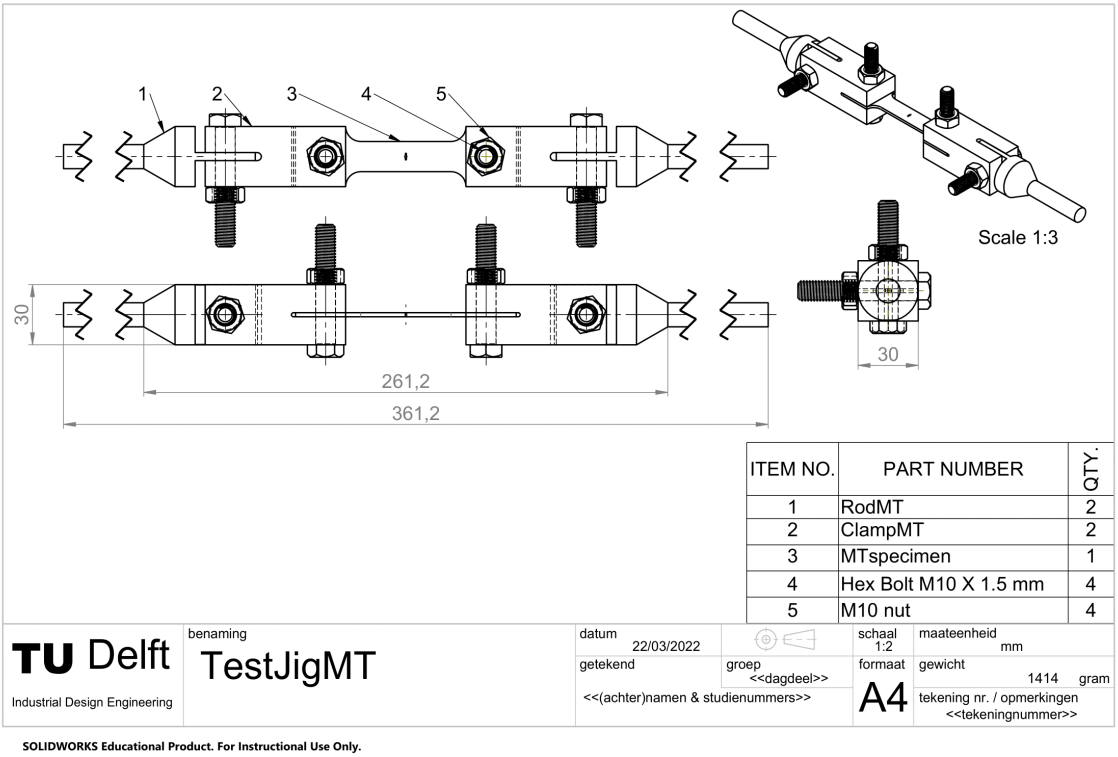

ITEM NO.	PART NUMBER	QTY.
1	RodMT	2
2	ClampMT	2
3	MTspecimen	1
4	Hex Bolt M10 X 1.5 mm	4
5	M10 nut	4

TU Delft Industrial Design Engineering	benaming TestJigMT	datum 22/03/2022	schaal 1:2	maateenheid mm
		getekend <<(achter)namen & studienummers>>	groep <<dagdeel>>	formaat A4
				gewicht 1414 gram
				tekening nr. / opmerkingen <<tekeningnummer>>

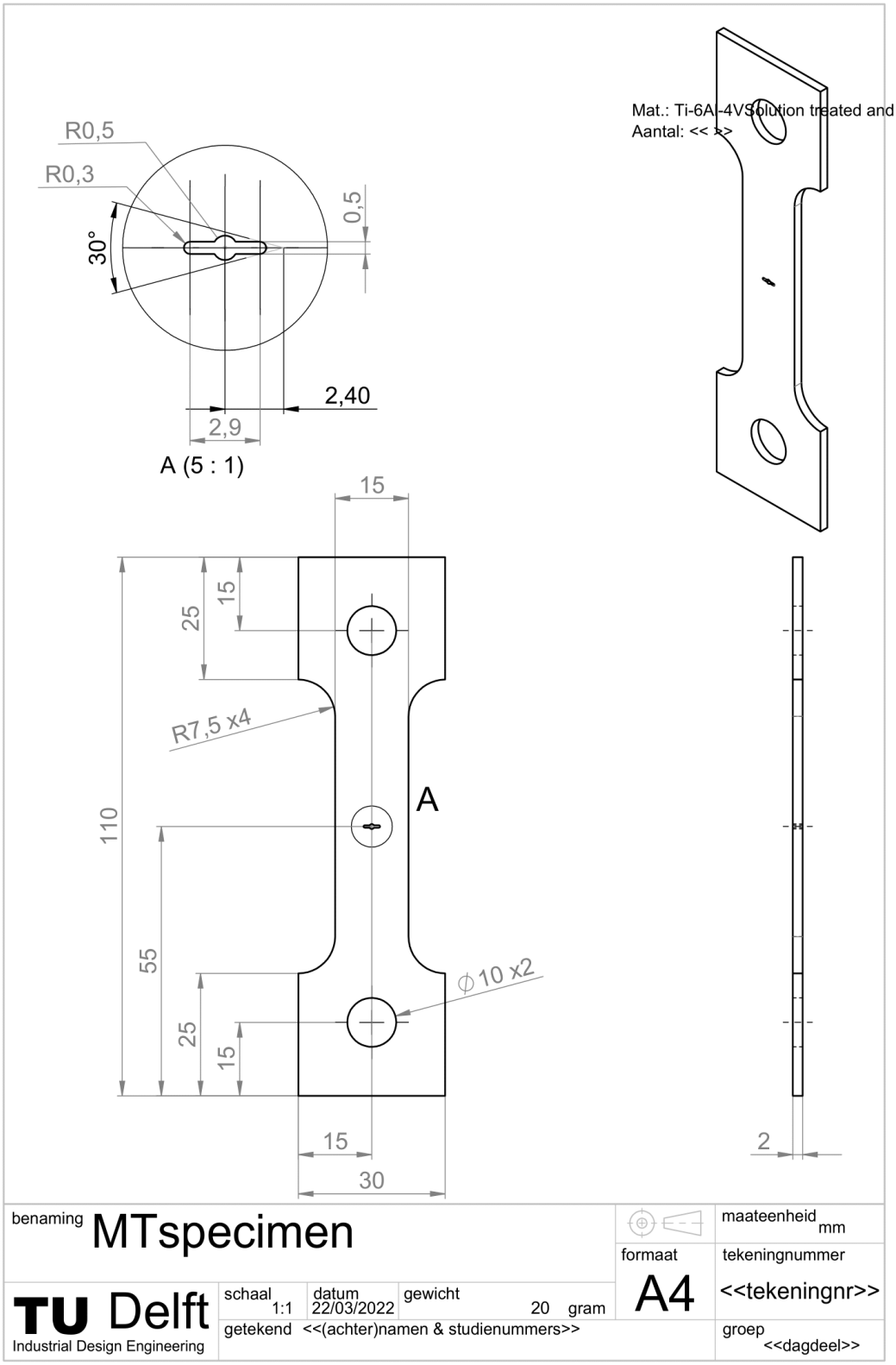

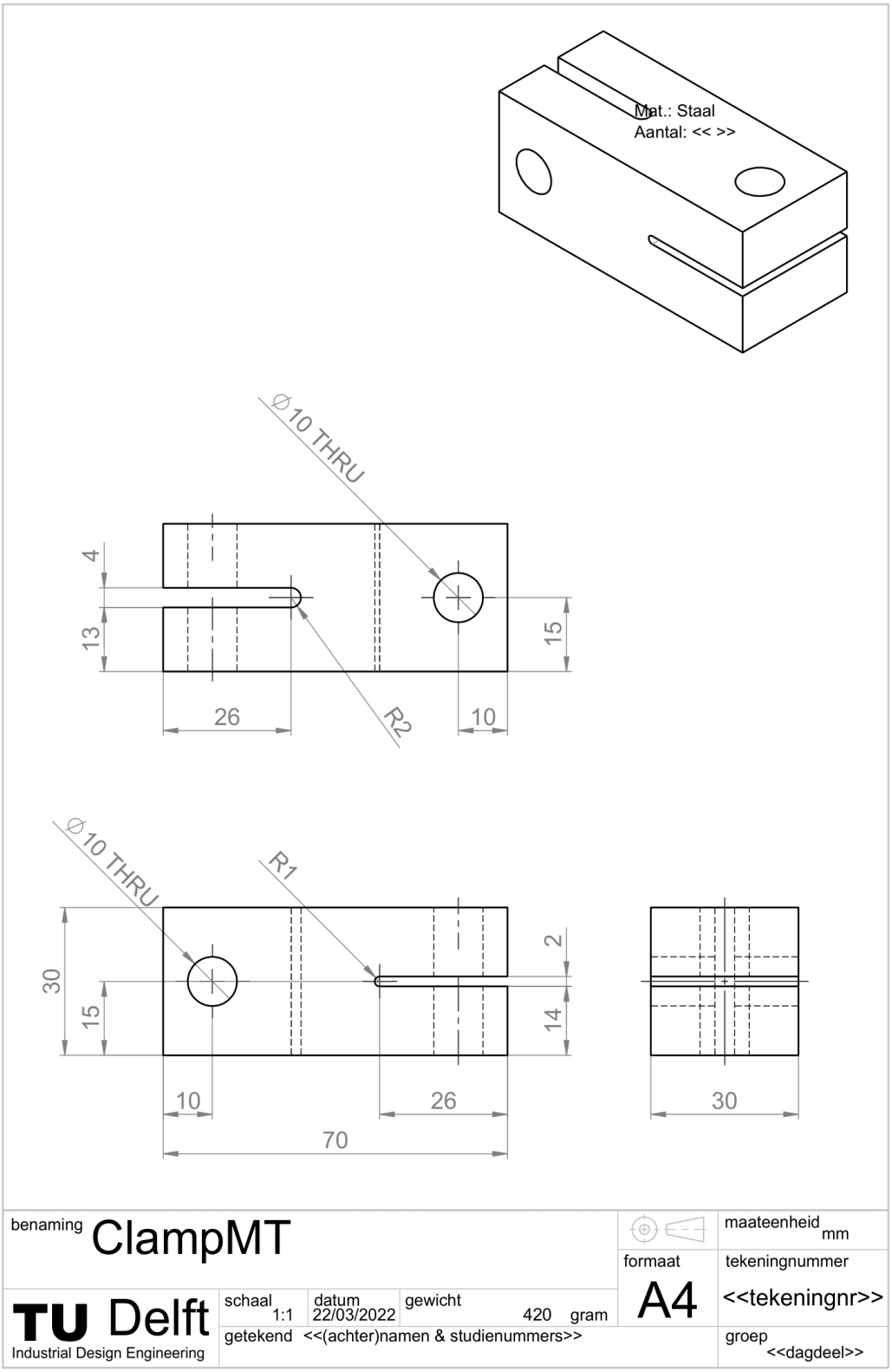

benaming ClampMT				maateenheid mm
TU Delft Industrial Design Engineering	schaal 1:1	datum 22/03/2022	gewicht 420 gram	formaat A4
	getekend <<(achter)namen & studienummers>>			tekeningnummer <<tekeningnr>>
				groep <<dagdeel>>

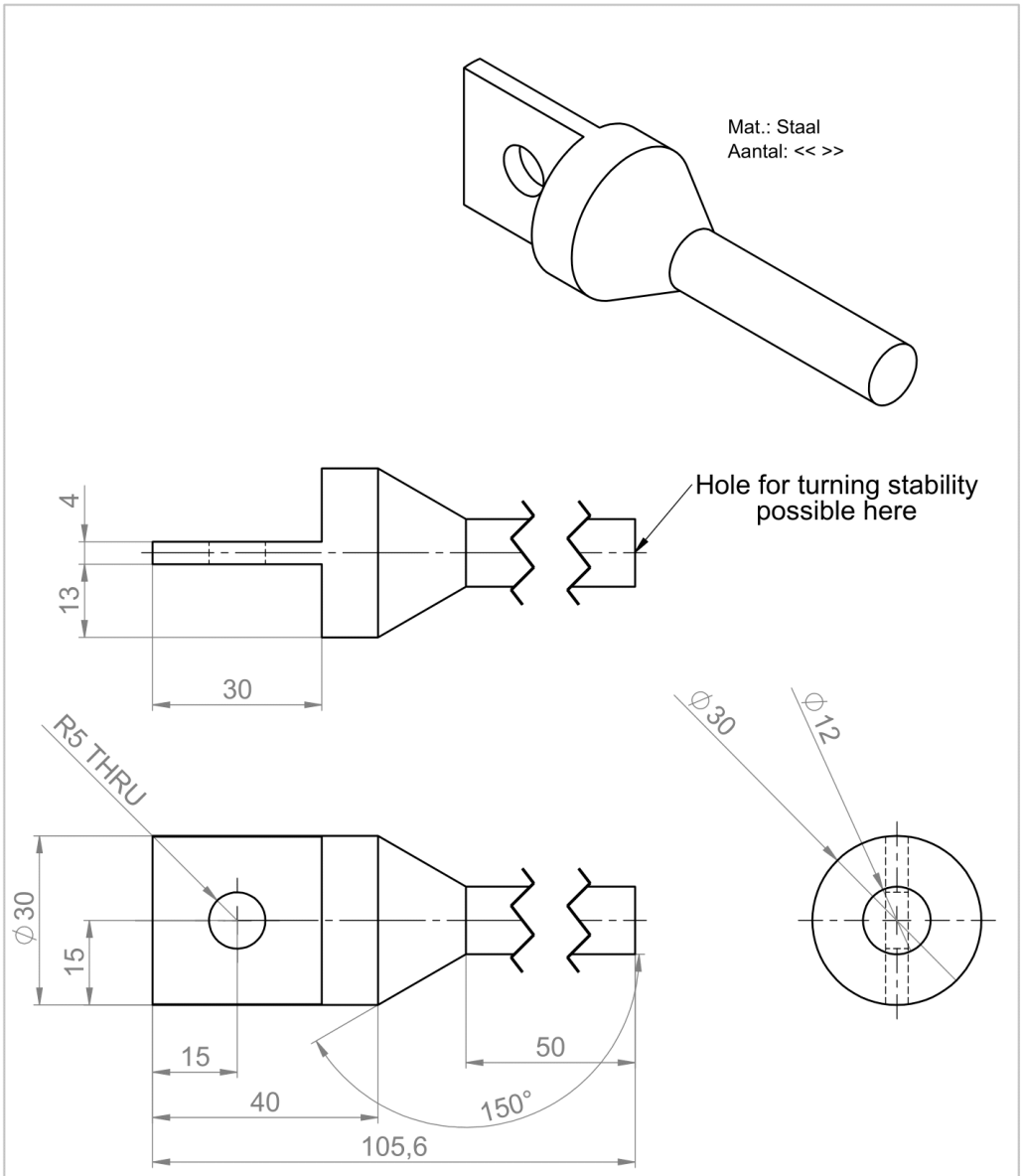

benaming RodMT			maateenheid mm
		formaat A4	tekeningnummer <<tekeningnr>>
TU Delft Industrial Design Engineering	schaal 1:1 / datum 22/03/2022 / gewicht 169 gram		
	getekend <<(achter)namen & studienummers>>		groep <<dagdeel>>

B

Test matrix load-shedding

Table B.1: Expected load shedding method with the calculated cycles per load step for R=0.1 for a crack growth of 200 µm

Stage	ΔK	$F_{amplitude}$ [N]	F_{mean} [N]	No. of Cycles	Expected growth [µm]
Initiation	15	5000	3056	10000	716
Propagation	29	4456	5446	400	200
	26	3793	4635	500	200
	23	3190	3899	800	200
	21	2774	3390	1667	200
	19	2391	2922	4444	200
	17	2040	2493	9524	200
	15	1717	2099	22222	200
	14	1528	1867	28571	200
	12	1248	1525	40000	200
	11	109	1332	66667	200
	10	943	1153	100000	200
	9	807	986	3333333	200

Table B.2: Expected load shedding method with the calculated cycles per load step for R=0.7 for a crack growth of 200 µm

Stage	ΔK	$F_{amplitude}$ [N]	F_{mean} [N]	No. of Cycles	Expected growth [µm]
Initiation	15	5000	3056	10000	716
Propagation	16	2600	14733	167	200
	14	2075	11758	476	200
	13	1850	10483	526	200
	12	1600	9067	690	200
	10	1350	7650	1111	200
	9	1100	6233	2000	200
	8	950	5383	3333	200
	8	850	4817	3846	200
	7	750	4250	5128	200
	6	650	3683	8000	200
	6	575	3258	11111	200
	5	500	2833	36364	200

MTS 500 universal testing machine											
Sample #	**R**	**Thickness**	**W**				Input	Output	Results	***P***	9
2	0,1	0,0019	0,015				Frequency of 10Hz			***I***	3
Ini stage							DeltaK at 10-10m/cycle is DeltaKth			***D***	0
Force [N]					**dK**		**location 1**				
Range	Mean	Amp	Max	Expected cycles	Range		Growth m	Cycles			
5000	3056	2500	5556	10000	16,27		607,55	10000			
Prop stage											
Force [N]					**dK**		**Location 1**				
Range	Mean	Amp	Max	Expected cycles	Range		Cycles	Total crack le	Growth [µm]	Average size [µm]	
8912	5446	4456	9902	400	27,02		400	928,25	320,7	768	
5547	4635	3793	6163	500	17,67		500	1002,22	73,97	965	
3434	3899	3190	3816	800	11,28		800	1194,2	191,98	1098	
3434	3390	2774	3816	1667	9,04		1667	1402,64	208,44	1298	
4782	2922	2391	5313	4444	12,59		4444	2235,64	833	1819	
3055	1867	1528	3394	9524	8,05		10000	2455,64	220	2346	
1886	1153	943	2096	22222	4,97		20000	2502,64	47	2479	

MTS500 universal testing machine											
Sample #	**R**	**Thickness**	**W**				Input	Output	Results	***P***	9
6	0,7	0,0019	0,015				Frequency of 10Hz			***I***	3
Ini stage							DeltaK at 10-10m/cycle is DeltaKth			***D***	0
Force [N]					**dK**		**location 1**				
Range	Mean	Amp	Max	Expected cycles	Range		Growth m	Cycles			
5000	3056	2500	5556	10000	16,27		596	10000			
Prop stage											
Force [N]					**dK**		**Location 1**				
Range	Mean	Amp	Max	Expected cycles	Range		Cycles	Total crack	Growth [µm]	Average size [µm]	
5200	14733	2600	17333	167	16,72		167	747	151	672	
4150	11758	2075	13833	476	13,81		476	857	110	802	
4150	11758	2075	13833	800	12,59		1000	919	62	888	
3700	10483	1850	12333	1667	11,06		1000	977	58	948	
3200	9067	1600	10667	4444	9,51		2000	1073	96	1025	
2700	7650	1350	9000	9524	7,89		5000	1113	40	1093	
2200	6233	1100	7333	22222	6,94		10000	1229	116	1171	

C

All EBSD results

This appendix shows all EBSD results from the cracks sample 4 and sample 8, the order of figures show is from top to bottom: Schmid factor in basal plane, Schmid factor in prismatic plane, Schmid factor in preferred slip plane and HAGB+IPF map.

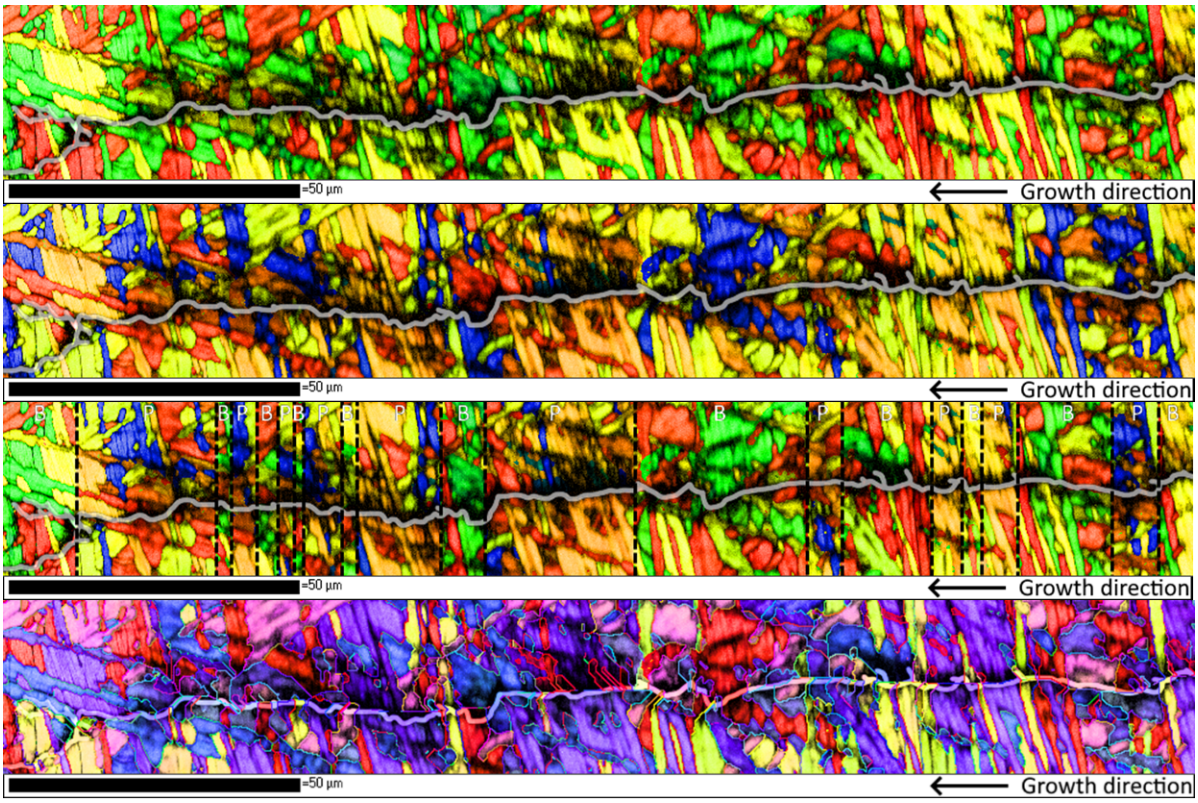

Figure C.1: Crack Sample 4 area 1 tested at R-ratio $= 0.1$ and $\Delta K = 11\,\mathrm{MPa}\sqrt{\mathrm{m}}$

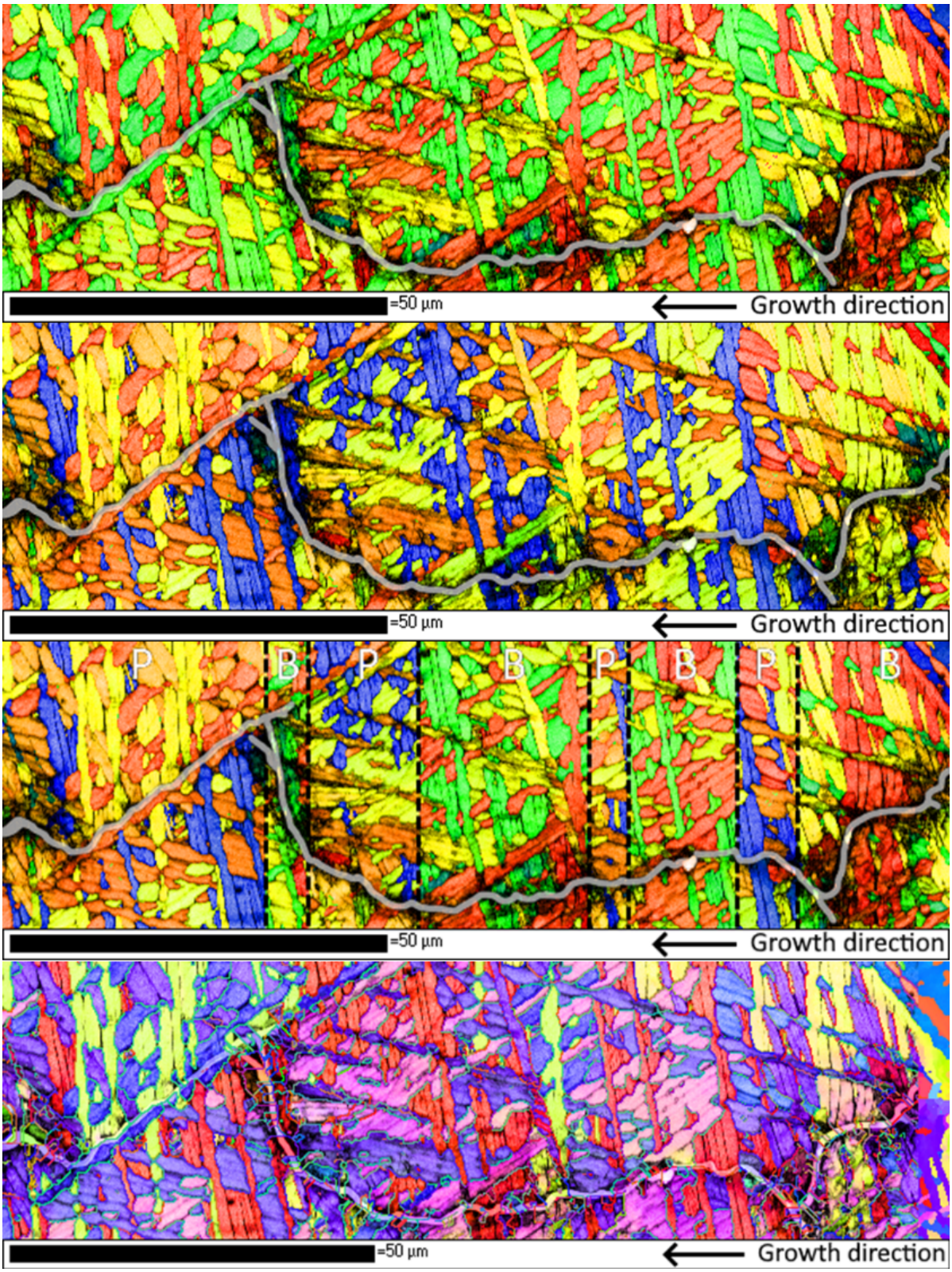

Figure C.2: Crack Sample 4 area 2 tested at R-ratio = 0.1 and $\Delta K = 24\,\mathrm{MPa}\sqrt{\mathrm{m}}$

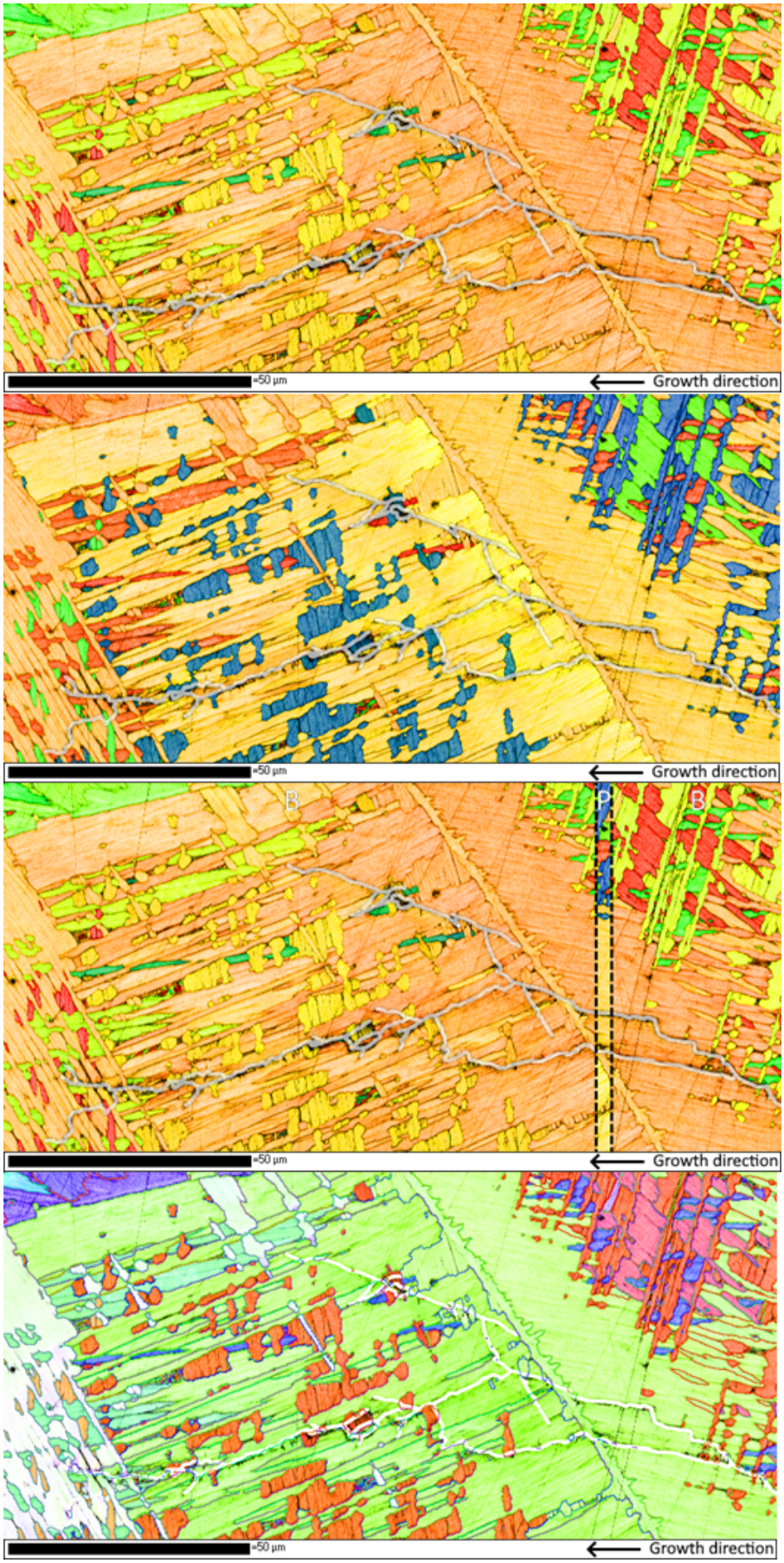

Figure C.3: Crack Sample 4 area 3 tested at R-ratio = 0.1 and $\Delta K = 11\,\mathrm{MPa}\sqrt{\mathrm{m}}$

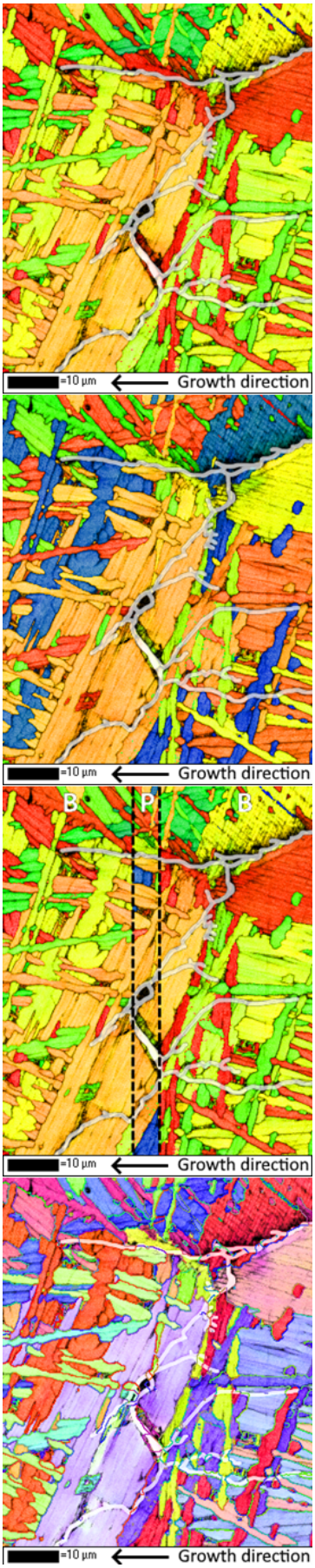

Figure C.4: Crack Sample 4 area 4 tested at R-ratio = 0.1 and $\Delta K = 11\,\mathrm{MPa}\sqrt{\mathrm{m}}$

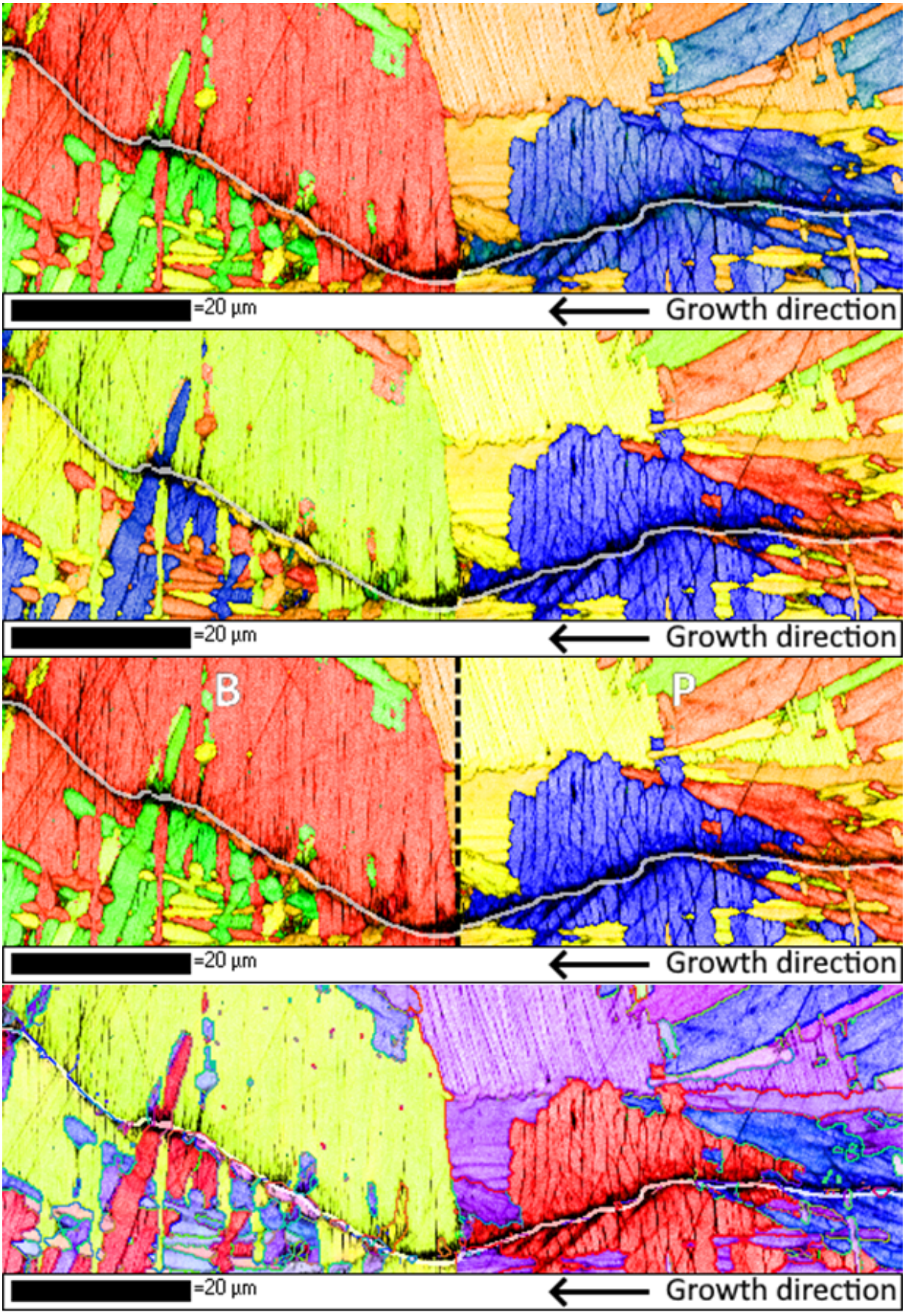

Figure C.5: Crack Sample 4 area 5 tested at R-ratio = 0.1 and $\Delta K = 11\,\mathrm{MPa}\sqrt{\mathrm{m}}$

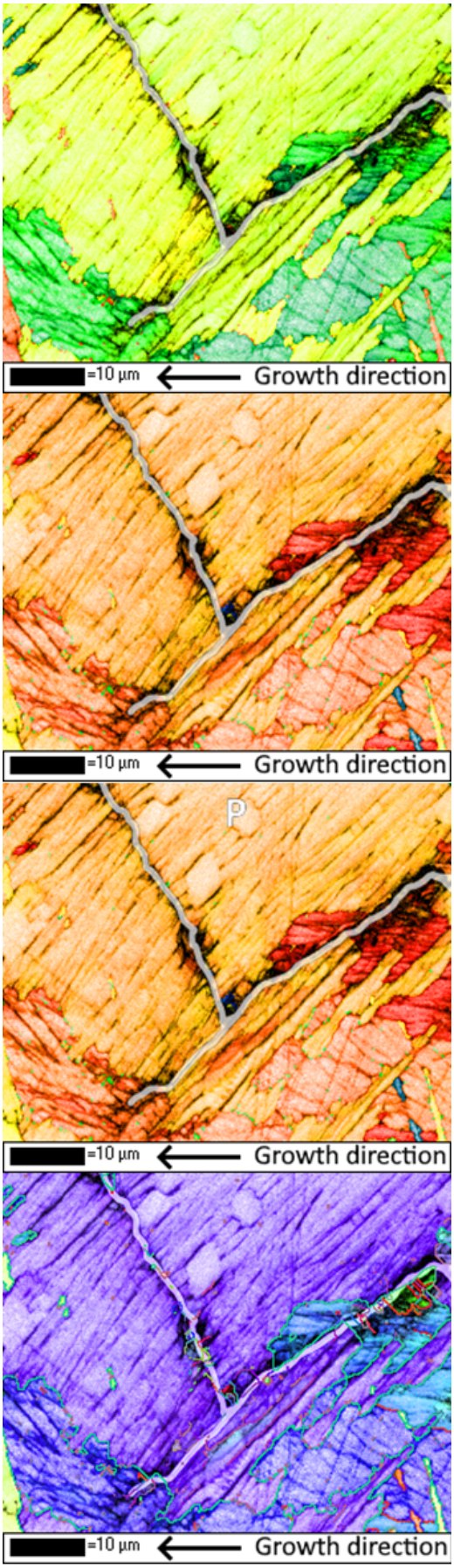

Figure C.6: Crack Sample 8 area 1 tested at R-ratio = 0.7 and $\Delta K = 13\,\mathrm{MPa}\sqrt{\mathrm{m}}$

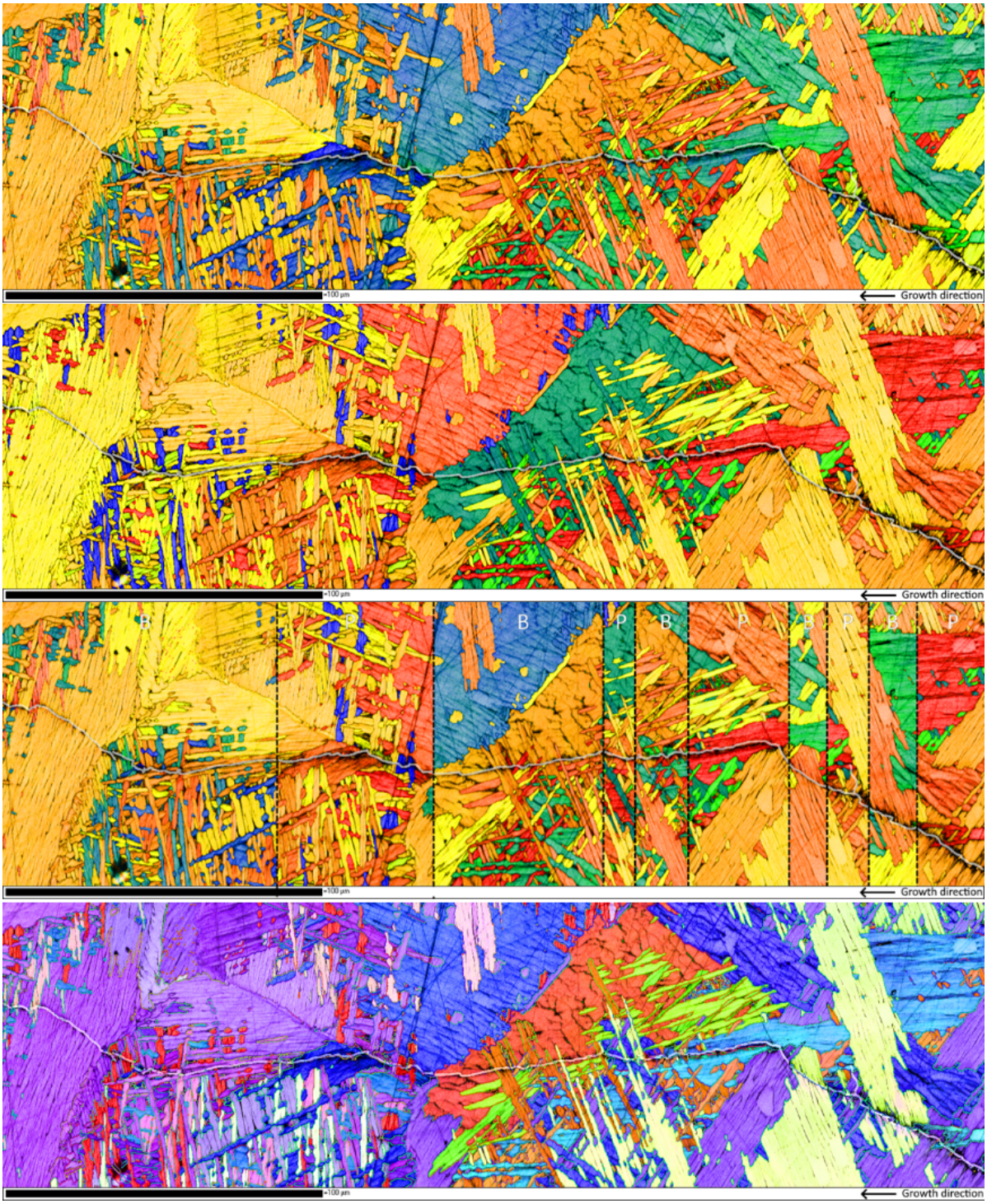

Figure C.7: Crack Sample 8 area 2 tested at R-ratio = 0.7 and $\Delta K = 13\,\mathrm{MPa}\sqrt{\mathrm{m}}$

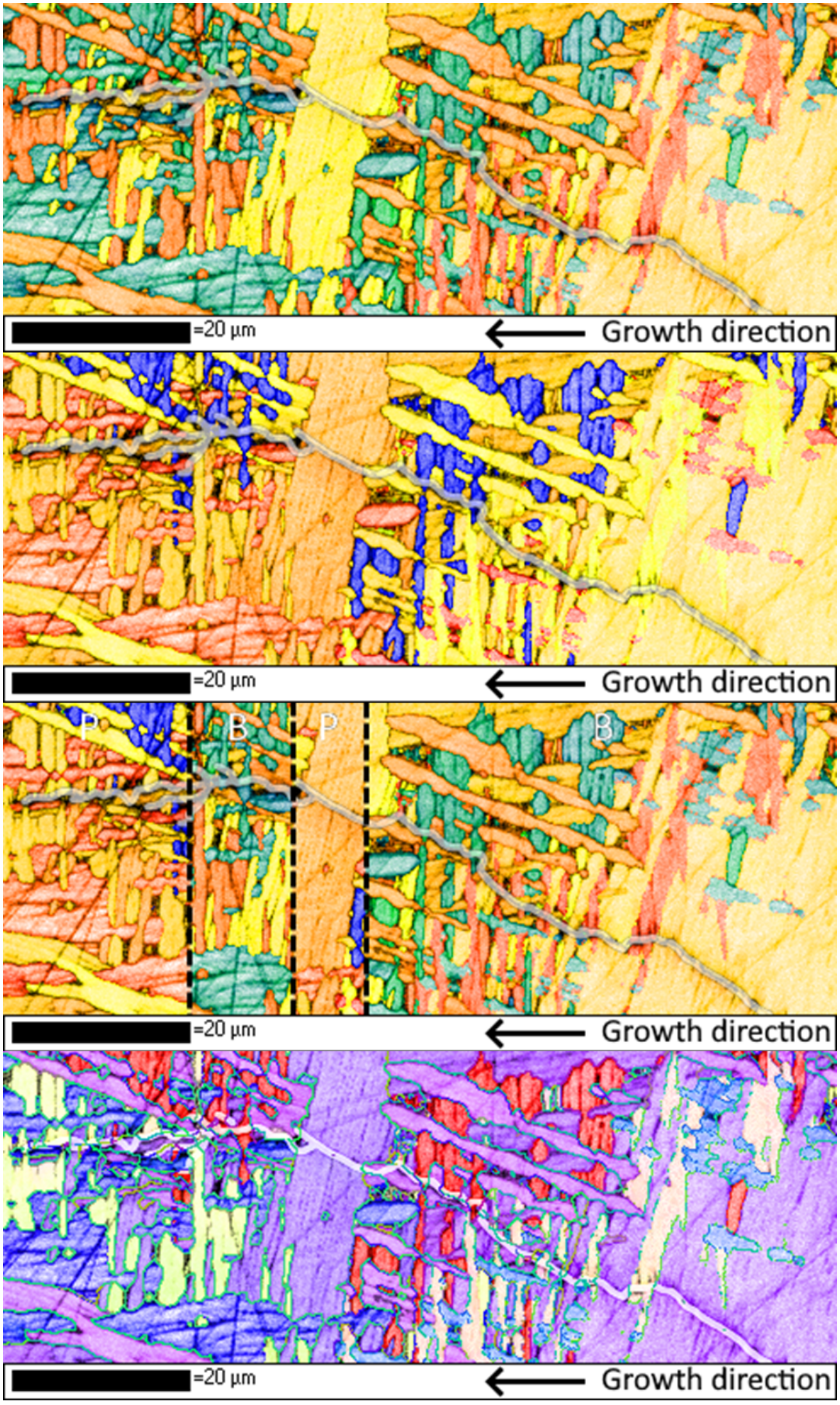

Figure C.8: Crack Sample 8 area 3 tested at R-ratio = 0.7 and $\Delta K = 9\,\mathrm{MPa}\sqrt{\mathrm{m}}$

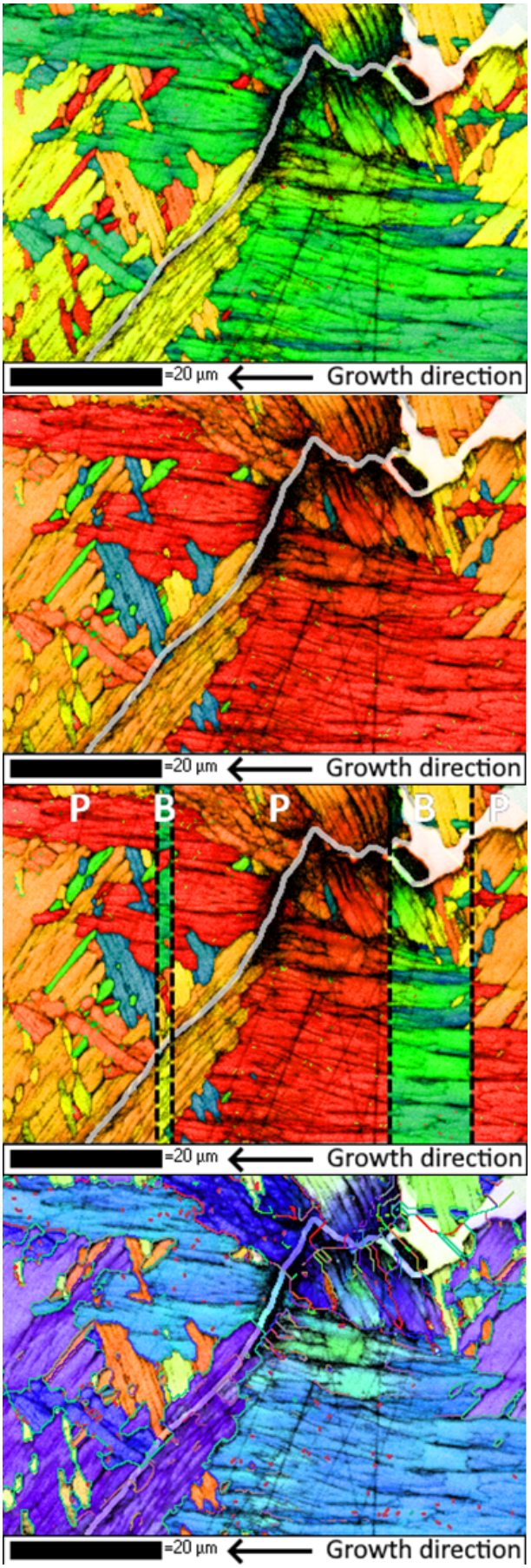

Figure C.9: Crack Sample 8 area 4 tested at R-ratio = 0.7 and $\Delta K = 16\,\mathrm{MPa}\sqrt{\mathrm{m}}$